UNIVERSITE SAAD DAHLAB DE BLIDA 1

Faculté de Technologie

Département de Mécanique

THESE DE DOCTORAT (LMD)

En Génie Mécanique

Spécialité : Construction Mécanique

Vibrational analysis of nanocomposites under hygrothermal effect

Par

MOUAS Zahira

Devant le jury composé de :

TEMMAR Mustapha	Professeur., U. Blida1	Président
AMEUR Mohamed Fayçal	MCA., ENSTA, Alger	Examinateur
BOUKHALKHAL Lamine	Professeur., U. Djelfa	Examinateur
MAGRAOUI Rabah	MCA., U. Blida1	Examinateur
TIBERKAK Rachid	Professeur., U. Blida1	Directeur de Thèse
BACHENE Mourad	Professeur., U. Médéa	Co-directeur de Thèse

Blida, 2025

ملخص

تركز هذه الأطروحة على تحليل الاهتزازات الحرة في الصفائح المركبة ذات مصفوفة بوليميرية مدعّمة بأنابيب الكربون النانوية (CNTs) ، والموزعة إما بشكل منتظم أو بطريقة متدرجة وظيفياً. الهدف الأساسي هو تطوير هياكل مركبة خفيفة الوزن، صلبة، ومتعددة الوظائف، قادرة على العمل بكفاءة في ظروف بيئية رطبة–حرارية (هَيجروحرارية).

تُدمج الأنابيب النانوية الكربونية وفقًا لأنماط توزيع متدرجة وظيفياً مختلفة(UD, FG-X, FG-O, FG-A) مما يسمح بتغيير متحكم فيه في الخصائص الميكانيكية عبر سُمك الصفيحة. يتم تقدير الخواص الفعالة للمواد باستخدام قاعدة الخلط(rule of mixtures) ، مع أخذ التأثيرات الهَيجروحرارية على كل من المصفوفة البوليميرية وعناصر التدعيم بعين الاعتبار. يستند منهج النمذجة إلى نظرية تشوه القص من الدرجة الأولى (FSDT) ، والتي تُعد مناسبة لتحليل الصفائح المركبة. يتم اشتقاق معادلة الحركة باستخدام مبدأ لاغرانج، وتُدرج التأثيرات الهَيجروحرارية من خلال معاملات المرونة الحرارية في نموذج العلاقات .تُستخدم طريقة العناصر المحدودة لنمذجة الاستجابة الاهتزازية للصفيحة تحت ظروف حدية مختلفة. ويتم دراسة تأثير عدة عوامل، بما في ذلك هندسة الصفيحة، ترتيب التكديس، نوع توزيع التدعيم، والظروف الهَيجروحرارية.

يتم التحقق من صحة النتائج العددية من خلال مقارنتها مع الأدبيات المتوفرة، وتُظهر النتائج أن التوزيعات المتدرجة وظيفياً بأنابيب الكربون النانوية تُحسن من الصلابة الفعالة وتُحسن الأداء الاهتزازي للهياكل. على وجه الخصوص، تُظهر بعض التوزيعات غير المنتظمة أداءًا أفضل، حتى تحت التحميل الهَيجروحراري.

توفر هذه الدراسة إرشادات قيمة لتصميم مُحسَّن لهياكل نانوية مركبة مدعّمة بأنابيب الكربون النانوية، مناسبة لتطبيقات عالية الأداء في مجالات مثل الطيران، هندسة السيارات، والهياكل الذكية.

الكلمات المفتاحية: اهتزاز حر؛ بيئة حرارية رطبة؛ نظرية تشوه القص من الدرجة الأولى؛ متدرج وظيفيًا؛ مركب نانوي؛ أنابيب الكربون النانوية.

ABSTRACT

This thesis focuses on the analysis of free vibrations in laminated composite plates with a polymer matrix reinforced by carbon nanotubes (CNTs), distributed either uniformly or in a functionally graded manner. The primary objective is to develop lightweight, stiff, and multifunctional composite structures capable of operating efficiently under hygrothermal environmental conditions.

The CNTs are incorporated according to various functionally graded distribution patterns (UD, FG-X, FG-O, FG-A), enabling controlled variation of mechanical properties through the plate thickness. The effective material properties are estimated using the rule of mixtures, accounting for hygrothermal effects on both the polymer matrix and the reinforcements. The modeling approach is based on the First-Order Shear Deformation Theory (FSDT), which is well-suited for the analysis of laminated plates. The equations of motion are derived using Lagrange's principle, and hygrothermal effects are introduced through thermoelastic coefficients in the constitutive model. The finite element method is employed to model the vibrational response of the plate under various boundary conditions. The influence of several parameters is investigated, including plate geometry, stacking sequence, CNT volume fraction, distribution pattern, and hygrothermal conditions.

The numerical results are validated through comparison with existing literature and demonstrate that functionally graded CNT distributions enhance the effective stiffness and optimize the vibrational performance of the structures. In particular, certain non-uniform distributions achieve a better performance under hygrothermal loading.

This study provides valuable guidelines for the optimized design of CNT-reinforced nanocomposite structures, suitable for high-performance applications in fields such as aerospace, automotive engineering, and smart structures.

Keywords: Free vibration; hygrothermal environment; first-order shear deformation theory; functionally graded; nanocomposite; carbon nanotubes.

RESUME

Cette thèse se concentre sur l'analyse des vibrations libres dans les plaques composites laminées avec une matrice polymère renforcée par des nanotubes de carbone (NTCs), distribués soit uniformément, soit de manière fonctionnellement graduée. L'objectif principal est de développer des structures composites légères, rigides et multifonctionnelles capables de fonctionner efficacement dans des conditions environnementales hygrothermiques. Les NTCs sont incorporés selon différents schémas de distribution fonctionnelle (UD, FG-X, FG-O, FG-A), permettant une variation contrôlée des propriétés mécaniques à travers l'épaisseur de la plaque. Les propriétés effectives des matériaux sont estimées à l'aide de la règle des mélanges, en tenant compte des effets hygrothermiques sur la matrice polymère et les renforts. L'approche de modélisation est basée sur la théorie de la déformation par cisaillement du premier ordre (FSDT), qui est bien adaptée à l'analyse des plaques stratifiées. Les équations du mouvement sont dérivées en utilisant le principe de Lagrange, et les effets hygrothermiques sont introduits par des coefficients thermoélastiques dans le modèle constitutif. La méthode des éléments finis est employée pour modéliser la réponse vibratoire de la plaque dans diverses conditions limites. L'influence de plusieurs paramètres est étudiée, notamment la géométrie de la plaque, la séquence d'empilement, la fraction de volume des NTC, le modèle de distribution et les conditions hygrothermiques.

Les résultats numériques sont validés par comparaison avec la littérature existante et démontrent que les distributions de NTC fonctionnellement graduées améliorent la rigidité effective et optimisent la performance vibratoire des structures. En particulier, certaines distributions non uniformes permettent d'obtenir de meilleures performances sous charge hygrothermique.

Cette étude fournit des indications précieuses pour la conception optimisée de structures nanocomposites renforcées par des NTC, adaptées à des applications de haute performance dans des domaines tels que l'aérospatiale, l'ingénierie automobile et les structures intelligentes.

Mots clés : Vibration libre ; environnement hygrothermique ; théorie de la déformation par cisaillement du premier ordre ; gradient fonctionnel ; nanocomposite ; nanotubes de carbone.

ACKNOWLEDGMENTs

First and foremost, I thank **Allah Almighty** for granting me strength, patience, and guidance throughout this journey.

I would like to express my deepest gratitude to my supervisors, **Prof. Rachid TIBERKAK** and **Prof. Mourad BACHENE**, for their invaluable guidance, continuous support, and insightful advice during the course of this research. Their expertise and encouragement have played a crucial role in shaping both this work and my academic growth.

I would also like to sincerely thank the jury members, **Prof. Mustapha TEMMAR**, **Dr. Mohamed Fayçal AMEUR**, **Prof. Lamine BOUKHALKHAL**, and **Dr. Rabah MAGRAOUI**, for accepting to examine my work and for their valuable time and feedback.

I am also sincerely thankful to **Dr. Yasser CHIKER** for his time, commitment, and support throughout my doctoral studies.

Special thanks go to **Dr. Madjid EZZRAIMI** and **Dr. Taha CHETTIBI** for their thoughtful guidance and for fostering a laboratory environment that inspires dedication and excellence.

My acknowledgments are extended to **Mohamed Essedik LAZAR** and **Samah MAOUDJ**, whose technical assistance, constructive discussions, and moral support were greatly appreciated along the way.

On a personal note, I am deeply grateful to my family for their unconditional love, patience, and support throughout my academic path. Their encouragement has been a source of strength and motivation at every step.

I would like to thank everyone who has helped and supported me, whether directly or indirectly.

Thank you all very much.

CONTENTs

LIST OF FIGURES

LIST OF TABLES

LIST OF SYMBOLS

a : Length of the CNTRC plate (m).

[A] : Matrix of elastic constants due to the membrane effect.

[B] : Matrix of elastic constants due to the bending effect.

b : Width of the CNTRC plate (m).

$[B_i]$: Strain interpolation matrix.

C : Moisture (*wt.*% of H_2O).

[C] : Elasticity matrix.

[D] : Matrix of elastic constants due to the membrane-bending effect.

E_{11}^{CNT} : Longitudinal Young's modulus of carbon nanotube nanofillers (Pa).

E_{22}^{CNT} : Transverse Young's modulus of carbon nanotube nanofillers (Pa).

E^m : Young's modulus of the matrix (Pa).

[F] : Matrix of elastic constants due to the shear effect.

$[J]$: Jacobian matrix.

h : Thickness of the CNTRC plate (m).

[G]: Shape function operating matrix.

G_{12}^{CNT}, G^m: Shear modulus of carbon nanotube and matrix (Pa).

$[K_e]$, $[K]$: Element and global elastic stiffness matrices.

$\left[K_{\sigma_e}\right]$, $[K_\sigma]$: Element and global initial stress stiffness matrices.

L : Total kinetic energy of the plate.

M^H : In-plane hygrothermal moment resultants.

$[\bar{m}]$: Inertia matrix.

$[M_e]$, $[M]$: Element and global mass matrices.

n : Number of plies constituting the plate thickness.

NE : Number of elements.

N_L : Total number of layers.

N_i : Interpolation functions vector.

$[N_i]$: Interpolation matrix.

N^H : In-plane hygrothermal force resultants.

N_N : Number of nodes of the element.

P : Total potential energy of the plate.

P_{in} : Power law index.

$[Q]^k$: The stiffness matrix.

$Q_{ij}^{(k)}$: Elastics constants.

T : Temperature (K).

u , v and w : Displacements components in the directions x, y and z.

u_0 , v_0 and w_0 : Displacements components on the mid-plane of the plate in the directions x, y and z.

$V_m^{(k)}$: Volume fraction of the matrix of the k^{th} layer.

V_{CNT}^* : Volume fraction of the reinforcement of the k^{th} layer.

V_{CNT}^* : CNT volume fraction.

$\{X_e\}$: Element load vector due to external transverse static load.

$\{X_e^H\}$: Element load vector due to hygrothermal forces and moments.

$\alpha_{11}^{(k)}$, $\alpha_{22}^{(k)}$: Thermal expansion coefficients in longitudinal and transverse directions of the k^{th} CNTRC plate layer (K^{-1}).

α_{11}^{CNT} , α_{22}^{CNT} : Thermal expansion coefficients of the CNTs in the longitudinal and transverse directions (K^{-1}).

α^m and β^m : Thermal and moisture expansion coefficients of the matrix.

α_{ij} : Shear correction factors.

$\beta_{11}^{(k)}$, $\beta_{22}^{(k)}$: Moisture expansion coefficients in longitudinal and transverse directions of the k^{th} CNTRC plate layer (%$^{-1}$).

$\{\varepsilon\}^k$: Strain vector.

θ : Angle between the (1, 2) coordinate system (aligned with the material or fiber directions) and the (x, y) coordinate system (Degrees °).

$\theta_x(x, y)$ and $\theta_y(x, y)$: Rotations of the transverse normal about the y and x axes.

η_1, η_2 and η_3 : CNT efficiency parameters.

ρ^{CNT} : CNT density (kg/m^3).

ρ^m : Matrix density (kg/m^3).

$\{\sigma\}^k$: Vector of stress components in the k^{th} ply.

ΔT : Temperature increment from the reference temperature (K).

ΔC : Moisture increment from the reference moisture (*wt.*% of H_2O).

$\{\delta_e\}$: Element displacement.

ν_{12}^{CNT}, ν^m : Poisson's ratio of carbon nanotube and matrix.

w^{CNT} : CNT's weight fraction.

ω : Natural frequency (Hz).

$\bar{\omega}$: Non-dimensional natural frequency.

$\{\Phi\}$: Mode shape.

LIST OF ABREVIATIONS

CNT, CNTs : Carbon Nanotube, Carbon Nanotubes.

CNTRC : Carbon Nanotubes Reinforced Composite Plate.

CPT : Classical Plate Theory.

CCCC : Clamped plate on their four edges.

FGMs : Functionally Graded Materials.

FG : Functionally Graded

FG-X : X functionally graded configuration.

FG-O : O functionally graded configuration.

FG-A : A functionally graded configuration.

FG-V : V functionally graded configuration.

FG-CNTRC : Functionally Graded Carbon Nanotubes Reinforced Composite Plate.

FSDT : First Order Shear Deformation Theory.

FEM : Finite Element Method.

HSDT : Higher Order Shear Deformation Theory.

LC : Laminated Composite.

MWCNTs : Multi-Walled Carbon Nanotubes.

PMMA : Polymethyl Methacrylate Polymer Matrix.

PmPV : Poly(m-phenylenevinylene)-co-[(2,5-dioctoxy-p-phenylene)vinylene] polymer matrix.

SWCNTs : Single-Walled Carbon Nanotubes.

SSSS : Simply supported plate on their four edges.

UD : Uniform Distribution.

GENERAL INTRODUCTION

Composite materials have become indispensable in modern engineering due to their superior mechanical performance, lightweight nature, and outstanding design flexibility. Their ability to achieve tailored properties by combining two or more distinct constituents has enabled their use across a wide range of high-performance applications, including aerospace structures, marine components, automotive systems, and advanced civil engineering designs. As technological demands continue to increase, the need for materials that can maintain mechanical integrity under complex and harsh service environments has grown correspondingly.

Among emerging composite systems, carbon nanotube-reinforced composites (CNTRCs) have attracted significant attention. Carbon nanotubes (CNTs) possess exceptional stiffness, strength, and thermal conductivity, making them ideal nanoscale reinforcements for enhancing the mechanical and functional behavior of polymer matrices. When strategically dispersed or functionally graded through the thickness of a structure, CNTs can deliver substantial improvements in stiffness-to-weight ratio, vibration resistance, and durability. These advantages render CNTRCs promising candidates for next-generation smart and lightweight structural components.

However, many engineering structures operate under hygrothermal environments, where temperature variations and moisture diffusion alter the material properties and induce additional strains. For polymer-based composites, these environmental effects can lead to matrix softening, interfacial degradation, swelling, residual stress development, and ultimately reductions in stiffness and stability. The behavior of CNT-reinforced composites under such coupled temperature–moisture conditions is therefore a critical research area, especially for applications requiring long-term reliability.

Despite increasing interest, the vibrational and mechanical response of functionally graded CNT-reinforced composite (FG-CNTRC) plates under hygrothermal effects remains insufficiently explored. Existing studies often assume constant material properties or neglect the combined influence of thermal and moisture fields on the constitutive behavior. Furthermore, the interaction between CNT distribution patterns, stacking sequences, and

environmental conditions creates complex mechanisms that significantly influence structural performance.

This thesis aims to contribute to this field by developing a comprehensive theoretical and numerical framework to analyze the free vibration behavior of FG-CNTRC plates exposed to hygrothermal environments. The formulation incorporates temperature- and moisture-dependent material properties, hygrothermal strain contributions, and the modification of stiffness matrices to accurately capture environmental effects. The study also investigates the influence of CNT volume fraction, functional grading patterns, geometric parameters, and stacking sequences on the vibrational response of these advanced composite plates.

Through this work, new insights are provided into the design and optimization of environmentally resilient CNT-reinforced composites, offering valuable guidance for their application in demanding engineering environments.

To establish a strong foundation, Chapter One provides a focused literature review on composite and nanocomposite materials, emphasizing the influence of temperature and moisture on their mechanical behavior. It particularly addresses CNT-reinforced composites, outlining how hygrothermal conditions affect stiffness, interfacial bonding, and vibrational performance.

Chapter Two provides a comprehensive review of composite and nanocomposite materials, with a focus on CNT-reinforced systems. It discusses their classifications, mechanical advantages, and the role of FGMs in enhancing structural performance. Special attention is given to the challenges posed by hygrothermal environments, including temperature- and moisture-induced degradation.

The third chapter developed the theoretical model for FG-CNTRC plates using First-Order Shear Deformation Theory (FSDT). Material properties were estimated via the extended rule of mixtures, and the governing equations were derived. The chapter also introduced the Finite Element Method (FEM) as the numerical tool for solving the formulated problem.

Chapter Four detailed the application of the Finite Element Method (FEM) for structural analysis. It covered element discretization, strain-displacement relationships, and the

derivation of equations of motion via Lagrange's principle. The chapter concluded with modal analysis to evaluate the vibrational behavior of the structure.

Chapter Five focused on the free vibration analysis of FG-CNTRC plates under hygrothermal conditions. The study evaluated the impact of CNT distribution patterns, volume fraction, plate geometry, and boundary conditions on the non-dimensional natural frequencies. The developed model was validated against ABAQUS and existing literature, and comprehensive parametric analyses were conducted. The outcomes clearly demonstrate the detrimental effects of temperature and moisture on the structural stiffness, as evidenced by a consistent reduction in natural frequencies. The analysis revealed that optimizing geometric parameters, such as width-to-thickness and aspect ratios, along with tailored CNT volume fractions and distribution profiles, can significantly enhance vibration resistance. In particular, the FG-X distribution pattern proved most effective in improving frequency response under hygrothermal loads.

The thesis further explored laminated CNTRC plates in Chapter Six, a configuration often overlooked in hygrothermal vibration studies. It was shown that angle-ply laminates outperform cross-ply ones, and that boundary conditions and ply stacking sequences have a pronounced impact on vibrational behavior. Notably, this work identified the frequency-symmetry property of angle-ply laminates at room temperature and its disruption at elevated temperatures. Additionally, the role of CNT orientation, the number of plies, and the interaction between power-law index and moisture content was systematically evaluated, offering new design pathways for nanocomposite laminates.

CHAPTER 1: STATE OF THE ART

The advancement of high-performance materials has become a critical objective in modern engineering disciplines, where the demand for lightweight, durable, and efficient materials continues to grow. Among the various material systems developed to meet these requirements, composite materials have emerged as indispensable due to their superior properties. More recently, the integration of nanostructured reinforcements, such as carbon nanotubes (CNTs), into conventional matrix materials has led to the development of nanocomposites. Since their discovery by Iijima [1], CNTs have attracted considerable attention due to their remarkable mechanical, thermal, and electrical properties. Their tensile strength, for example, can reach up to 63 GPa [2], and their Young's modulus can exceed 1 TPa [3]. The integration of CNTs into polymer matrices has been shown to substantially enhance composite properties even at low volume fractions. Jiang et al. [4] observed a remarkable twofold improvement in thermal conductivity with just 1wt% of CNTs, and Zhu et al. [5] demonstrated that incorporating CNTs into a polymer matrix can increase stiffness by up to 20%. Qian et al. [6] conducted one of the early experimental investigations into CNT-reinforced epoxy composites. They reported that the addition of 1 wt% CNTs led to an increase in Young's modulus by up to 36% and tensile strength by 25%, attributed to efficient load transfer between the matrix and CNTs. Thostenson and Chou [7] reviewed CNT dispersion methods and their effects on nanocomposite performance, concluding that uniform dispersion and strong interfacial bonding are critical to achieving property enhancement. To translate these exceptional properties into practical composites, understanding CNT dispersion, alignment, and interfacial bonding is essential, which has motivated the development of various micromechanical models to predict effective composite behavior.

Ajayan et al. [8] investigated the mechanical behavior of polymer composites reinforced with aligned CNTs. Their study demonstrated that the alignment of nanotubes further improves stiffness and strength due to directional reinforcement effects. Similarly, Gojny et al. [9] examined multi-walled CNTs functionalized with carboxyl and amino groups and found that chemical functionalization improved dispersion and interfacial adhesion, resulting in up to a 50% improvement in tensile strength. To predict the effective mechanical properties of CNT-reinforced composites, several micromechanical models have been developed. Shen [10] proposed a modified rule of mixtures incorporating orientation and

efficiency parameters to model the axial and transverse properties of CNT-reinforced beams. He found that the stiffness enhancement was strongly dependent on CNT orientation and dispersion. Rafiee et al. [11] employed the Mori–Tanaka method to model CNT-reinforced nanocomposites and showed that the inclusion of randomly oriented CNTs could increase the effective Young's modulus by up to 80% compared to the pure matrix. Li and Chou [12] developed a multi-scale model combining molecular dynamics simulations and continuum mechanics to evaluate the interfacial effects and CNT waviness on the elastic properties of nanocomposites. Their results indicated that interfacial shear strength and CNT alignment significantly influence overall stiffness. Odegard et al. [13] used a modified Halpin–Tsai approach to capture the scale-dependent reinforcement behavior in CNT-reinforced composites, demonstrating good agreement with molecular modeling results for aligned systems.

Inspired by the remarkable properties of carbon nanotubes (CNTs) and the concept of Functionally Graded Materials (FGMs), Shen [14] introduced the non-uniform distribution of CNTs across the composite structure thickness for the first time when studying the nonlinear bending of FG-CNTRC plates in thermal environments. These composite materials have demonstrated superior performance compared to those with uniform CNT distribution, making them an exciting area of research. This progression toward functionally graded CNT reinforcement motivates further investigations into the response of FG-CNTRCs under complex environmental loading, particularly hygrothermal conditions.

Environmental exposure, particularly elevated temperatures, has been shown to induce significant degradation in the mechanical properties of composite structures. Understanding the thermal behavior of both conventional and CNT-reinforced composites is therefore essential for predicting their performance in real-world applications.

Temperature variations are among the most prevalent environmental factors influencing the long-term behavior of fiber-reinforced composites. Elevated temperatures may lead to matrix softening [15], fiber–matrix interfacial degradation, thermal expansion mismatch [16], and the development of residual stresses [17], all of which can significantly compromise the material's load-bearing capacity. Determining the vibration characteristics of composite plates under such conditions is crucial for their successful utilization in various engineering applications. Extensive research has been conducted to investigate the effects of various parameters and thermal environments on free vibration analysis [18]–[20], static analysis [21], dynamic analysis [22], post buckling analysis [23], [24], buckling analysis

[25], [26], and bending analysis [14], [27]–[29]. These studies have considered a wide range of plate structures, including plates [30], sandwich plates [22, 23], laminated plates [33], [34], spherical and cylindrical shells [35], [36], elliptical and cylindrical shells [37], [38], skew plates [39], plates with various shapes [23], smart piezoelectric sandwich plates [40], and quadrilateral plates [41].

In one of the earliest comprehensive studies, Baker and Dutton [42] demonstrated that glass fiber-reinforced polymer composites exhibited up to a 40% reduction in tensile modulus when exposed to temperatures approaching the glass transition temperature of the matrix. They attributed this behavior primarily to thermal softening and diminished interfacial strength.

Hull and Clyne [43] further highlighted the detrimental effect of thermal cycling, noting the onset of microcracking and interfacial debonding in carbon fiber-reinforced composites. These phenomena, particularly under repeated temperature fluctuations, result in cumulative damage that reduces fatigue life and overall durability. Their work emphasized the necessity of considering thermal fatigue when designing composite structures for high-temperature applications.

As research advanced toward nano-enhanced systems, the behavior of CNT-reinforced nanocomposites under thermal conditions attracted increasing attention. Thostenson et al. [44] reported that CNTs can improve thermal stability by impeding polymer chain mobility and enhancing thermal conductivity, which delays the onset of thermal degradation. They observed improved modulus retention at elevated temperatures in CNT-filled epoxy systems compared to neat polymers.

Nevertheless, the mismatch in thermal expansion coefficients between CNTs and polymer matrices can give rise to interfacial stresses, especially under non-uniform temperature distributions. Al-Saleh and Sundararaj [45] found that while CNTs enhanced the thermal conductivity of composites, exposure to high temperatures beyond critical thresholds weakened interfacial bonding, reducing effective load transfer and resulting in deteriorated mechanical performance. Uymaz et al. [46] conducted a three-dimensional thermal vibration analysis of FG-CNT reinforced plates under uniform, linear, and sinusoidal temperature distributions. Their findings demonstrated that both the amount and distribution type of temperature significantly influence the frequencies.

Qian et al. [47] developed a thermo-mechanical micromechanical model to quantify the effect of thermal loading on CNTRCs, incorporating CNT orientation and interfacial properties. Their simulations showed that aligned CNTs significantly mitigated thermal softening effects, leading to more stable stiffness values over a wide temperature range. Shen and Li [48] investigated thermally induced bending of functionally graded CNTRC plates using nonlinear finite element models. Their results indicated that graded CNT distributions helped redistribute thermal stresses more effectively than uniformly reinforced configurations, reducing stress concentrations and enhancing thermal resistance.

Despite the promising findings, the thermomechanical response of CNTRCs remains highly dependent on factors such as CNT volume fraction, dispersion quality, interfacial bonding, and the thermal properties of the matrix. Continued research is therefore necessary to establish predictive models and robust material systems for thermally demanding environments.

Although significant progress has been made in understanding the influence of temperature alone, real-world applications often expose composite materials to coupled environmental conditions, where moisture presence can alter thermal responses.

Moisture, along with temperature, is a critical environmental factor that significantly influences the strength and behavior of polymeric composite structures. The hygrothermal effect on composite materials must be carefully considered in various engineering applications, particularly when designing structures for use in environments with fluctuating moisture and temperature. When exposed to humid environments or direct water contact, composite materials tend to absorb moisture over time through diffusion, capillary action, or microcrack pathways. This absorbed moisture can lead to several deleterious effects such as plasticization of the matrix, swelling-induced stresses, hydrolysis, and fiber–matrix interfacial debonding [49].

In their seminal study, George and Springer [50] investigated the effects of moisture absorption on glass fiber-reinforced polyester composites, revealing critical insights into environmental degradation. They found that prolonged water immersion at 60°C caused a significant 25°C reduction in the glass transition temperature (Tg), from 112°C to 87°C, accompanied by a 35% decrease in flexural modulus and a 40% loss in interlaminar shear strength. Shen and Springer [51] provided one of the first analytical models for moisture diffusion in composites, highlighting the significance of boundary conditions and laminate thickness on absorption behavior. Banea and Silva [52] observed similar degradation in

structural adhesives used in composite joints, emphasizing the universality of moisture-related deterioration across various composite systems.

With the evolution of nanocomposites, researchers began investigating whether the inclusion of CNTs could mitigate moisture effects. Xu et al. [53] demonstrated that CNTs could reduce the overall moisture uptake in polymer matrices by acting as barriers to diffusion pathways. Their study on CNT-reinforced epoxy showed a 15% lower equilibrium moisture content compared to unreinforced epoxy. Studies have demonstrated that the elastic moduli and strength of composites are reduced at high temperature and moisture levels [54]–[56]. These environmental conditions can also influence the vibrational behaviors and natural frequencies of composite structures. Inala [57] investigated the vibration characteristics and parametric instability of FGM plates subjected to cyclic loading in a hygrothermal environment. Their study demonstrated that elevated temperature and moisture reduce the frequency parameters of FGM plates, indicating a softening effect. Additionally, the critical buckling load of the FGM plate decreases with increasing moisture concentration, implying a reduction in structural stability. Zaitoun et al. [58] examined the thermal buckling response of a sandwich FG ceramic-metal plate resting on a viscoelastic foundation under hygrothermal conditions. Their findings revealed a linear relationship between the thermal buckling load of the FG sandwich plate and increasing foundation parameters. The effect of the damping coefficient was found to be dependent on the FG sandwich plate configuration. Subsequently, Zaitoun et al. [59] developed a high-order shear deformation theory to determine the free vibration response of FG sandwich plates subjected to hygrothermal loads and resting on viscoelastic foundations. Arshid et al. [60] explored the vibrational behavior of sandwich structures incorporating FG microplates embedded with polymeric nanocomposite patches under hygrothermal conditions. Employing an innovative plate theory, they observed a reduction in stability and stiffness of these structures due to the presence of hygrothermal environments. This degradation in mechanical properties is

attributed to the softening effect of temperature and moisture on the composite materials. Furthermore, their study revealed a step-by-step decrease in natural frequency, stability, and stiffness with increasing external electrical voltage, suggesting an additional destabilizing factor.

V. Kallannavar et al. [61] examined the effect of temperature and moisture on the free vibration characteristics of skew-laminated composite sandwich panels. They found that the natural frequencies of the flat sandwich plate are more sensitive to thermal and moisture environments, while the spherical sandwich shell shows greater resilience to changing environmental conditions. Zhang et al. [62] investigated the vibration analysis of cylindrical sandwich shells with FG porous core in hygrothermal environments. As discussed in reference [62], an increase in the length of graphene nanoplatelets (GNPs) and a decrease in the porosity coefficient, humidity, and temperature differences can increase the natural frequency. Moreover, Yüksel and Akbaş [33] studied the stress analysis of simply supported FG composite laminated plates with porosity subjected to hygrothermal conditions. Yüksel and Akbaş revealed that the hygrothermal stress behavior of porous laminated plates is significantly influenced by both the porosity coefficient and different porosity distribution models. Bisheh et al. [63] conducted the first free vibration analysis of piezoelectric coupled CNT-reinforced composite shells, considering different boundary conditions and hygrothermal environments. They found that the hygrothermal environment significantly influences the vibration characteristics of these shells. The piezoelectric coupling, which allows for the conversion between mechanical and electrical energy, introduces additional factors to the vibration response. Al-Furjan et al. [64] investigated the nonlinear forced vibrations of CNT-reinforced viscoelastic thick annular plates under hygrothermal environments. Their findings showed that CNT reinforcement enhanced structural stiffness and vibration resistance, particularly when functionally graded. However, increasing

temperature and moisture levels reduced stiffness, leading to lower natural frequencies and higher vibration amplitudes. The study also emphasized the role of viscoelastic foundations in damping vibrations and noted that nonlinear effects became more significant under higher excitation levels and severe environmental conditions. Investigating the nonlinear free vibration and nonlinear dynamic hygrothermal buckling behaviour of imperfect functionally graded carbon nanotube reinforced composite (FG-CNTRC) cylindrical panels subjected to hygrothermal environments, Foroutan et al. [65] observed that CNTRC with an FG-Λ distribution pattern exhibits the most favourable nonlinear free vibration response and nonlinear dynamic hygrothermal buckling response compared to other distribution patterns. Additionally, Penna et al. [66] studied the dynamic response of multilayered functionally graded CNT-reinforced polymer nano-beams under hygrothermal environments. They found that increased temperature and moisture content reduced flexural frequencies due to the degradation of material properties. However, a higher CNT volume fraction improved stiffness and mitigated these adverse effects. The functionally graded "X" distribution of CNTs provided the best vibrational performance. Additionally, the use of local/nonlocal stress gradient theory revealed that nonlocal parameters influenced the stiffening or softening behavior of the structure, highlighting the importance of size-dependent effects in nanoscale applications. Furthermore, using the proposed C-0 finite element-based higher-order zigzag theory, Chalak et al. [67] conducted a study on the free vibration and modal stress analysis of functionally graded carbon nanotube-reinforced composite (FG-CNTRC) beams under hygrothermal conditions. The research revealed that increasing temperature and moisture levels led to reductions in natural frequencies and alterations in stress distributions, with higher vibration modes being more sensitive to these environmental factors. Among various CNT distribution patterns, the FG-O configuration exhibited the least sensitivity to thermal effects, while the FG-X pattern was the most affected. These

findings underscore the importance of considering both environmental conditions and CNT distribution in the design of FG-CNTRC structures. Patnaik and Roy [68] explored the vibration and damping response of functionally graded carbon nanotube-reinforced hybrid composite skewed shell structures under hygrothermal loading. The study employed finite element analysis and Rayleigh damping assumptions to assess the influence of CNT gradation, fibre orientation, and moisture/temperature variations. The results demonstrated that increasing CNT content and employing optimal gradation significantly improved natural frequencies and damping ratios, helping to offset the degradative effects of hygrothermal exposure.

Recently, Alsubaie et al. [69] investigated the vibration response of porous functionally graded CNTRC beams under hygrothermal environments. Applying a simplified higher-order shear deformation theory, they analyzed the effects of various porosity profiles and moisture-temperature levels on natural frequencies. The study found that moisture and porosity jointly reduce stiffness and frequency, while strategic CNT distribution across the beam thickness helps to mitigate these losses and enhances vibrational resilience. Zhai et al. [70] studied the thermomechanical buckling and vibration of composite sandwich doubly curved shells with carbon nanotube-reinforced face layers. Employing first-order shear theory and Hamilton's principle, they derived vibration and stability equations under thermomechanical loads. The study found that temperature variations notably affect the buckling load and vibration frequencies, highlighting the importance of thermal considerations in the design of such composite structures. Patnaik [71] explored the vibrational parameters of viscoelastic CNT–carbon fiber reinforced polymer (CFRP) hybrid spherical shell structures under hygrothermal conditions. Through finite element modelling, the study assessed how temperature and moisture variations affect frequency responses and transient behaviors. The findings indicated that hygrothermal environments significantly

influence the dynamic performance of these hybrid structures, emphasizing the need for careful consideration in design applications.

Building upon the insights gained from functionally graded CNTRCs, it is equally important to examine the hygrothermal behavior of laminated CNT-reinforced composites, where the multilayered configuration introduces additional complexity in moisture and thermal diffusion mechanisms, interfacial stresses, and overall structural response. The effect of hygrothermal conditions on the free vibration of laminated plates has been considered earlier by Whitney and Ashton [19]. Utilizing Classical Laminate Plate Theory (CLPT), they incorporated hygrothermal strains into the constitutive relations to account for the effects of thermal expansion and moisture-induced swelling. Their analysis revealed that environmental factors could significantly alter the stiffness and stress distribution within composite laminates, leading to notable changes in their elastic behavior. Patel et al. [72] examined the static and dynamic behavior of thick laminated composite plates under hygrothermal conditions using a higher-order shear deformation theory (HSDT). The formulation accounted for nonlinear variations of in-plane and transverse displacements through the thickness and incorporated abrupt discontinuities in the slope of in-plane displacements at layer interfaces. Utilizing an eight-nodded isoparametric quadrilateral finite element model, the analysis revealed that increases in temperature and moisture concentration significantly reduce the stiffness of composite laminates, leading to increased deflections and decreased natural frequencies. Rath and Sahu Sahu [73] conducted both experimental and numerical investigations to examine the free vibration behavior of woven fiber laminated composite plates under varying temperature and moisture conditions. Utilizing a finite element model developed in MATLAB, they analyzed the dynamic response of glass/epoxy laminates subjected to hygrothermal loading. The study revealed that increases in temperature and moisture concentration lead to a significant reduction in

natural frequencies, attributed to the degradation of material stiffness. Additionally, the research demonstrated that anti-symmetric laminates exhibit higher vibration frequencies compared to symmetric laminates, and an increase in the number of layers further enhances these frequencies.

Recently, Bouazza and Zenkour [74] investigated the free vibration behavior of multilayered composite plates subjected to hygrothermal conditions using a refined hyperbolic shear deformation theory. This theory accounts for the realistic distribution of transverse shear strains through the plate's thickness without requiring shear correction factors. The study considered temperature and moisture-dependent material properties to simulate hygrothermal effects accurately. Their findings revealed that increases in temperature and moisture concentration lead to a significant reduction in natural frequencies, indicating a decrease in structural stiffness. Abdelmalek et al. [75] explored the free vibration behavior of composite plates under hygrothermal environments using a refined nth-order shear deformation theory. This advanced theory captures the parabolic distribution of transverse shear strains through the plate's thickness, eliminating the need for shear correction factors. The study incorporated temperature and moisture-dependent material properties, evaluated through a micromechanical approach. The results demonstrated that hygrothermal effects, such as increased temperature and moisture content, significantly reduce the natural frequencies of composite plates, indicating a degradation in stiffness. Bisheh and Civalek [76] investigated the vibration characteristics of smart laminated CNTRC cylindrical panels resting on elastic foundations, considering hygrothermal environmental effects. Their study demonstrated that factors such as increasing the number of end supports, employing elastic foundations, and increasing the nanotube volume fraction positively influenced the vibrational frequencies. Conversely, increasing panel length,

decreasing panel thickness, integrating piezoelectric materials, and elevating temperature and moisture levels were observed to decrease the frequencies.

In summary, while substantial progress has been made in understanding the mechanical performance of carbon nanotube-reinforced composites under individual hygrothermal effects, the complex interaction of temperature and moisture (especially in laminated and functionally graded configurations) remains insufficiently explored. Most existing studies focus either on idealized configurations or exclude the combined environmental impact. This research aims to bridge this gap by investigating the vibrational behavior of CNT-reinforced composite plates, including laminated and FG-CNTRC configurations, subjected to hygrothermal environments. The insights derived from this study are expected to enhance the predictive capability of structural models and support the development of more resilient nanocomposite systems for advanced engineering applications.

CHAPTER 2: COMPOSITE AND NANOCOMPOSITE MATERIALS – FUNDAMENTALS AND HYGROTHERMAL CONSIDERATIONS

2.1 Introduction

Composite materials are widely used in engineering applications due to their high strength-to-weight ratio, durability, and design flexibility. The incorporation of carbon nanotubes (CNTs) as reinforcements further enhances their mechanical, thermal, and electrical properties. However, despite their promising characteristics, the long-term durability of CNT-reinforced composites under environmental conditions remains a critical concern. These materials are often exposed to hygrothermal environments, where fluctuations in temperature and humidity can lead to mechanical degradation, moisture absorption, and thermal expansion mismatches. Such conditions are particularly severe in aerospace and marine applications, where materials experience continuous cycles of high humidity, elevated temperatures, and mechanical stress.

This chapter provides an overview of composite materials, their classification, constituents, and applications. It also examines the challenges associated with CNT dispersion, interfacial bonding, and processing techniques, which directly impact their structural integrity. Finally, the chapter discusses the effects of hygrothermal aging on CNT-reinforced composites.

2.2 Composite materials

Composite materials are engineered materials that consist of two or more distinct constituents (each possessing different physical or chemical properties) that, when combined, produce a material with enhanced characteristics. Typically, a composite is made up of a reinforcement phase (such as fibers, particles, or whiskers) embedded within a continuous matrix (usually a polymer, metal, or ceramic) [77]. The reinforcement phase provides superior strength, stiffness, and sometimes other properties like high-temperature resistance, while the matrix binds the reinforcements together, distributes loads, and protects them from environmental and mechanical damage.

The primary motivation for developing and utilizing composite materials is to achieve an optimal combination of mechanical strength, stiffness, and lightweight characteristics. This makes them highly suitable for applications in aerospace, automotive, marine, civil infrastructure, and biomedical engineering.

To illustrate the practical advantages of composite materials over traditional materials, Figure 2.1 compares key properties of steel, aluminum (Al), and composite materials in terms of weight, thermal expansion, stiffness, strength, and fatigue resistance. Composites are the lightest, strongest, and most fatigue-resistant among the materials compared. They exhibit the lowest thermal expansion, ensuring dimensional stability, and can achieve high stiffness depending on their reinforcement. With their superior strength-to-weight ratio and durability, composites are ideal for high-performance applications.

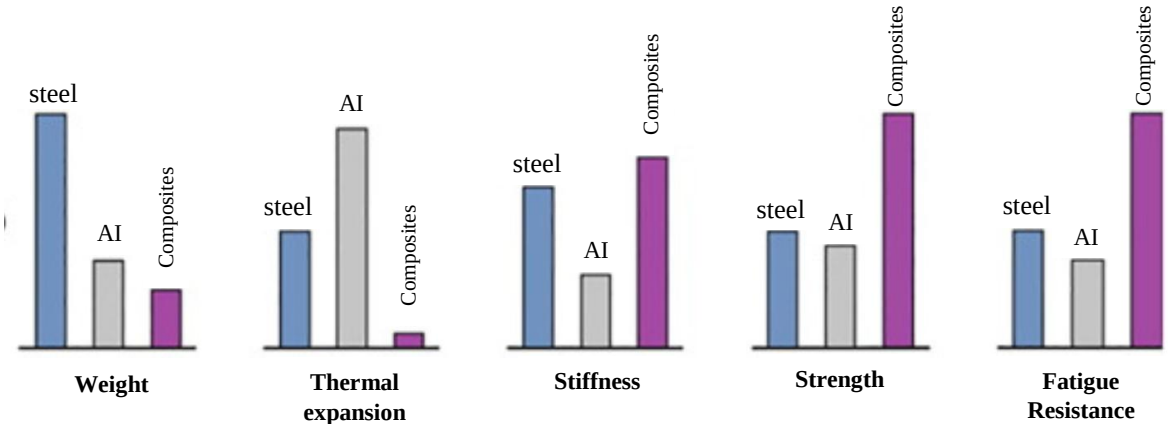

Figure 2.1 : Comparison between pure metals and composite materials [78]

2.1.1 Classification of composite materials

Composite materials can be systematically categorized based on their matrix phase, the type of reinforcement utilized, and the scale at which the reinforcement is incorporated. Figure 2.2 provides a schematic representation of this classification, offering a clear visualization of the hierarchical structure within composite systems. Additionally, Table 2.1 enumerates specific examples of various composite types, detailing their constituent materials and common areas of application. Together, these visual aids facilitate a comprehensive understanding of the diverse material configurations and their functional roles in different engineering domains.

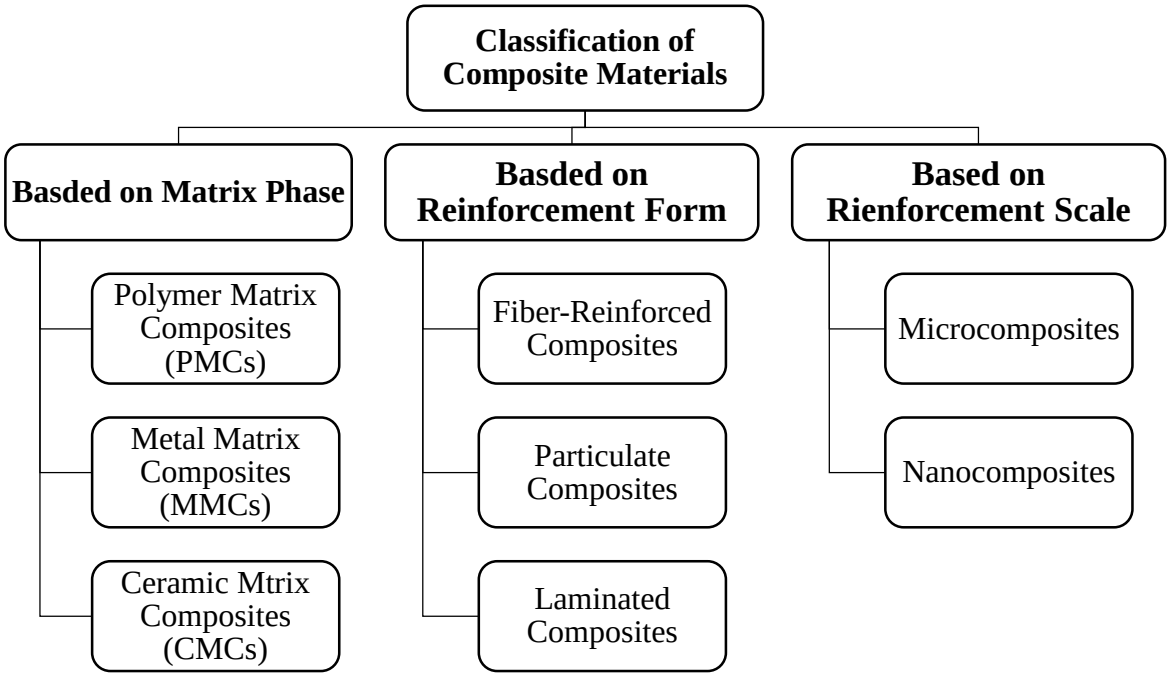

Figure 2.2 : Hierarchical classification of composite materials

Table 2.1 Examples of composite material types with their constituents and typical applications

Composite Type	Constituents	Application Areas
1. Organic matrix composites		
Paper, cardboard	Resins, fillers, cellulose fibers	Packaging, printing, etc.
Particle boards	Resin, wood chips	Woodworking, furniture
Fiberboards	Resin, wood fibers	Construction industry
Coated fabricses	Flexible resins, textiles	Sports equipment, waterproof coverings
Sealing materials	Elastomers, bitumen, textiles	Roofing, waterproofing
Tires	Rubber, fabric, steel	Automotive
Laminates	Resins, glass fibers, carbon fibers	Transport, construction
Reinforced plastics	Resins, microspheres	Multidomain applications
2. Mineral Matrix Composites		
Concrete	Cement, sand, aggregates	Civil engineering
Carbon-carbon composites	Carbon matrix, carbon fibers	Aerospace, biomedical, high-temperature systems

Ceramic composites	Ceramic matrix, ceramic fibers	Thermomechanical components
3. Metallic Matrix Composites		
Aluminum-based systems	Aluminum matrix with boron or carbon fibers	Aerospace structures
4. Sandwich Composites		
Faces	Metals, laminates	Multiple domains
Cores	Foams, honeycomb structures, balsa wood, reinforced polymers	Lightweight panels for aerospace, marine, etc.

2.3 Nanocomposite materials

While traditional composite materials have significantly advanced engineering performance in various fields, they often face limitations in achieving multi-functionality and optimal performance at small scales. To overcome these limitations, a new class of materials known as nanocomposites has emerged. These materials incorporate nanoscale reinforcements (such as carbon nanotubes, graphene, or nanosilica) into conventional matrices, enabling unprecedented improvements in mechanical, thermal, and electrical properties.

2.3.1 Definition of nanocomposite materials

Nanocomposites are characterized by the incorporation of nanoscale reinforcements into a conventional matrix. These reinforcements typically have at least one dimension in the nanometer range (1–100 nm) and include nanoparticles, nanofibers, nanotubes, or nanosheets [79]. Due to their extremely high surface area-to-volume ratio and unique quantum-level interactions, nanocomposites exhibit enhanced mechanical, thermal, electrical, and barrier properties compared to their micro- or macro-reinforced counterparts.

The nanoscale dispersion of fillers enables superior stress transfer, interfacial bonding, and multi-functionality, even at low reinforcement concentrations. This makes nanocomposites highly attractive for applications requiring lightweight materials with customized and enhanced performance metrics.

2.3.2 Classification of nanocomposite materials

Nanocomposite materials can be classified using multiple criteria depending on the focus of the application or the design strategy. Figure 2.3 illustrates two widely adopted classification schemes: (1) the type of matrix material and (2) the morphology of the nanofillers incorporated into the matrix. These classifications provide complementary perspectives, reflecting both the macroscopic functional domain of the composite and the nanoscale architecture of the reinforcing phase.

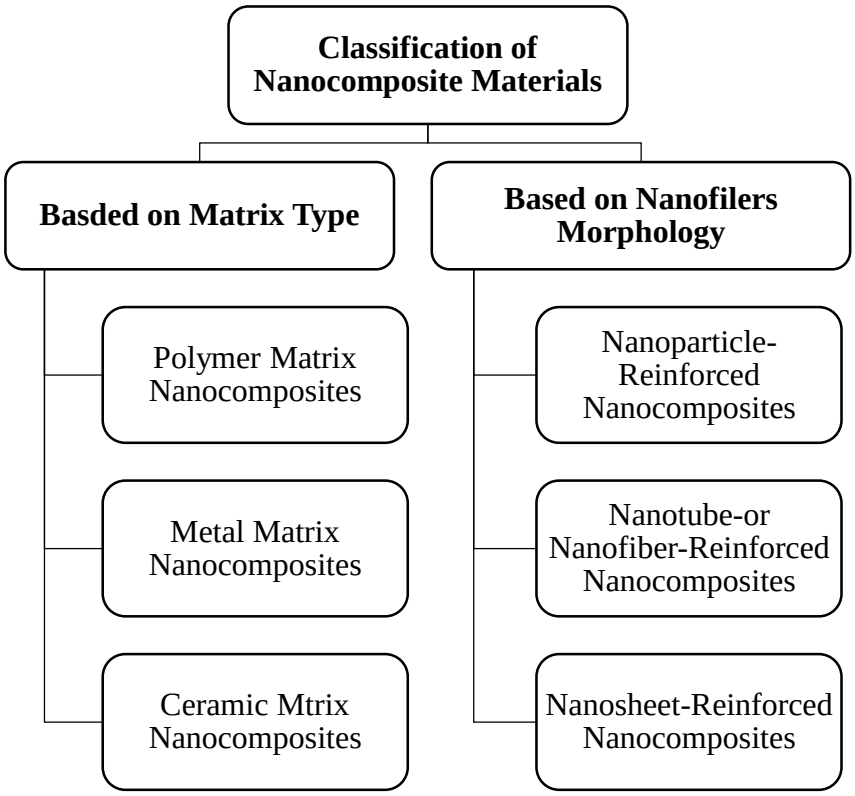

Figure 2.3 : Hierarchical classification of Nanocomposite materials

2.3.2.1. Classification based on matrix material

Metal-Based Nanocomposites

Metallic nanocomposites are typically developed by dispersing nanoparticles such as silicon carbide (SiC), aluminum oxide (Al_2O_3), or carbon nanotubes (CNTs) within a metal matrix. The primary goal is to enhance the material's hardness, stiffness, and wear resistance without significantly increasing its weight. For instance, aluminum-based nanocomposites reinforced with CNTs or ceramic particles are widely utilized in aerospace and defense

sectors, where lightweight but mechanically robust materials are essential. Similarly, copper or silver-based nanocomposites demonstrate notable electrical and antimicrobial properties, enabling their application in microelectronics and biomedical devices. Unlike traditional metal alloys, the nanoscale reinforcements in these materials offers substantial improvements at lower filler loadings, minimizing processing challenges and maintaining ductility. [80]

Ceramic-Based Nanocomposites

Traditional ceramics are valued for their high hardness, thermal resistance, and chemical stability, but their inherent brittleness limits their structural applications. To overcome these limitations, nanocomposite strategies have been developed by embedding nanoscale reinforcements such as zirconia (ZrO_2), boron nitride (BN), and silicon carbide (SiC) into ceramic matrices. The addition of these nanofillers not only improves fracture toughness through mechanisms like crack deflection and bridging but also enhances high-temperature mechanical performance. For example, zirconia-alumina nanocomposites are used in orthopedic implants due to their biocompatibility and resistance to mechanical degradation under cyclic loading. Meanwhile, BN- or SiC-reinforced ceramics are widely applied in thermal barrier coatings, cutting tools, and high-stress components for aerospace engines. [81]

Polymer-Based Nanocomposites

Among the various nanocomposite systems, polymer-based nanocomposites have received the most research attention due to the inherent processability, flexibility, and low density of polymers. Reinforcing polymers with nanomaterials like carbon nanotubes (CNTs), graphene, nanoclays, or metal nanoparticles introduces significant enhancements in mechanical strength, thermal stability, gas barrier properties, and electrical conductivity. For instance, CNT-reinforced epoxy systems are used in aerospace structures for their superior strength-to-weight ratios. Graphene-enhanced polymers find applications in flexible electronics and next-generation energy storage devices due to their high electron mobility and surface area. Additionally, polymer nanocomposites containing nanoclays or TiO_2 nanoparticles exhibit improved fire resistance and UV protection, making them suitable for automotive parts and packaging films. The tenability of both matrix and filler properties

allows for a high degree of customization, making these materials attractive for multifunctional applications. [82]

The key features and application domains of these nanocomposite systems are consolidated in Table 2.2 for clarity.

Table 2.2 Matrix-based classification of nanocomposites with representative nanofillers and applications

Matrix Type	Common Nanofillers	Key Properties Enhanced	Typical Applications
Metal Matrix	SiC, Al_2O_3, CNTs	Hardness, thermal stability, wear resistance	Aerospace, electronics, magnetic devices
Ceramic Matrix	ZrO_2, BN, SiC	Fracture toughness, thermal endurance	Biomedical implants, cutting tools, aerospace
Polymer Matrix	CNTs, graphene, nanoclays, metal nanoparticles	Strength, barrier properties, conductivity	Automotive, packaging, electronics, coatings

2.3.2.2. Classification based on nanofiller morphology

An alternative yet highly relevant classification approach is based on the dimensional morphology of the nanofillers, which significantly affects the load transfer mechanism, dispersion behavior, and interaction with the matrix.

- Zero-dimensional (0D) nanofillers, such as spherical silica or titania nanoparticles, provide isotropic enhancement and are typically used to improve thermal and optical properties.

- One-dimensional (1D) nanofillers, such as carbon nanotubes or nanofibers, have high aspect ratios and deliver superior mechanical strength and electrical conductivity due to efficient stress transfer along the fiber axis.

- Two-dimensional (2D) nanofillers, like graphene oxide or layered silicates, offer large surface areas and excellent barrier properties, enhancing flame resistance and mechanical integrity in polymer matrices.

- Three-dimensional (3D) nanostructured fillers (e.g., metal-organic frameworks or hybrid nanonetworks) provide multi-directional reinforcement and hierarchical porosity, applicable in catalysis and energy storage.

2.4 Carbon Nanotubes (CNTs) as a reinforcement

Carbon nanotubes (CNTs) are among the most extensively studied and utilized nanofillers in advanced composite materials due to their extraordinary mechanical, electrical, and thermal properties. Since their discovery by Iijima in 1991 [1], CNTs have attracted considerable attention as reinforcement agents in nanocomposites, especially in polymer-based systems. Their nanoscale dimensions, high aspect ratio, and unique graphitic structure make them ideal candidates for improving the performance of both structural and functional materials.

2.4.1 Structure and properties of CNTs

CNTs are hollow cylindrical structures composed of rolled-up graphene sheets. They exist in two primary forms:

- Single-Walled CNTs (SWCNTs): Consist of a single graphene layer rolled into a tube, exhibiting superior flexibility and electrical conductivity.
- Multi-Walled CNTs (MWCNTs): Comprise multiple concentric graphene tubes, providing higher mechanical strength and thermal stability.

2.4.1.1. Single-Walled Carbon Nanotubes (SWCNTs)

Single-Walled Carbon Nanotubes (SWCNTs) are cylindrical nanostructures consisting of a single layer of graphene rolled into a seamless tube as illustrated in Figure (2.4). They have diameters ranging from 0.4 to 2 nm and can be several micrometers in length, resulting in an extremely high aspect ratio. Their atomic structure can vary, leading to different electronic and mechanical properties.

SWCNTs can be categorized based on their chirality (as depicted in Figure 2.4), which defines how the graphene sheet is rolled:

- Armchair (n = m): Metallic in nature, excellent electrical conductors.

- Zigzag (m = 0): Can be metallic or semiconducting depending on the chiral angle.
- Chiral (n ≠ m): Usually semiconducting, widely used in nanoelectronics.

The electronic properties of SWCNTs depend on their chirality, with some behaving as metallic conductors and others as semiconductors. This makes them highly useful in nanoelectronics, transistors, and sensors.

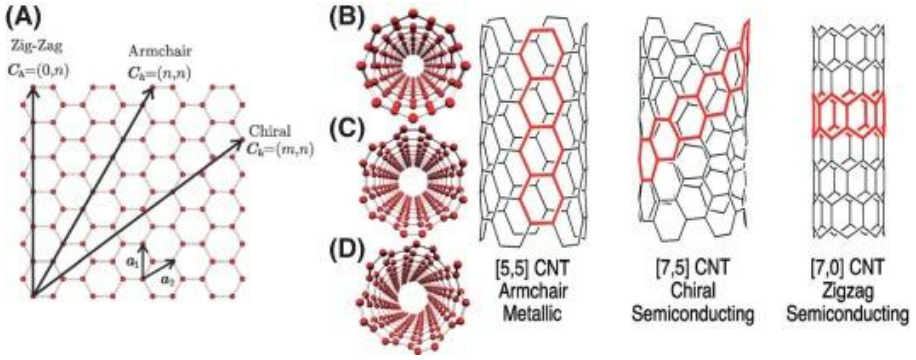

Figure 2.4 : Structures of SWCNTs [83]

2.4.1.2. Multi-Walled Carbon Nanotubes (MWCNTs)

Multi-Walled Carbon Nanotubes (MWCNTs) consist of multiple concentric layers of graphene sheets rolled into cylindrical tubes. These layers are separated by a distance of approximately 0.34 nm, similar to the interlayer spacing in graphite. MWCNTs typically have an outer diameter of 10-100 nm and can be several micrometers long (Figure 2.5).

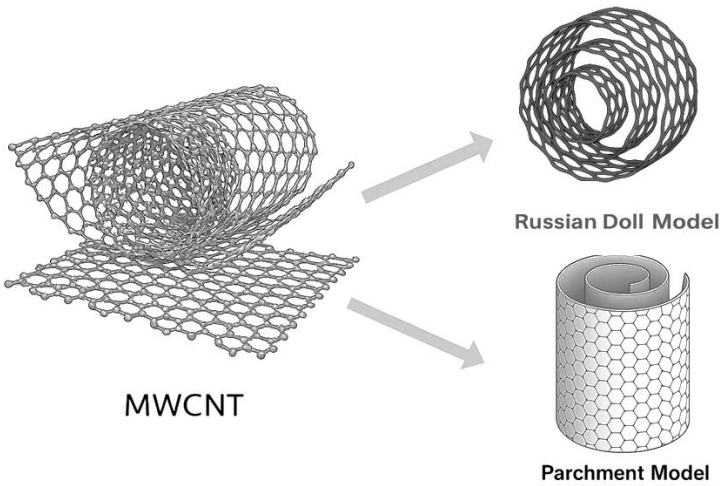

Figure 2.5 : Structures of MWCNTs

There are two main structural models for MWCNTs:

- Russian Doll Model: The graphene layers are arranged concentrically, resembling a nested structure.

- Parchment Model: A single graphene sheet is rolled multiple times like a scroll.

2.5 Functionally Graded Materials (FGMs)

Functionally Graded Materials (FGMs) are a class of advanced composites characterized by a continuous spatial variation in composition, microstructure, or properties, resulting in tailored performance for specific applications. FGMs were initially developed to withstand extreme thermal environments, where high heat loads induce significant thermal stresses. To address this challenge, a combination of ceramic and metallic constituents with a continuous gradient in composition and properties was introduced, enabling FGMs to endure temperatures up to 2000 K and thermal gradients as high as 1000 K [84].

2.5.1 Microstructural gradient and connectivity in FGMs

Unlike homogeneous materials, the properties of Functionally Graded Materials (FGMs) are not solely dictated by their compositional variations, but also depend significantly on the connectivity and distribution of their internal phases. This microstructural evolution, governed by the volume fraction and spatial arrangement of the constituent phases, critically influences the global behavior of the material.

Figure 2.6 illustrates a schematic representation of typical microstructures observed in FGMs as the concentration of the second phase increases:

At low volume fractions (Figure 2.6 a), the second phase appears as isolated particles dispersed within a continuous matrix.

As the volume fraction increases (Figure 2.6 b), these particles begin to form clusters or aggregates.

Beyond a critical concentration threshold (Figure 2.6 c-e), a microstructural transition occurs, leading to long-range connectivity of the second phase. This results in a percolated network where the second phase becomes continuous throughout the material.

This transition has a pronounced effect on the effective properties of the composite, such as thermal and electrical conductivity, mechanical stiffness, or permeability. Even minor compositional changes can result in significant property shifts, due to the connectivity threshold being crossed. Understanding this microstructural evolution is vital in the design of FGMs for tailored performance.

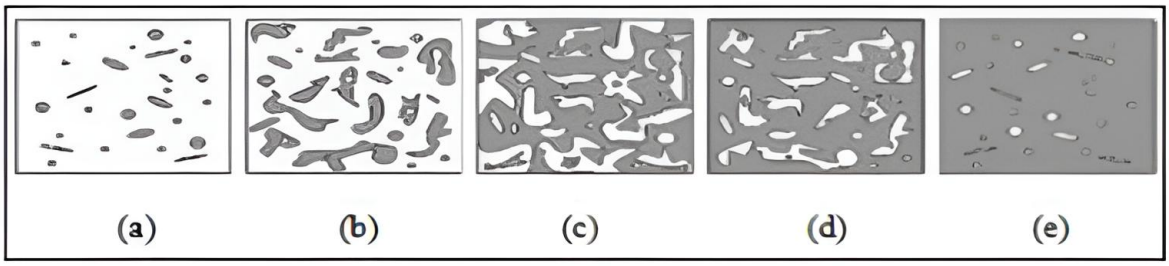

Figure 2.6 : Schematic change of the microstructure in a FGM profile

2.5.2 Common material combinations in FGMs

To illustrate the wide range of applications and advantages of FGMs, Table 2.3 presents typical combinations of constituent materials, categorized by type, along with their corresponding application areas and key performance benefits. These combinations demonstrate how strategic material gradation can be tailored to meet diverse functional requirements in advanced engineering systems.

Table 2.3 Representative material combinations in FGMs and their engineering application

Material 1	**Material 2**	**FGM Type**	**Typical Applications**	**Key Benefits**
Zirconia	Stainless Steel	Ceramic–Metal	Thermal coatings, aerospace	High-temperature resistance, mechanical toughness
Alumina	Titanium	Ceramic–Metal	Engine components, fusion reactors	Thermal insulation, corrosion resistance
Copper	Aluminum	Metal–Metal	Heat exchangers, electronics	Good conductivity, lightweight
Nickel	Titanium (NiTi)	Metal–Metal	Actuators, biomedical implants	Shape memory effect, strength
PLA	Hydroxyapatite (HA)	Polymer–Ceramic	Bone scaffolds, orthopedic implants	Biocompatibility, stiffness gradient
Polyimide	Silver	Polymer–Metal	Flexible electronics, sensors	Flexibility, electrical conductivity
Epoxy	CNT	CNT-Reinforced Nano-FGM	Aerospace panels, electronics	High strength, multi-functionality, lightweight
PEEK	CNT	CNT-Reinforced Nano-FGM	Structural components, microelectronics	Thermal stability, enhanced stiffness

2.6 Advantages of composite materials

High strength-to-weight ratio: Composites are renowned for offering exceptional strength and stiffness with a significantly lower weight compared to conventional materials

such as metals. This advantage is critical in aerospace, automotive, and sporting goods applications where weight reduction directly translates to improved performance and fuel efficiency.

Tailorability: The properties of composite materials can be engineered by varying the type, orientation, and volume fraction of the reinforcement. This design flexibility allows engineers to customize materials for specific load-bearing, thermal, or environmental conditions, thus optimizing performance for targeted applications.

Improved thermal stability: Certain composites can maintain their mechanical integrity over a wide range of temperatures. For instance, ceramic matrix composites are used in high-temperature environments due to their excellent thermal stability and resistance to thermal shock.

Corrosion and fatigue resistance: Composites generally exhibit excellent resistance to corrosion, chemical attack, and fatigue. These properties are particularly beneficial in harsh environmental conditions, such as marine or chemical processing applications, where traditional metals might degrade quickly.

Design flexibility: The manufacturing processes for composites, such as hand lay-up, filament winding, or pultrusion, allow for the creation of complex shapes that would be difficult or uneconomical to produce using traditional materials. This flexibility enables innovative designs that maximize structural efficiency and performance.

Damping capacity: Composite materials often exhibit superior vibration damping properties compared to metals. This characteristic can reduce noise, vibration, and harshness in dynamic applications, thereby enhancing comfort and longevity in structures and vehicles.

Energy absorption: In applications requiring impact resistance, composites can be designed to absorb energy effectively, which is crucial in automotive crashworthiness and protective gear.

2.7 Challenges and limitations of composite and nanocomposite materials

While composite materials offer superior mechanical properties, lightweight structures, and resistance to corrosion, they are not without challenges that impact their performance, durability, and cost-effectiveness. These challenges broadly fall under three main categories:

manufacturing complexity, mechanical durability, and environmental susceptibility. Table 2.4 provides an overview of these issues.

Among these, environmental susceptibility, particularly to hygrothermal conditions, is of primary importance in the context of this work. Exposure to moisture and thermal cycles significantly affects the performance of CNT-reinforced polymer composites, leading to long-term degradation mechanisms such as interfacial debonding, matrix plasticization, and microcracking. These effects compromise structural integrity, dimensional stability, and service life, especially in aerospace, marine, and civil infrastructure applications. Understanding and mitigating such environmental impacts is therefore critical for the reliable use of nanocomposites in real-world conditions.

Table 2.4 Summary of challenges in composite and nanocomposite materials

Challenge Category	Specific Issues	Implications
Manufacturing Challenges	▪ Nanofiller agglomeration ▪ Poor dispersion ▪ Weak interfacial bonding ▪ High cost and scalability limitations ▪ Integration with existing processing methods	▪ Reduced mechanical performance ▪ Variability in material properties ▪ Limited industrial adoption
Durability & Mechanical Limitations	▪ Fatigue and creep ▪ Delamination and cracking ▪ Anisotropic behavior	▪ Unpredictable long term behavior ▪ Structural reliability ▪ concerns
Environmental Susceptibility	▪ Hygrothermal degradation ▪ UV and oxidative damage ▪ Chemical incompatibility and corrosion	▪ Property degradation over time ▪ Premature failure in harsh service conditions

2.8 Hygrothermal effects on CNT-reinforced composites

Hygrothermal effects refer to the combined influence of moisture and temperature on the structural integrity and performance of composite materials. In many real-world applications, CNT-reinforced composites are exposed to high humidity, temperature

fluctuations, and even liquid immersion, all of which can lead to material degradation over time. Understanding how hygrothermal environments affect composite properties is essential for industries where long-term durability is critical.

CNTs have been widely studied as reinforcements due to their exceptional mechanical, electrical, and thermal properties. However, their effectiveness under hygrothermal conditions remains a significant concern. This section discusses the mechanisms by which hygrothermal exposure affects CNT-reinforced materials.

2.8.1 Mechanisms of moisture absorption

Moisture can penetrate composite materials through several mechanisms, depending on the fiber-matrix interface, the degree of porosity, and the presence of microcracks. The primary pathways for moisture absorption include:

- Capillary Transport: Water enters the composite through microscopic cracks and defects, particularly at fiber-matrix interfaces.
- Diffusion Through the Polymer Matrix: Water molecules move through the polymer chains, leading to swelling and plasticization of the matrix.
- Interfacial Absorption: The fiber-matrix interface can serve as a site for water accumulation, weakening adhesion and promoting delamination.

2.8.2 Effects of moisture on composite properties [85]

Mechanical degradation

Water absorption can lead to a significant reduction in the tensile strength, flexural modulus, and impact resistance of composites. This is mainly due to matrix softening, fiber swelling, and weakening of fiber-matrix interactions. In CNT-reinforced composites, moisture accumulation at the CNT-matrix interface can reduce load transfer efficiency, leading to premature failure.

Swelling and dimensional changes

The absorbed moisture can cause dimensional expansion of the matrix, generating internal stresses that lead to microcracking. These effects are particularly problematic in thermoplastic-based CNT composites, where swelling can compromise structural stability in applications requiring tight tolerances.

Plasticization and softening

Moisture can act as a plasticizer, reducing the glass transition temperature (Tg) of the polymer matrix. This results in lower stiffness and increased ductility, which may be detrimental for load-bearing applications. The softening effect also impacts CNT dispersion, potentially leading to re-agglomeration of CNTs over time.

Interfacial debonding and delamination

Prolonged moisture exposure weakens adhesion between CNTs and the polymer matrix, leading to interfacial debonding. As a result, delamination occurs, reducing the overall mechanical performance of the composite. This issue is particularly critical in aerospace and marine applications, where prolonged moisture exposure is inevitable.

2.8.3 Thermal effects on composite materials

Thermal expansion and contraction

Composites are susceptible to thermal expansion mismatch between the CNTs and the matrix. CNTs have a low thermal expansion coefficient, whereas polymer matrices expand significantly with temperature. This difference can induce residual stresses, leading to microcracking and loss of mechanical integrity over time.

Glass transition temperature (Tg) shift

Elevated temperatures can cause a reduction in Tg, softening the polymer matrix and reducing its load-bearing capacity. When combined with moisture absorption, this effect is amplified, leading to accelerated degradation of CNT-reinforced composites in high-temperature, humid environments.

Creep and stress relaxation

Creep, the slow deformation of a material under constant stress, is exacerbated at high temperatures. CNT reinforcements can reduce creep effects by restricting polymer chain mobility, but their efficiency is reduced in humid conditions, where interfacial bonding deteriorates [86].

Oxidation and thermal degradation of CNTs

CNTs have excellent thermal stability, but at temperatures above 500°C, they begin to oxidize, forming defects that reduce their mechanical properties. In CNT-reinforced

composites, prolonged high-temperature exposure can lead to CNT degradation, impacting overall performance [87].

2.8.4 Combined hygrothermal effects on CNT-reinforced composites

When moisture and temperature act together, their combined effects accelerate material degradation. Some key consequences include:

- Increased rate of moisture absorption: Elevated temperatures enhance moisture diffusion, leading to faster degradation.
- Reduction in load transfer efficiency: CNT-matrix interactions weaken under hygrothermal aging, reducing reinforcement efficiency.
- Accelerated aging and loss of stiffness: The combined action of heat and moisture reduces the long-term durability of the composite.

These effects make hygrothermal resistance a key design challenge for CNT-based composites in extreme environments.

2.9 Conclusion

This chapter has presented an in-depth overview of composite and nanocomposite materials, focusing on carbon nanotube (CNT)-reinforced systems. It covered their classification, structural advantages, and potential applications, along with the role of functionally graded materials (FGMs) in enhancing material performance.

Key challenges, including complex manufacturing processes, interfacial limitations, and environmental degradation (particularly under hygrothermal exposure) have been outlined. The final sections detailed the mechanisms by which moisture and temperature variations affect the mechanical behavior of CNT-reinforced composites, emphasizing the need to account for such effects in design and analysis.

The insights gained from this chapter provide a foundational understanding for the modeling and performance evaluation of CNT-based nanocomposites under real-world environmental conditions, as will be explored in the subsequent chapters.

CHAPTER 3: THEORETICAL FRAMEWORK AND CONSTITUTIVE LAW FOR NANOCOMPOSITE PLATES

3.1 Introduction

This chapter aims to present the geometric characteristics of nanocomposite plates while considering different types of nanofillers distributions. Additionally, it explores the mechanical properties of nanocomposites by discussing various approaches for predicting their effective mechanical behavior. The theoretical formulation is developed within the framework of First-Order Shear Deformation Theory (FSDT) to define the kinetic energy, strain energy, and external forces acting on both isotropic and orthotropic plates. Furthermore, the stress-strain relationships for these plates are derived and analyzed to establish a comprehensive understanding of their mechanical response.

3.2 Geometric characterizations of FG-CNTRC plates

Let us consider a CNTRC plate composed of an isotropic polymer matrix and CNT fillers with dimensions of length *a*, width *b*, and thickness *h* within a Cartesian coordinate system (*x*, *y*, *z*), as depicted in Figure 3.1. The FG-CNTRC plate is assumed to be divided into N_L layers, each with an equal thickness of $h_L = h / N_L$. The CNT volume fraction across the nanocomposite plate's thickness can be Uniformly Distributed (UD) or Functionally Graded (FG). In the case of UD-CNTRC plates, the volume fraction of the nano-reinforcements is evenly distributed throughout all layers. In contrast, for FG-CNTRC plates, the CNT volume fraction varies across the thickness according to specific distribution patterns. In this study, four prevalent distributions are considered: FG-V, FG-A, FG-O, and FG-X, as illustrated in Figure 3.2.

In FG-V, CNTs are concentrated in the top layer and gradually decrease toward the bottom. Conversely, FG-A distribution concentrates CNTs in the bottom layers, with a gradual decrease toward the top. The FG-O distribution features a CNT-rich middle layers, with symmetric linear reductions toward the top and bottom surfaces. Conversely, the FG-X distribution is characterized by high CNT concentrations at the top and bottom surfaces, decreasing toward the mid-plane. These patterns are designed to enhance the mechanical

properties of the FG-CNTRC plates and optimize their performance for specific applications and environmental conditions.

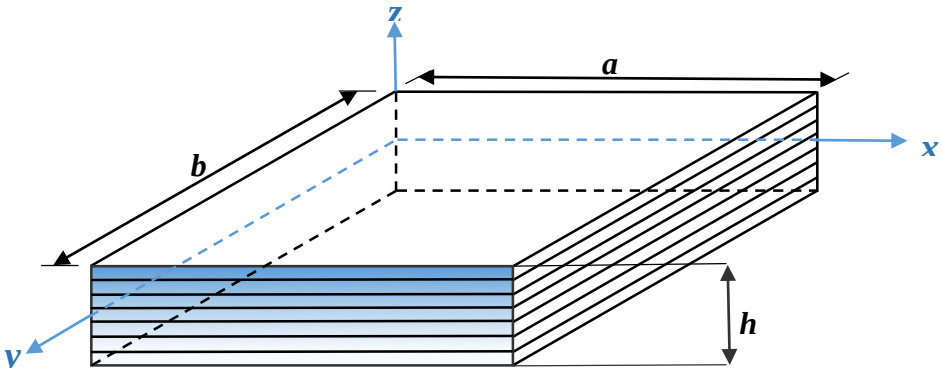

Figure 3.1 : Geometry of functionally graded plate.

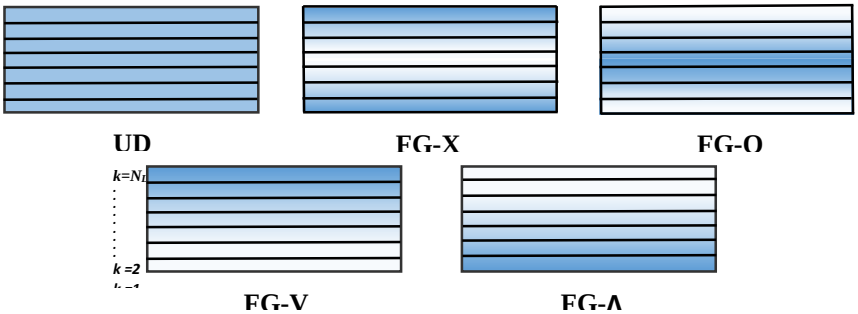

Figure 3.2 : Distribution patterns

The mathematical expressions of the CNT volume fraction ($V_{CNT}^{(k)}$) of the k^{th} layer ($k = 1, 2, 3, ..., N_L$) for UD and FG CNTRC are given as [88]:

$$UD:\ V_{CNT}^{(k)} = V_{CNT}^{*} \tag{3.1}$$

$$\text{FG-X:}\ V_{CNT}^{(k)} = (1+P_{in})\left(\frac{|2k-N_L-1|}{N_L}\right)^{P_{in}} V_{CNT}^{*} \tag{3.2}$$

$$\text{FG-O:}\ V_{CNT}^{(k)} = (1+P_{in})\left(1-\frac{|2k-N_L-1|}{N_L}\right)^{P_{in}} V_{CNT}^{*} \tag{3.3}$$

$$\text{FG-V:}\ V_{CNT}^{(k)} = (1+P_{in})\left(\frac{k-0.5}{N_L}\right)^{P_{in}} V_{CNT}^{*} \tag{3.4}$$

$$\text{FG-}\Lambda\text{:}\ V_{CNT}^{(k)} = (1+P_{in})\left(\frac{0.5-k+N_L}{N_L}\right)^{P_{in}} V_{CNT}^{*} \tag{3. 5}$$

Where, the volume fraction of CNTs is given as [89]:

$$V_{CNT}^{*} = \frac{w^{CNT}}{(1-w^{CNT})(\rho^{CNT}/\rho^{m}) + w^{CNT}} \tag{3.6}$$

The power-law index P_{in} is a key parameter in modeling the material distribution in FGMs and nanocomposite structures. It governs the variation of material properties across a structure, such as the volume fraction of reinforcements like CNTs in FG distributions. This index is used to define both linear ($P_{in}=1$) and non-linear ($P_{in}>1$) distributions of nano-reinforcements across the nano-composite plate thickness.

- For $P_{in}=0$: The reinforcement content is uniformly distributed over the thickness.
- For $P_{in}=1$: The reinforcement content varies linearly through the thickness.
- For $P_{in}>1$: The reinforcement is more concentrated in one region (e.g., near the top or bottom surface), leading to a nonlinear gradient in material properties.

w^{CNT} is the CNT's weight fraction, ρ^{CNT} and ρ^{m} are the densities of CNTs and matrix, respectively.

The relation between the matrix volume fraction ($V_m^{(k)}$) and $V_{CNT}^{(k)}$ is given as:

$$V_{CNT}^{(k)} + V_m^{(k)} = 1 \tag{3.7}$$

3.3 Mechanical characterizations of FG-CNTRC plates

3.3.1 Extended rule of mixtures

The extended rule of mixtures is employed to estimate the overall properties of nanocomposite structures based on the properties and volume fractions of their constituents (typically fibers and matrix). Unlike the classical rule which assumes perfect alignment, full load transfer, and idealized conditions, the extended rule of mixtures introduces additional efficiency factors to account for real-world imperfections. These factors typically include: fiber orientation, fiber length, and additional factors that reflect the quality of the fiber-matrix interface, the distribution of fibers, or other geometric considerations.

In the case of CNTRC, these efficiency factors are particularly important to capture nanoscale effects, such as non-uniform dispersion, orientation misalignment, and imperfect interfacial bonding.

According to the extended rule of mixture, the effective Young's modulus in longitudinal ($E_{11}^{(k)}$) and transverse ($E_{22}^{(k)}$) directions and shear modulus ($G_{12}^{(k)}$) of the k^{th} CNTRC layer are expressed as follows [22], [90]–[92]:

$$E_{11}^{(k)} = \eta_1 V_{CNT}^{(k)} E_{11}^{CNT} + V_m^{(k)} E^m \tag{3.8}$$

$$\frac{\eta_2}{E_{22}^{(k)}} = \frac{V_{CNT}^{(k)}}{E_{22}^{CNT}} + \frac{V_m^{(k)}}{E^m} \tag{3.9}$$

$$\frac{\eta_3}{G_{12}^{(k)}} = \frac{V_{CNT}^{(k)}}{G_{12}^{CNT}} + \frac{V_m^{(k)}}{G^m} \tag{3.10}$$

According to the same micromechanics model (i.e. extended rule of mixture) the Poisson's ratio ($\nu_{12}^{(k)}$) and masse density ($\rho_{12}^{(k)}$) of the k^{th} CNTRC layer are given as follows [66], [93]:

$$\nu_{12}^{(k)} = V_{CNT}^{*} \nu_{12}^{CNT} + V_m^{(k)} \nu^m \tag{3.11}$$

$$\rho_{12}^{(k)} = V_{CNT}^{*} \rho_{12}^{CNT} + V_m^{(k)} \rho^m \tag{3.12}$$

Where, ρ^m, ν^m, E^m, and G^m are masse density, Poisson's ratio, Young's and shear modulus of the matrix, respectively.

η_1, η_2 and η_3 are the CNT efficiency parameters.

3.3.2 Thermal and moisture expansion coefficients

In materials science, the thermal expansion coefficient (often denoted by α) serves as a quantitative measure of how a material's dimensions (in length, area, or volume) change with temperature variations. It represents the rate at which a material expands or contracts per unit length per degree of temperature change.

In a similar manner, the moisture expansion coefficient, often termed the hygroscopic expansion coefficient, quantifies the dimensional variations resulting from moisture absorption or desorption. This parameter is particularly crucial for materials that exhibit significant sensitivity to humidity fluctuations, such as polymers, wood, and composites containing hygroscopic constituents.

Thermal and moisture expansion coefficients (i.e. $\alpha^{(k)}$ and $\beta^{(k)}$) in longitudinal ($\alpha_{11}^{(k)}$, $\beta_{11}^{(k)}$) and transverse ($\alpha_{22}^{(k)}$, $\beta_{22}^{(k)}$) directions of the k^{th} CNTRC plate layer are assumed to be graded in the thickness direction and are expressed as follows [65]:

$$\alpha_{11}^{(k)} = V_{CNT}^{(k)}\alpha_{11}^{CNT} + V_m^{(k)}\alpha^m \tag{3.13}$$

$$\alpha_{22}^{(k)} = \left(1+\nu_{12}^{CNT}\right)V_{CNT}^{(k)}\alpha_{22}^{CNT} + \left(1+\nu^m\right)V_m^{(k)}\alpha^m - \nu_{12}^{CNT}\alpha_{11}^{(k)} \tag{3.14}$$

$$\beta_{11}^{(k)} = V_m^{(k)}\beta^m \tag{3.15}$$

$$\beta_{22}^{(k)} = \left(1+\nu^m\right)V_m^{(k)}\beta^m - \nu_{12}^{CNT}\beta_{11}^{(k)} \tag{3.16}$$

α_{11}^{CNT}, α_{22}^{CNT} are the thermal expansion coefficients of the CNTs in the longitudinal and transverse directions, respectively. α^m and β^m are the thermal and moisture expansion coefficients of the matrix, respectively.

3.4 First-Order Shear Deformation Theory (FSDT)

3.4.1 Displacement field

To overcome the limitations of Classical Plate Theory (CPT), which neglects transverse shear and normal deformations, several researchers have developed alternative theories that account for shear deformation effects. Reissner [94], [95] pioneered a consistent stress-based plate theory incorporating shear deformations, while Hencky [96] and Mindlin [97] further advanced these concepts. Notably, Mindlin introduced a displacement-based first-order shear deformation theory (FSDT), which provides a practical balance between computational efficiency and accuracy in predicting the global behavior of thin and moderately thick laminated composite plates, although it may not capture localized effects with high fidelity. The combined Hencky–Mindlin framework, widely recognized as FSDT, has subsequently been refined through the use of shear correction factors [98], [99].

The displacement field of the FSDT is of the form [100] :

$$\begin{cases} u(x,y,z) = u_0(x,y) + z\theta_x(x,y) \\ v(x,y,z) = v_0(x,y) + z\theta_y(x,y) \\ w(x,y,z) = w_0(x,y) \end{cases} \tag{3.17}$$

Where,

u , v and w are displacements components in the directions *x, y* and *z*, respectively.

u_0 , v_0 and w_0 are displacements components on the mid-plane of the plate in the directions *x, y* and *z*, respectively.

$\theta_x(x, y)$ and $\theta_y(x, y)$ refer respectively to the rotations of the transverse normal about the *y* and *x* axes: $\theta_x = \dfrac{\partial w}{\partial z}$, $\theta_y = \dfrac{\partial w}{\partial z}$

3.4.2 Strain field

The strain field is derived from the displacement field.

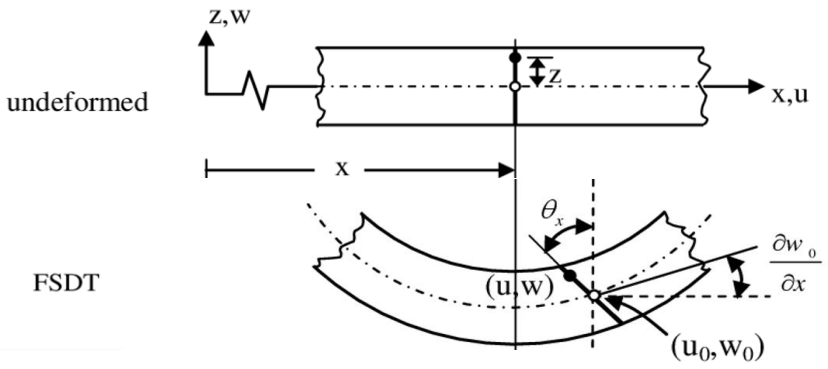

Figure 3.3 : Deformation of the plate according to FSDT

$$\begin{Bmatrix} \varepsilon_x \\ \varepsilon_y \\ \varepsilon_z \\ \gamma_{xy} \\ \gamma_{yz} \\ \gamma_{xz} \end{Bmatrix} = \begin{Bmatrix} \dfrac{\partial u}{\partial x} \\ \dfrac{\partial v}{\partial y} \\ \dfrac{\partial w}{\partial z} \\ \dfrac{\partial v}{\partial x} + \dfrac{\partial u}{\partial y} \\ \dfrac{\partial v}{\partial x} + \dfrac{\partial w}{\partial x} \\ \dfrac{\partial u}{\partial y} + \dfrac{\partial w}{\partial y} \end{Bmatrix} = \begin{Bmatrix} \varepsilon_{x0} + z\kappa_x \\ \varepsilon_{y0} + z\kappa_y \\ 0 \\ \gamma_{xy0} + z\kappa_{xy} \\ \theta_y + \dfrac{\partial w_0}{\partial y} \\ \theta_x + \dfrac{\partial w_0}{\partial x} \end{Bmatrix} = \begin{Bmatrix} \dfrac{\partial u_0}{\partial x} + z.\dfrac{\partial \theta_x}{\partial x} \\ \dfrac{\partial v_0}{\partial y} + z.\dfrac{\partial \theta_y}{\partial y} \\ 0 \\ \dfrac{\partial u_0}{\partial y} + \dfrac{\partial v_0}{\partial x} + z.\left(\dfrac{\partial \theta_x}{\partial y} + \dfrac{\partial \theta_y}{\partial x} \right) \\ \theta_y + \dfrac{\partial w_0}{\partial y} \\ \theta_x + \dfrac{\partial w_0}{\partial x} \end{Bmatrix} \tag{3.18}$$

Where,

$\varepsilon_{x0}, \varepsilon_{y0}, \gamma_{xy0}$ are the membrane strains that describe how the mid-plane of the plate stretches,

$\kappa_x, \kappa_y, \kappa_{xy}$ are the bending strains that describe the curvature of the plate due to flexural loading,

γ_{xz}, γ_{yz} are the transverse shear strains.

3.5 Strain-Stress relationship

The generalized Hooke's law extends the classical stress-strain relationship to anisotropic materials, such as those found in laminated composite plates. In a composite laminate, each layer (or ply) can have different material properties and orientations. As a result, the relationship between stress and strain must be defined separately for each ply. This is particularly important because of stress components.

To simplify the formulation and take full advantage of the orthotropic properties of the composite material, a local coordinate system (1, 2, 3) is defined for each ply. In this system:

- The 1-axis is aligned with the longitudinal fiber direction,
- The 2-axis is perpendicular to the fibers within the plane of the ply,
- The 3-axis is normal to the ply surface (through the thickness).

This local coordinate system not only simplifies the stiffness matrix $[Q]^{th}$ representation, but also ensures that the material properties (like the high stiffness along the fiber direction) are explicitly and accurately modeled. If needed, these local stress-strain relations can be transformed into the global coordinate system (*x, y, z*) to analyze the overall behavior of the laminated plate.

For each ply *k*, the constitutive relationship in the local (1,2,3) coordinate system is typically expressed as [101]:

$$\begin{Bmatrix} \sigma_1^{(k)} \\ \sigma_2^{(k)} \\ \tau_{12}^{(k)} \\ \tau_{23}^{(k)} \\ \tau_{13}^{(k)} \end{Bmatrix} = \begin{bmatrix} Q_{11}^{(k)} & Q_{12}^{(k)} & 0 & 0 & 0 \\ Q_{12}^{(k)} & Q_{22}^{(k)} & 0 & 0 & 0 \\ 0 & 0 & Q_{33}^{(k)} & 0 & 0 \\ 0 & 0 & 0 & Q_{44}^{(k)} & 0 \\ 0 & 0 & 0 & 0 & Q_{66}^{(k)} \end{bmatrix} \left(\begin{Bmatrix} \varepsilon_1^{(k)} \\ \varepsilon_2^{(k)} \\ \gamma_{12}^{(k)} \\ \gamma_{23}^{(k)} \\ \gamma_{13}^{(k)} \end{Bmatrix} - \Delta T \begin{Bmatrix} \alpha_{11}^{(k)} \\ \alpha_{22}^{(k)} \\ 0 \\ 0 \\ 0 \end{Bmatrix} - \Delta C \begin{Bmatrix} \beta_{11}^{(k)} \\ \beta_{22}^{(k)} \\ 0 \\ 0 \\ 0 \end{Bmatrix} \right) \tag{3.19}$$

Where,

$$Q_{11}^{(k)} = \frac{E_{11}^{(k)}}{1-\nu_{12}\nu_{21}}, Q_{22}^{(k)} = \frac{E_{22}^{(k)}}{1-\nu_{12}\nu_{21}}, Q_{12}^{(k)} = \frac{E_{11}^{(k)}\nu_{21}}{1-\nu_{12}\nu_{21}}, Q_{44}^{(k)} = G_{23}^{(k)}, Q_{55}^{(k)} = G_{13}^{(k)}, Q_{33}^{(k)} = G_{12}^{(k)} \quad (3.20)$$

Rewritten the Eq. (3.19) in a compact form as:

$$\{\sigma\}_{123}^{k} = [Q]^{k} \{\varepsilon - \alpha\Delta T - \beta\Delta C\}_{123}^{k} \quad (3.21)$$

Where:

- $\{\sigma\}^{k}$ is the vector of stress components in the k^{th} ply,
- $\{\varepsilon\}^{k}$ is the corresponding strain vector,
- $[Q]^{k}$ is the reduced stiffness matrix that characterizes the material behavior of that ply,
- ΔT is temperature increment from the reference temperature T_0 ($T_0 = 300K$), and $\Delta T = T - T_0$,
- ΔC is moisture increment from the reference moisture C_0.($C_0 = 0wt.\%$ of H_2O), and $\Delta C = C - C_0$.

To express the stress field in the global coordinate system (*x*, *y*, *z*), the local stresses must be transformed using the appropriate change-of-basis (or transformation) matrices, as depicted in Figure 3.4. This formulation allows for the analysis of the elastic behavior of the laminate by considering the different fiber orientations in each ply.

The corresponding stress state in the global coordinate system (*x*, *y*, *z*) can be written as:

$$\{\sigma\}_{xyz}^{k} = [T]\{\sigma\}_{123}^{k} \quad (3.22)$$

Where the transformation matrix $[T]$ for plane stress is defined as:

$$[T] = \begin{bmatrix} \cos^2\theta & \sin^2\theta & 0 & -\cos\theta\sin\theta & 0 & 0 \\ \sin^2\theta & \cos^2\theta & 0 & \cos\theta\sin\theta & 0 & 0 \\ 0 & 0 & 1 & 0 & 0 & 0 \\ 2\cos\theta\sin\theta & -2\cos\theta\sin\theta & 0 & \cos^2\theta - \sin^2\theta & 0 & 0 \\ 0 & 0 & 0 & 0 & \cos\theta & \sin\theta \\ 0 & 0 & 0 & 0 & -\sin\theta & \cos\theta \end{bmatrix} \quad (3.23)$$

θ is the angle between the (1,2) coordinate system (aligned with the material or fiber directions) and the (*x*, *y*) coordinate system (the global reference frame).

Thus, the strain field in the global coordinate system becomes:

$$\{\varepsilon\}_{xyz}^{k} = [T']\{\varepsilon\}_{123}^{k} \tag{3.24}$$

Where $[T']$ is the strain transformation matrix, given as:

$$[T'] = \begin{bmatrix} \cos^2\theta & \sin^2\theta & 0 & -2\cos\theta\sin\theta & 0 & 0 \\ \sin^2\theta & \cos^2\theta & 0 & 2\cos\theta\sin\theta & 0 & 0 \\ 0 & 0 & 1 & 0 & 0 & 0 \\ \cos\theta\sin\theta & -\cos\theta\sin\theta & 0 & \cos^2\theta-\sin^2\theta & 0 & 0 \\ 0 & 0 & 0 & 0 & \cos\theta & \sin\theta \\ 0 & 0 & 0 & 0 & -\sin\theta & \cos\theta \end{bmatrix} \tag{3.25}$$

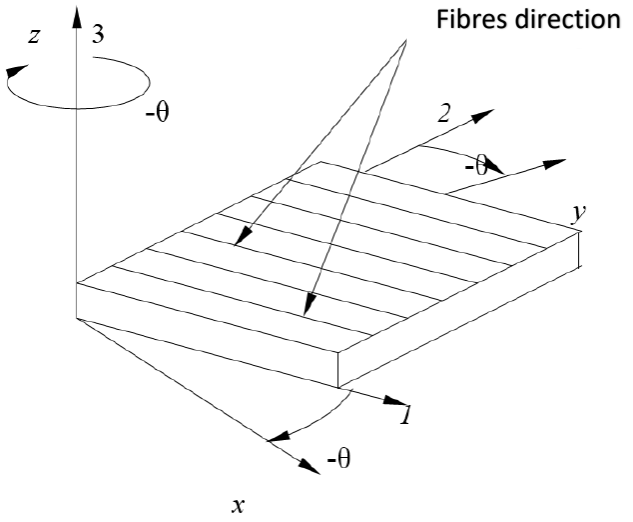

Figure 3.4 : Coordinate transformation in a composite ply

By substituting Eqs. (3.21) and (3.24) into Eq. (3.22), the stress-strain relationship becomes:

$$\{\sigma\}_{xyz}^{k} = \left[\overline{Q}\right]^{k} \{\varepsilon - \alpha\Delta T - \beta\Delta C\}_{xyz}^{k} \tag{3.26}$$

$\left[\overline{Q}\right]^{k}$ is the stiffness matrix of ply *k* expressed in the global coordinate system (*x*, *y*, *z*) expressed as:

$$\left[\overline{Q}\right]^{k} = [T]^{-1}[Q]^{k}[T'] \tag{3.27}$$

The elements of the $\left[\overline{Q}\right]^k$ matrix are defined as:

$$\overline{Q_{11}^{(k)}} = Q_{11}C^4 + 2\left(Q_{12} + 2\,Q_{66}\right)S^2\,C^2 + Q_{22}\,S^4 \tag{3.28}$$

$$\overline{Q_{12}^{(k)}} = \left(Q_{11} + Q_{22} - 4\,Q_{66}\right)S^2\,C^2 + Q_{12}\left(S^4 + C^4\right) \tag{3.29}$$

$$\overline{Q_{22}^{(k)}} = Q_{11}\,S^4 + 2\left(Q_{12} + 2\,Q_{66}\right)S^2\,C^2 + Q_{22}\,C^4 \tag{3.30}$$

$$\overline{Q_{13}^{(k)}} = \left(Q_{11} - Q_{12} + 2\,Q_{33}\right)S\,C^3 + \left(Q_{12} - Q_{22} + 2\,Q_{33}\right)Q_{22}\,S^3\,C \tag{3.31}$$

$$\overline{Q_{23}^{(k)}} = \left(Q_{11} - Q_{12} - 2\,Q_{33}\right)S^3\,C + \left(Q_{12} - Q_{22} + 2\,Q_{33}\right)Q_{22}\,S\,C^3 \tag{3.32}$$

$$\overline{Q_{33}^{(k)}} = \left(Q_{11} + Q_{22} - 2\,Q_{12} - 2\,Q_{33}\right)S^2\,C^2 + Q_{33}\left(S^4 + C^4\right) \tag{3.33}$$

$$\overline{Q_{44}^{(k)}} = Q_{11}\,C^2 + Q_{55}\,S^2 \tag{3.34}$$

$$\overline{Q_{45}^{(k)}} = \left(Q_{55} - Q_{44}\right)C.S \tag{3.35}$$

$$\overline{Q_{55}^{(k)}} = Q_{44}\,S^2 + Q_{55}\,C^2 \tag{3.36}$$

Where, S refers to ‘ $\sin\theta$ ’ and C to ‘ $\cos\theta$ ’ .

3.6 Stress, moment, and shear resultants for composite plate

In the analysis of laminated composite plates, the overall mechanical behavior is often described using resultant forces and moments rather than localized stresses. These resultants are obtained by integrating the stress components across the thickness of the laminate. They are typically classified into four categories:

3.6.1 Membrane Resultants (In-Plane Force Resultants)

Membrane resultants represent the in-plane forces per unit length acting on the mid-surface of the composite plate. These resultants are derived by integrating the normal and shear stresses through the laminate thickness:

$$N(x,y)=\begin{Bmatrix}N_x\\N_y\\N_{xy}\end{Bmatrix}=\sum_{k=1}^{N_L}\int_{Z_k}^{Z_{k+1}}\begin{Bmatrix}\sigma_x\\\sigma_y\\\tau_{xy}\end{Bmatrix}^k dz \tag{3.37}$$

$$\begin{Bmatrix}N_x\\N_y\\N_{xy}\end{Bmatrix}=\left(\begin{bmatrix}A_{11}&A_{12}&A_{16}\\A_{12}&A_{22}&A_{26}\\A_{16}&A_{26}&A_{66}\end{bmatrix}\begin{Bmatrix}\varepsilon_x^{(0)}\\\varepsilon_y^{(0)}\\\varepsilon_{xy}^{(0)}\end{Bmatrix}+\begin{bmatrix}B_{11}&B_{12}&B_{16}\\B_{12}&B_{22}&B_{26}\\B_{16}&B_{26}&B_{66}\end{bmatrix}\begin{Bmatrix}\varepsilon_x^{(1)}\\\varepsilon_y^{(1)}\\\varepsilon_{xy}^{(1)}\end{Bmatrix}\right)-\begin{Bmatrix}N_x^H\\N_y^H\\N_{xy}^H\end{Bmatrix} \tag{3.38}$$

3.6.2 Shear Resultants (Transverse Shear Forces)

Shear resultants represent the transverse shear forces per unit length that arise due to out-of-plane loading. Unlike isotropic plates, composite plates are more sensitive to transverse shear deformation, requiring special treatment in first-order and higher-order shear deformation theories.

$$Q(x,y)=\begin{Bmatrix}Q_x\\Q_y\end{Bmatrix}=\sum_{k=1}^{N_L}\int_{Z_k}^{Z_{k+1}}\begin{Bmatrix}Q_x\\Q_y\end{Bmatrix}^k\{e\}^k dz \tag{3.39}$$

Where *k* represents a layer composing the laminate.

$$\begin{Bmatrix}Q_x\\Q_y\end{Bmatrix}=\alpha_{ij}\begin{bmatrix}F_{44}&F_{45}\\F_{45}&F_{55}\end{bmatrix}\begin{Bmatrix}\gamma_{yz}^{(0)}\\\gamma_{xz}^{(0)}\end{Bmatrix} \tag{3.40}$$

Where,

$$\{e\}^k=\begin{Bmatrix}e_x\\e_y\\e_{xy}\end{Bmatrix}^k=[T_R]\begin{Bmatrix}\beta_{11}^{(k)}\\\beta_{22}^{(k)}\end{Bmatrix}\Delta C+[T_R]\begin{Bmatrix}\alpha_{11}^{(k)}\\\alpha_{22}^{(k)}\end{Bmatrix}\Delta T \tag{3.41}$$

In which,

$$[T_R]=\begin{bmatrix}\cos^2\theta&\sin^2\theta\\\sin^2\theta&\cos^2\theta\\\sin 2\theta&-\sin 2\theta\end{bmatrix} \tag{3.42}$$

The coefficients α_{ij} represent shear correction factors, which are introduced to enhance the accuracy of laminated plate theories by accounting for non-uniform transverse shear deformation. The determination of these factors has been extensively studied in the literature

[80]. Notably, Timoshenko, Reissner, and Mindlin proposed different values for these factors, taking them as 2/3, 5/6 et $\pi^2/12$, respectively. Among these, it has been observed that using a value of 5/6 yields the most satisfactory results, providing a balance between computational efficiency and accuracy in predicting the mechanical behavior of laminated composite plates.

3.6.3 Bending Moments (Flexural Resultants)

Bending moments describe the internal moments resultants per unit length generated due to the distribution (variation) of normal stresses across the thickness of the laminate. They primarily govern the bending and twisting responses of the laminated composite plate under mechanical, thermal, or hygrothermal loading.

$$M(x,y)=\begin{Bmatrix} M_x \\ M_y \\ M_{xy} \end{Bmatrix}=\sum_{k=1}^{N_L}\int_{Z_k}^{Z_{k+1}}\begin{Bmatrix} \sigma_x \\ \sigma_y \\ \tau_{xy} \end{Bmatrix}^k z\,dz \tag{3.43}$$

$$\begin{Bmatrix} M_x \\ M_y \\ M_{xy} \end{Bmatrix}=\left(\begin{bmatrix} B_{11} & B_{12} & B_{16} \\ B_{12} & B_{22} & B_{26} \\ B_{16} & B_{26} & B_{66} \end{bmatrix}\begin{Bmatrix} \varepsilon_x^{(0)} \\ \varepsilon_y^{(0)} \\ \varepsilon_{xy}^{(0)} \end{Bmatrix}+\begin{bmatrix} D_{11} & D_{12} & D_{16} \\ D_{12} & D_{22} & D_{26} \\ D_{16} & D_{26} & D_{66} \end{bmatrix}\begin{Bmatrix} \varepsilon_x^{(1)} \\ \varepsilon_y^{(1)} \\ \varepsilon_{xy}^{(1)} \end{Bmatrix}\right)-\begin{Bmatrix} M_x^H \\ M_y^H \\ M_{xy}^H \end{Bmatrix} \tag{3.44}$$

The stiffness elements of the plate are defined as:

$$(A_{ij},B_{ij},D_{ij})=\sum_{k=1}^{N_L}\int_{Z_k}^{Z_{k+1}}Q_{ij}^{(k)}\left(1,z,z^2\right)dz \tag{3.45}$$

$$F_{ij}=\sum_{k=1}^{N_L}\int_{Z_k}^{Z_{k+1}}Q_{ij}^{(k)}dz\,,\quad (i,j=1,2,6) \tag{3.46}$$

3.6.4 Hygrothermal Force Resultants

In-plane hygrothermal force resultants (N_x^H,N_y^H,N_{xy}^H) and hygrothermal moment resultants (M_x^H,M_y^H,M_{xy}^H) of the k^{th} layer are given as follows [101]:

$$\begin{Bmatrix} N_x^H \\ N_y^H \\ N_{xy}^H \end{Bmatrix}^k = \sum_{k=1}^{N_L} \int_{Z_k}^{Z_{k+1}} \left[\overline{Q}_{ij}\right]^k \begin{Bmatrix} e_x \\ e_y \\ e_{xy} \end{Bmatrix}^k dz \tag{3.47}$$

$$\begin{Bmatrix} M_x^H \\ M_y^H \\ M_{xy}^H \end{Bmatrix}^k = \sum_{k=1}^{N_L} \int_{Z_k}^{Z_{k+1}} \left[\overline{Q}_{ij}\right]^k \begin{Bmatrix} e_x \\ e_y \\ e_{xy} \end{Bmatrix}^k z dz \tag{3.48}$$

3.7 Constitutive equation

By combining the Equations (3.38, 3.39, 3.43, 3.47, 3.48), we obtained:

$$\begin{Bmatrix} N_x \\ N_y \\ N_{xy} \\ M_x \\ M_y \\ M_{xy} \\ Q_x \\ Q_y \end{Bmatrix} = \begin{bmatrix} A_{11} & A_{12} & A_{16} & B_{11} & B_{12} & B_{16} & 0 & 0 \\ & A_{22} & A_{26} & B_{12} & B_{22} & B_{26} & 0 & 0 \\ & & A_{66} & B_{16} & B_{26} & B_{66} & 0 & 0 \\ & & & D_{11} & D_{12} & D_{16} & 0 & 0 \\ & & & & D_{22} & D_{26} & 0 & 0 \\ & & sym & & & D_{66} & 0 & 0 \\ & & & & & & F_{44} & F_{45} \\ & & & & & & & F_{55} \end{bmatrix} \begin{Bmatrix} \varepsilon_{x0} \\ \varepsilon_{y0} \\ \gamma_{xy0} \\ \kappa_x \\ \kappa_y \\ \kappa_{xy} \\ \gamma_{xz} \\ \gamma_{yz} \end{Bmatrix} - \begin{Bmatrix} N_x^H \\ N_y^H \\ N_{xy}^H \\ M_x^H \\ M_y^H \\ M_{xy}^H \\ 0 \\ 0 \end{Bmatrix} \tag{3.49}$$

Or in compact form:

$$\begin{Bmatrix} N \\ M \\ Q \end{Bmatrix} = [C] \begin{Bmatrix} \varepsilon_0 \\ \kappa \\ \gamma \end{Bmatrix} - \begin{Bmatrix} N^H \\ M^H \\ 0 \end{Bmatrix} \tag{3.50}$$

Where, [C] is the elasticity matrix, expressed as:

$$[C] = \begin{bmatrix} [A] & [B] & 0 \\ [B] & [D] & 0 \\ 0 & 0 & [F] \end{bmatrix} \tag{3.51}$$

3.8 Derivation of Fundamental Equations for Laminated Plates

To establish the fundamental equations governing the behavior of laminated plates, it is essential to consider the dynamic equilibrium conditions. These equations can be derived by

formulating the equilibrium conditions of an infinitesimal plate element, accounting for internal resultants, external loads, and inertial effects.

$$\begin{aligned}
\frac{\partial \sigma_x}{\partial x}+\frac{\partial \tau_{xy}}{\partial y}+\frac{\partial \tau_{xz}}{\partial z}+f_x&=\rho a_x\\
\frac{\partial \tau_{xy}}{\partial x}+\frac{\partial \sigma_y}{\partial y}+\frac{\partial \tau_{yz}}{\partial z}+f_y&=\rho a_y\\
\frac{\partial \tau_{xz}}{\partial x}+\frac{\partial \tau_{yz}}{\partial y}+\frac{\partial \sigma_z}{\partial z}+f_z&=\rho a_z
\end{aligned} \tag{3.52}$$

Where,

f_x, f_y, f_z are the components of the body forces acting at point *M* of the material.

ρ is the density at point *M*.

a_x, a_y, a_z are the components of the acceleration vector at point *M*.

By integrating the equilibrium equations along the thickness of the laminate and assuming that both body forces and interlaminar stresses are negligible, the resultant force and moment equilibrium equations can be expressed as follows:

$$\begin{aligned}
\frac{\partial N_x}{\partial x}+\frac{\partial N_{xy}}{\partial y}&=\rho_s\frac{\partial^2 u_0}{\partial t^2}+R\frac{\partial^2 \theta_x}{\partial t^2}\\
\frac{\partial N_y}{\partial y}+\frac{\partial N_{xy}}{\partial x}&=\rho_s\frac{\partial^2 v_0}{\partial t^2}+R\frac{\partial^2 \theta_y}{\partial t^2}\\
\frac{\partial Q_x}{\partial x}+\frac{\partial Q_y}{\partial y}&=\rho_s\frac{\partial^2 w_0}{\partial t^2}\\
\frac{\partial M_x}{\partial x}+\frac{\partial M_{xy}}{\partial y}-Q_x&=R\frac{\partial^2 u_0}{\partial t^2}+I_{xy}\frac{\partial^2 \theta_x}{\partial t^2}\\
\frac{\partial M_y}{\partial y}+\frac{\partial M_{xy}}{\partial x}-Q_y&=R\frac{\partial^2 v_0}{\partial t^2}+I_{xy}\frac{\partial^2 \theta_y}{\partial t^2}
\end{aligned} \tag{3.53}$$

Where : $\left(\rho_s, R, I_{xy}\right)=\int_{-\frac{h}{2}}^{\frac{h}{2}}\left(1, z, z^2\right)\rho dz$

By substituting equation (3.49) into equations (3.53), the fundamental equations governing the behavior of laminated plates are obtained, which can be expressed as follows:

$$A_{11}\frac{\partial^2 u_0}{\partial x^2}+2A_{16}\frac{\partial^2 u_0}{\partial x\partial y}+A_{66}\frac{\partial^2 u_0}{\partial y^2}+A_{16}\frac{\partial^2 v_0}{\partial x^2}+\left(A_{12}+A_{66}\right)\frac{\partial^2 v_0}{\partial x\partial y}+A_{26}\frac{\partial^2 v_0}{\partial y^2}+$$
$$B_{11}\frac{\partial^2 \theta_x}{\partial x^2}+2B_{16}\frac{\partial^2 \theta_x}{\partial x\partial y}+B_{66}\frac{\partial^2 \theta_x}{\partial y^2}+B_{16}\frac{\partial^2 \theta_y}{\partial x^2}+\left(B_{12}+B_{66}\right)\frac{\partial^2 \theta_y}{\partial x\partial y}+B_{26}\frac{\partial^2 \theta_y}{\partial y^2}= \tag{3.54}$$
$$\rho_s\frac{\partial^2 u_0}{\partial t^2}+R\frac{\partial^2 \theta_x}{\partial t^2}$$

$$A_{16}\frac{\partial^2 u_0}{\partial x^2}+\left(A_{12}+A_{66}\right)\frac{\partial^2 u_0}{\partial x\partial y}+A_{26}\frac{\partial^2 u_0}{\partial y^2}+A_{66}\frac{\partial^2 v_0}{\partial x^2}+2A_{26}\frac{\partial^2 v_0}{\partial x\partial y}+A_{22}\frac{\partial^2 v_0}{\partial y^2}+$$
$$B_{16}\frac{\partial^2 \theta_x}{\partial x^2}+\left(B_{12}+B_{66}\right)\frac{\partial^2 \theta_y}{\partial x\partial y}+B_{26}\frac{\partial^2 \theta_x}{\partial y^2}+B_{66}\frac{\partial^2 \theta_y}{\partial x^2}+2B_{26}\frac{\partial^2 \theta_y}{\partial x\partial y}+B_{22}\frac{\partial^2 \theta_y}{\partial y^2}= \tag{3.55}$$
$$\rho_s\frac{\partial^2 v_0}{\partial t^2}+R\frac{\partial^2 \theta_y}{\partial t^2}$$

$$F_{55}\left(\frac{\partial \theta_x}{\partial x}+\frac{\partial^2 w_0}{\partial x^2}\right)+F_{45}\left(\frac{\partial \theta_x}{\partial x}+\frac{\partial \theta_y}{\partial x}+2\frac{\partial^2 w_0}{\partial x\partial y}\right)+F_{44}\left(\frac{\partial \theta_y}{\partial y}+\frac{\partial^2 w_0}{\partial y^2}\right)=\rho_s\frac{\partial^2 w_0}{\partial t^2} \tag{3.56}$$

$$B_{11}\frac{\partial^2 u_0}{\partial x^2}+2B_{16}\frac{\partial^2 u_0}{\partial x\partial y}+B_{16}\frac{\partial^2 v_0}{\partial x^2}+\left(B_{12}+B_{66}\right)\frac{\partial^2 v_0}{\partial x\partial y}+B_{26}\frac{\partial^2 v_0}{\partial y^2}+$$
$$D_{11}\frac{\partial^2 \theta_x}{\partial x^2}+2D_{16}\frac{\partial^2 \theta_x}{\partial x\partial y}+D_{66}\frac{\partial^2 \theta_x}{\partial y^2}+D_{16}\frac{\partial^2 \theta_y}{\partial x^2}+\left(D_{12}+D_{66}\right)\frac{\partial^2 \theta_y}{\partial x\partial y}+ \tag{3.57}$$
$$D_{26}\frac{\partial^2 \theta_y}{\partial y^2}-F_{55}\left(\theta_x+\frac{\partial w_0}{\partial x}\right)-F_{45}\left(\theta_y+\frac{\partial w_0}{\partial y}\right)=R\frac{\partial^2 u_0}{\partial t^2}+I_{xy}\frac{\partial^2 \theta_x}{\partial t^2}$$

$$B_{16}\frac{\partial^2 u_0}{\partial x^2}+\left(B_{16}+B_{66}\right)\frac{\partial^2 u_0}{\partial x\partial y}+B_{26}\frac{\partial^2 u_0}{\partial y^2}+B_{66}\frac{\partial^2 v_0}{\partial x^2}+2B_{26}\frac{\partial^2 v_0}{\partial x\partial y}+B_{22}\frac{\partial^2 v_0}{\partial y^2}+$$
$$D_{16}\frac{\partial^2 \theta_x}{\partial x^2}+\left(D_{12}+D_{66}\right)\frac{\partial^2 \theta_x}{\partial x\partial y}+D_{26}\frac{\partial^2 \theta_x}{\partial y^2}+D_{66}\frac{\partial^2 \theta_y}{\partial x^2}+2D_{26}\frac{\partial^2 \theta_y}{\partial x\partial y}+D_{22}\frac{\partial^2 \theta_y}{\partial y^2}- \tag{3.58}$$
$$F_{45}\left(\theta_x+\frac{\partial w_0}{\partial x}\right)-F_{44}\left(\theta_y+\frac{\partial w_0}{\partial y}\right)=R\frac{\partial^2 v_0}{\partial t^2}+I_{xy}\frac{\partial^2 \theta_y}{\partial t^2}$$

Equations (3.54 to 3.58) theoretically provide a framework for determining the five solution functions $\left(u_0(x,y,t), v_0(x,y,t), w_0(x,y,t), \theta_x(x,y,t), \theta_y(x,y,t)\right)$, which describe the mechanical response of laminated plates under given loading and boundary conditions.

In the analysis of vibrational behavior, where the objective is to determine the natural frequencies of vibration, the displacement field for harmonic motion can be expressed as follows:

$$
\begin{aligned}
u_0(x,y,t) &= u_0(x,y)e^{i\omega t} \\
v_0(x,y,t) &= v_0(x,y)e^{i\omega t} \\
w_0(x,y,t) &= w_0(x,y)e^{i\omega t} \\
\theta_x(x,y,t) &= \theta_x(x,y)e^{i\omega t} \\
\theta_y(x,y,t) &= \theta_y(x,y)e^{i\omega t}
\end{aligned}
\tag{3.59}
$$

Given that ω represents the natural vibration frequency of the plate, the natural frequencies can be determined by substituting the assumed displacement expressions into the fundamental equations (3.54 to 3.58).

However, the analytical solution of these equations is highly complex and generally feasible only for simplified configurations, such as orthotropic or symmetric laminates. In general, the mechanical behavior of laminated plates (particularly their vibrational characteristics) requires numerical methods for accurate analysis. Among these approaches, the Finite Element Method (FEM) is widely recognized as a powerful and standard tool for analyzing the vibrational response of complex structures.

3.9 Conclusion

This chapter has established the theoretical foundation for analyzing FG-CNTRC plates. The geometric definitions and mechanical characterizations were provided, with material properties evaluated using the extended rule of mixtures. The first-order shear deformation theory (FSDT) was applied to formulate the displacement and strain fields, leading to the derivation of stress, moment, and shear resultants. The fundamental equations for laminated plates were then derived, providing a comprehensive framework for their mechanical behavior. Additionally, the finite element method (FEM) was introduced as a robust numerical technique for solving these equations, which will be investigated in detail in the next chapter.

CHAPTER 4: FINITE ELEMENT METHOD FORMULATION FOR PLATES

4.1 Introduction

The accurate prediction of the mechanical behavior of composite plates, particularly those reinforced with carbon nanotubes and exposed to hygrothermal environments, requires robust numerical tools. Among these tools, the finite element method (FEM) stands out as one of the most powerful and widely used techniques in engineering and applied sciences. It allows the analysis of complex structures by discretizing the domain into smaller elements, enabling the solution of governing differential equations in an approximate yet highly effective manner.

This chapter presents the finite element formulation used to model the free vibration behavior of FG-CNTRC. It begins with a general overview of FEM principles, including the selection of appropriate elements, the discretization process, and the derivation of element matrices. It then develops the equations of motion using Lagrange's principle, considering hygrothermal effects. Finally, it introduces the modal analysis technique used to compute the natural frequencies and mode shapes of the plates, providing essential insight into their vibrational characteristics under environmental influences.

4.2 Finite Element Method

The finite element method is a numerical technique that divides a complex problem into smaller and more manageable elements. Each element is modeled by a set of equations that approximate the system's behavior locally. These equations are then assembled to form the global solution of the problem.

The analysis of the vibrational behavior of nanocomposite plates using FEM involves developing the equations of motion based on energy-based formulations and subsequently determining the natural frequencies of vibration.

The finite element structural analysis typically consists of four main steps [102]:

- **Selection of element:** this step involves selecting appropriate element types (e.g., triangles, quadrilaterals, etc.) and defining the interpolation (or shape) functions that approximate the displacement field within each element.
- **Discretization and calculation of element properties:** The problem is divided into smaller and more manageable elements. Then, derive the element-level matrices (such as the stiffness and mass matrices) are formulated to characterize the element's behavior.
- **Transformation to a global reference frame:** Since the element matrices are typically derived in a local (element-based) coordinate system, they must be transformed into a common global coordinate system so that they can be consistently assembled for the entire structure.
- **Assembly and solution:** The transformed element matrices are assembled into a global matrix that represents the entire structure. Boundary conditions are applied during this assembly process. Finally, you solve the resulting system of simultaneous algebraic equations (often as an eigenvalue problem for vibration analysis or as a linear system for static or dynamic analysis).

4.3 Reference Element Selection

This analysis requires the use of two-dimensional elements for discretization. Before proceeding, it is beneficial to compare these elements to make a better choice. Several tests have been conducted on different element types regarding convergence behavior, and the following observations were made:

- Quadrilateral elements generally outperform triangular elements in terms of convergence.
- Quadratic elements achieve higher accuracy compared to linear elements for a given number of degrees of freedom.
- Mindlin-based elements are best suited for thick plate analyses due to their ability to account for transverse shear deformation [103].
- Serendipity elements exhibit shear locking regardless of integration order. Lagrangian elements, on the other hand, are known to be less susceptible to locking, even with full integration for thin plates [103], [104].

Based on these considerations, 9-node quadratic Lagrangian elements (Figure 4.1) offered a well-suited balance for our analysis. This choice minimizes the risk of locking while maintaining good accuracy for the specific case of a thin plate.

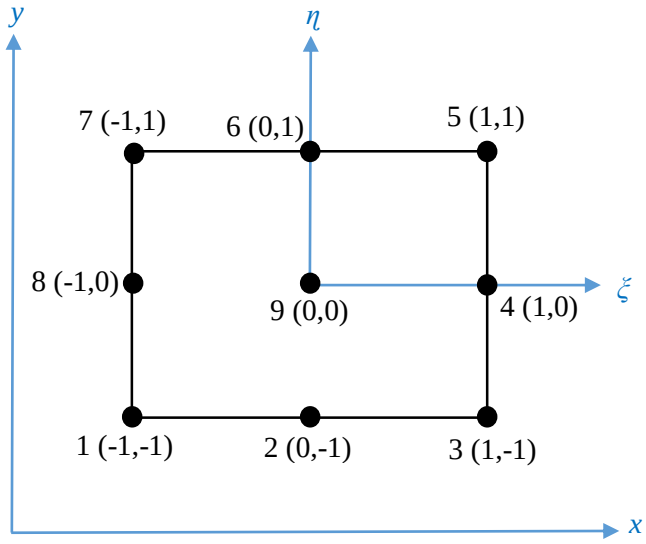

Figure 4.1 : Reference element

4.4 Discretization and calculation of element properties

The interpolation polynomial used for the selected nine-node element is based on Pascal's triangle, and is given as follows:

$$\{P\} = \{1 \quad \xi \quad \eta \quad \xi\eta \quad \xi^2 \quad \eta^2 \quad \xi^2\eta \quad \xi\eta^2 \quad \xi^2\eta^2\} \tag{4.1}$$

By substituting the coordinates of the nine nodes into the interpolation polynomial, the interpolation matrix can be obtained.

$$[A] = \begin{bmatrix} 1 & -1 & -1 & 1 & 1 & 1 & -1 & -1 & 1 \\ 1 & 0 & -1 & 0 & 0 & 1 & 0 & 0 & 0 \\ 1 & 1 & -1 & 1 & -1 & 1 & -1 & 1 & 1 \\ 1 & 1 & 0 & 1 & 0 & 0 & 0 & 0 & 0 \\ 1 & 1 & 1 & 1 & 1 & 1 & 1 & 1 & 1 \\ 1 & 0 & 1 & 0 & 0 & 1 & 0 & 0 & 0 \\ 1 & -1 & 1 & 1 & -1 & 1 & 1 & -1 & 1 \\ 1 & -1 & 0 & 1 & 0 & 0 & 0 & 0 & 0 \\ 1 & 0 & 0 & 0 & 0 & 0 & 0 & 0 & 0 \end{bmatrix} \tag{4.2}$$

Rewriting Eq. (4.2) in a matrix form:

$$[A] = [N_i]\{P\}, \ (i = 1,2,3,....,9) \tag{4.3}$$

Where, $[N_i]$ is the interpolation matrix.

For the vertex nodes, where, $\xi_i = \pm 1$ and $\eta_i = \pm 1$

$$N_i = \frac{1}{4}(1+\xi\xi_i)(1+\eta\eta_i)\xi\eta$$

For the interface nodes:

$$N_i = \frac{1}{2}(1-\xi^2)(1+\eta\eta_i)\eta\eta_i \quad \text{when, } \xi_i = 0 \text{ and } \eta_i = \pm 1$$

$$N_i = \frac{1}{2}(1-\eta^2)(1+\xi\xi_i)\xi\xi_i \quad \text{when, } \xi_i = \pm 1 \text{ and } \eta_i = 0$$

For the center node:

$$N_i = (1-\xi^2)(1-\eta^2)$$

4.4.1 Element displacement

Each node of the nine-node isoparametric quadrilateral element possesses five independent degrees of freedom: three displacements (u, v, w) and two rotations (θ_x, θ_y).

Where, $u_0 = \sum_{i=1}^{N_N} N_i u_{0i}$, $v_0 = \sum_{i=1}^{N_N} N_i v_{0i}$, $w_0 = \sum_{i=1}^{N_N} N_i w_{0i}$

$$\theta_x = \sum_{i=1}^{N_N} N_i \theta_{xi} \quad , \quad \theta_y = \sum_{i=1}^{N_N} N_i \theta_{yi} \tag{4.4}$$

Where, N_N is the number of nodes in the element.

The expressions in Eq. (4.4) can be rearranged in a matrix form as:

$$\begin{Bmatrix} u_0 \\ v_0 \\ w_0 \\ \theta_x \\ \theta_y \end{Bmatrix} = \sum_{i=1}^{N_N} \begin{bmatrix} N_i & 0 & 0 & 0 & 0 \\ 0 & N_i & 0 & 0 & 0 \\ 0 & 0 & N_i & 0 & 0 \\ 0 & 0 & 0 & N_i & 0 \\ 0 & 0 & 0 & 0 & N_i \end{bmatrix} \begin{Bmatrix} u_{0i} \\ v_{0i} \\ w_{0i} \\ \theta_{xi} \\ \theta_{yi} \end{Bmatrix} \tag{4.5}$$

Or in a compact form as:

$$\{\delta\} = [N]\{\delta_e\} \tag{4.6}$$

4.4.2 Element strain-displacement relationship

Considering the strain field given in Eq. (3.18) given in chapter 3 and the element displacement field defined in Eq. (4.4), the corresponding elemental strain-displacement relation can be expressed as follows:

$$\varepsilon_{x0}=\sum_{i=1}^{N_N}\frac{\partial N_i}{\partial x}u_{0i}\quad,\quad \varepsilon_{y0}=\sum_{i=1}^{N_N}\frac{\partial N_i}{\partial y}v_{0i}\quad,\quad \gamma_{xy0}=\sum_{i=1}^{N_N}\frac{\partial N_i}{\partial y}u_{0i}+\sum_{i=1}^{N_N}\frac{\partial N_i}{\partial x}v_{0i}$$

$$\kappa_x=\sum_{i=1}^{N_N}\frac{\partial N_i}{\partial x}\theta_{xi}\quad,\quad \kappa_y=\sum_{i=1}^{N_N}\frac{\partial N_i}{\partial y}\theta_{yi}\quad,\quad \kappa_{xy}=\sum_{i=1}^{N_N}\frac{\partial N_i}{\partial y}\theta_{xi}+\sum_{i=1}^{N_N}\frac{\partial N_i}{\partial x}\theta_{yi} \tag{4.7}$$

$$\gamma_{xz}=\sum_{i=1}^{N_N}N_i\theta_{xi}+\sum_{i=1}^{N_N}\frac{\partial N_i}{\partial x}w_{yi}\quad,\quad \gamma_{yz}=\sum_{i=1}^{N_N}N_i\theta_{yi}+\sum_{i=1}^{N_N}\frac{\partial N_i}{\partial y}w_{0i}$$

The compact form of Eq. (4.7) can be given as follows:

$$\begin{Bmatrix}\varepsilon_{x0}\\ \varepsilon_{y0}\\ \gamma_{xy0}\\ \kappa_x\\ \kappa_y\\ \kappa_{xy}\\ \gamma_{xz}\\ \gamma_{yz}\end{Bmatrix}=\sum_{i=1}^{N_N}\begin{bmatrix}\partial N_i/\partial x & 0 & 0 & 0 & 0\\ 0 & \partial N_i/\partial y & 0 & 0 & 0\\ \partial N_i/\partial y & \partial N_i/\partial x & 0 & 0 & 0\\ 0 & 0 & 0 & \partial N_i/\partial x & 0\\ 0 & 0 & 0 & 0 & \partial N_i/\partial y\\ 0 & 0 & 0 & \partial N_i/\partial y & \partial N_i/\partial x\\ 0 & 0 & \partial N_i/\partial x & N_i & 0\\ 0 & 0 & \partial N_i/\partial y & 0 & N_i\end{bmatrix}\begin{Bmatrix}u_{0i}\\ v_{0i}\\ w_{0i}\\ \theta_{xi}\\ \theta_{yi}\end{Bmatrix} \tag{4.8}$$

$$\begin{Bmatrix}\varepsilon_0\\ \kappa\\ \gamma\end{Bmatrix}=\sum_{i=1}^{N_N}[B_i]\{\delta_e\} \tag{4.9}$$

$$\{\varepsilon\}=[B]\{\delta_e\} \tag{4.10}$$

Where, ε_0, κ, and γ are membrane strains, bending strains, and transverse shear strains, respectively.

$[B_i]$ represents the strain interpolation matrix. The elements of the matrix $[B_i]$ are defined as:

$$\begin{Bmatrix} \frac{\partial N_i}{\partial x} \\ \frac{\partial N_i}{\partial y} \end{Bmatrix} = [J]^{-1} \begin{Bmatrix} \frac{\partial N_i}{\partial \xi} \\ \frac{\partial N_i}{\partial \eta} \end{Bmatrix} \tag{4.11}$$

The Jacobian matrix $[J]$ enables the conversion from the Cartesian coordinate system to the coordinate system associated with the element.

$$[J] = \begin{bmatrix} \frac{\partial x}{\partial \xi} & \frac{\partial y}{\partial \xi} \\ \frac{\partial x}{\partial \eta} & \frac{\partial y}{\partial \eta} \end{bmatrix} \tag{4.12}$$

Where, $\frac{\partial x}{\partial \xi} = \sum_{i=1}^{N_N} \frac{\partial N_i(\xi,\eta)}{\partial \xi} x_i$; $\frac{\partial y}{\partial \xi} = \sum_{i=1}^{N_N} \frac{\partial N_i(\xi,\eta)}{\partial \xi} y_i$; $\frac{\partial x}{\partial \eta} = \sum_{i=1}^{N_N} \frac{\partial N_i(\xi,\eta)}{\partial \eta} x_i$

$\frac{\partial y}{\partial \eta} = \sum_{i=1}^{N_N} \frac{\partial N_i(\xi,\eta)}{\partial \eta} y_i$

The nonlinear strain of the plate can be expressed as [101]:

$$\varepsilon_{nl} = \begin{Bmatrix} \varepsilon_{xnl} \\ \varepsilon_{ynl} \\ \gamma_{xynl} \\ \gamma_{xznl} \\ \gamma_{yznl} \end{Bmatrix} = \begin{Bmatrix} \frac{1}{2}\{u_{,x}^2 + v_{,x}^2 + w_{,x}^2\} \\ \frac{1}{2}\{u_{,y}^2 + v_{,y}^2 + w_{,y}^2\} \\ u_{,x}u_{,y} + v_{,x}v_{,y} + w_{,x}w_{,y} \\ u_{,x}u_{,z} + v_{,x}v_{,z} \\ u_{,y}u_{,z} + v_{,y}v_{,z} \end{Bmatrix} \tag{4.13}$$

Since : $u = u_0 + z\theta_y$ and $v = v_0 + z\theta_x$, Eq. (4.13) may be written as:

$$\begin{aligned}
\varepsilon_{xnl} &= [u_{0,x}^2 + v_{0,x}^2 + w_{,x}^2 + 2z(u_{0,x}\theta_{y,x} - v_{0,x}\theta_{x,x}) + z^2(\theta_{y,x}^2 + \theta_{x,x}^2)]/2 \\
\varepsilon_{ynl} &= [u_{0,y}^2 + v_{0,y}^2 + w_{,y}^2 + 2z(u_{0,y}\theta_{y,y} - v_{0,y}\theta_{x,y}) + z^2(\theta_{x,y}^2 + \theta_{y,y}^2)]/2 \\
\gamma_{xynl} &= [u_{0,x}u_{0,y} + v_{0,x}v_{0,y} + w_{,x}w_{,y} + z(u_{0,y}\theta_{y,x} + u_{0,x}\theta_{y,y} - z(v_{0,y}\theta_{x,x} + v_{0,x}\theta_{x,y}) + z^2(\theta_{y,x}\theta_{y,y} + \theta_{x,x}\theta_{x,y})] \\
\gamma_{xznl} &= [u_{0,x}\theta_y - v_{0,x}\theta_x + z(\theta_y\theta_{y,x} + \theta_x\theta_{x,x})] \\
\gamma_{yznl} &= [u_{0,y}\theta_y - v_{0,y}\theta_x + z(\theta_y\theta_{y,y} + \theta_x\theta_{x,y})]
\end{aligned} \tag{4.14}$$

The matrix form of the Equation (4.14) is:

$$\begin{aligned}\{\varepsilon_{nl}\} &= \{\varepsilon_{xnl}, \varepsilon_{ynl}, \gamma_{xynl}, \gamma_{xznl}, \gamma_{yznl}\}^T \\ \{\varepsilon_{nl}\} &= [R]\{d\}/2\end{aligned} \tag{4.15}$$

Where, $[R]$ is the multiplier matrix obtained following the procedure given in [105]

$$\{d\} = \{u_{0,x}, u_{0,y}, v_{0,x}, v_{0,y}, w_{0,x}, w_{0,y}, \theta_{x,x}, \theta_{x,y}, \theta_{y,x}, \theta_{y,y}, \theta_x, \theta_y\}^T \tag{4.16}$$

Using Equation (4.16), $\{d\}$ may be expressed as:

$$\{d\} = [G]\{\delta_e\} \tag{4.17}$$

Where, [G] represents the shape function operating matrix.

$$[G] = \sum_{i=1}^{9} \begin{bmatrix} N_{i,x} & 0 & 0 & 0 & 0 \\ N_{i,y} & 0 & 0 & 0 & 0 \\ 0 & N_{i,x} & 0 & 0 & 0 \\ 0 & N_{i,y} & 0 & 0 & 0 \\ 0 & 0 & N_{i,x} & 0 & 0 \\ 0 & 0 & N_{i,y} & 0 & 0 \\ 0 & 0 & 0 & N_{i,x} & 0 \\ 0 & 0 & 0 & N_{i,y} & 0 \\ 0 & 0 & 0 & 0 & N_{i,x} \\ 0 & 0 & 0 & 0 & N_{i,y} \\ 0 & 0 & 0 & 1 & 0 \\ 0 & 0 & 0 & 0 & 1 \end{bmatrix} \tag{4.18}$$

4.4.3 Element load vector

The element load vector due to external transverse static load *q* per unit area is given by:

$$\{X_e\} = \iint N_i \begin{bmatrix} q \\ 0 \\ 0 \end{bmatrix} dxdy \tag{4.19}$$

The element load vector due to hygrothermal forces and moments is given by:

$$\{X_e^H\} = \iint [B]^T \{F^H\} dxdy \tag{4.20}$$

Where,

$$\{F^H\} = \{N_x^H, N_y^H, N_{xy}^H, M_x^H, M_y^H, M_{xy}^H, 0, 0\}^T \tag{4.21}$$

4.5 Motion equations

The vibrational analysis of such a structure assumes the absence of external forces, simplifying the problem to a free vibration study.

The equations of motion for laminated plates are typically derived using Lagrange's equation, which provides a systematic approach to incorporating kinetic and potential energy contributions, ensuring an accurate representation of the system's behavior.

$$\frac{\partial}{\partial t}\left(\frac{\partial L}{\partial \dot{\delta}_r}\right)-\frac{\partial L}{\partial \delta_r}+\frac{\partial P}{\partial \dot{\delta}_r}=0 \qquad r=1,2,...,R \tag{4.22}$$

Where,

- R: Total number of degrees of freedom of the structure.
- L: Total kinetic energy of the plate.
- P: Total potential energy of the plate.

4.5.1 Potential energy

The expression for the elemental potential energy π_e in the presence of hygrothermal stresses and the absence of external force work is:

$$P_e = P_{elastic} + P_{\sigma_e} \tag{4.23}$$

$$P_{elastic} = \frac{1}{2}\iint \{\varepsilon\}^T \{\sigma\}\, dxdy = \frac{1}{2}\iint \{\varepsilon\}^T [C]\{\varepsilon\}\, dxdy \tag{4.24}$$

Substituting Equation (4.10) into Equation (4.24):

$$P_{elastic} = \frac{1}{2}\iint \{\delta_e\}^T [B]^T [C][B]\{\delta_e\}\, dxdy \tag{4.25}$$

Which gives the element elastic stiffness matrix $[K_e]$:

$$[K_e] = \iint [B]^T [C][B]\, dxdy \tag{4.26}$$

Thus, the elastic strain energy is:

$$P_{elastic} = \frac{1}{2}\{\delta_e\}^T [K_e]\{\delta_e\} \tag{4.27}$$

The potential energy contribution due to the initial stress field is:

$$P_{\sigma_e} = \frac{1}{2}\iint \{d\}^T [S]\{d\}\, dxdy \tag{4.28}$$

Where, [S] is a matrix contains in-plane initial internal force, moment resultants, and transverse shear resultant terms.

$$[S] = \begin{bmatrix}
S_{11} & & & & & & & & & & & \\
S_{21} & S_{22} & & & & & & & & & & \\
0 & 0 & S_{33} & & & & & & & & & \\
0 & 0 & S_{43} & S_{44} & & & & & & & & \\
0 & 0 & 0 & 0 & S_{55} & & & & sym & & & \\
0 & 0 & 0 & 0 & S_{65} & S_{66} & & & & & & \\
0 & 0 & S_{73} & S_{74} & 0 & 0 & S_{77} & & & & & \\
0 & 0 & S_{83} & S_{84} & 0 & 0 & S_{87} & S_{88} & & & & \\
S_{91} & S_{92} & 0 & 0 & 0 & 0 & 0 & 0 & S_{99} & & & \\
S_{101} & S_{102} & 0 & 0 & 0 & 0 & 0 & 0 & S_{109} & S_{1010} & & \\
0 & 0 & S_{113} & S_{114} & 0 & 0 & 0 & 0 & 0 & 0 & 0 & \\
S_{121} & S_{122} & 0 & 0 & 0 & 0 & 0 & 0 & 0 & 0 & 0 & 0
\end{bmatrix} \tag{4.29}$$

$S_{11} = S_{33} = S_{55} = N_x^i$; $S_{22} = S_{44} = S_{66} = N_y^i$; $S_{12} = S_{43} = S_{65} = N_{xy}^i$;

$S_{77} = S_{99} = N_x^i h^2/12$; $S_{88} = S_{1010} = N_y^i h^2/12$; $S_{87} = S_{109} = N_{xy}^i h^2/12$;

$-S_{73} = S_{91} = M_x^i$; $-S_{74} = -S_{83} = S_{92} = S_{101} = M_{xy}^i$; $-S_{84} = S_{102} = M_y^i$;

$-S_{113} = S_{121} = Q_x^i$; $-S_{114} = S_{122} = Q_y^i$.

With N_x^i, N_y^i, N_{xy}^i are the in-plane initial internal force resultants, M_x^i, M_y^i, M_{xy}^i are the initial internal moment resultants, and Q_x^i, Q_y^i are the initial transverse shear resultants.

Substituting Equation (4.17) into Equation (4.28):

$$P_{elastic} = \frac{1}{2}\iint \{\delta_e\}^T [G]^T [S][G]\{\delta_e\}\, dxdy \tag{4.30}$$

Which gives the element initial stress stiffness matrix $[K_{\sigma_e}]$:

$$[K_{\sigma_e}] = \iint [G]^T [S][G]\, dxdy \tag{4.31}$$

Thus, the elastic strain energy is:

$$P_{\sigma_e} = \frac{1}{2}\{\delta_e\}^T \left[K_{\sigma_e}\right]\{\delta_e\} \tag{4.32}$$

By substituting Equations (4.27 and 4.32) into Equation (4.23), we obtained:

$$P_e = \frac{1}{2}\{\delta_e\}^T [K_e]\{\delta_e\} + \frac{1}{2}\{\delta_e\}^T \left[K_{\sigma_e}\right]\{\delta_e\} \tag{4.33}$$

$$P_e = \frac{1}{2}\{\delta_e\}^T \left([K_e] + \left[K_{\sigma_e}\right]\right)\{\delta_e\} \tag{4.34}$$

In the case of a discretized plate, the total potential energy is the sum of all the elemental potential energies:

$$P = \sum_{e=1}^{NE} P_e \tag{4.35}$$

NE: Number of elements.

4.5.2 Kinetic energy

The elemental kinetic energy L_e is given by the following expression:

$$L_e = \frac{1}{2}\int_V \left\{\dot{\Delta}\right\}^T \rho\left\{\dot{\Delta}\right\} dV \tag{4.36}$$

- $\dot{\Delta}$: The velocity vector of a point M(x, y, z) in the laminate, $\left\{\dot{\Delta}\right\}^T = \{\dot{u}, \dot{v}, \dot{w}\}$.
- V: The volume of the plate.

Substituting $\left\{\dot{\Delta}\right\} = [N]\left\{\dot{\delta}_e\right\}$ into Equation (4.36).

$$L_e = \frac{1}{2}\int_V [N]^T \left\{\dot{\delta}_e\right\}^T \rho[N]\left\{\dot{\delta}_e\right\} dV \tag{4.37}$$

Integrating Eq. (4.37) through the thickness of the plate leads to:

$$L_e = \frac{1}{2}\iint \left(\int_h [N]^T \left\{\dot{\delta}_e\right\}^T \rho[N]\left\{\dot{\delta}_e\right\} dz\right) dxdy \tag{4.38}$$

$$L_e = \frac{1}{2}\iint [N]^T \left\{\dot{\delta}_e\right\}^T [\bar{m}][N]\left\{\dot{\delta}_e\right\} dxdy \tag{4.39}$$

Where $[\bar{m}]$ is the inertia matrix, expressed as:

$$[\bar{m}] = \begin{bmatrix} I_0 & 0 & 0 & I_1 & 0 \\ 0 & I_0 & 0 & 0 & I_1 \\ 0 & 0 & I_0 & 0 & 0 \\ I_1 & 0 & 0 & I_2 & 0 \\ 0 & I_1 & 0 & 0 & I_2 \end{bmatrix} \tag{4.40}$$

Note that, $I_i = \sum_{k=1}^{N_L} \int_{z_{k-1}}^{z_k} Z^i \rho^k dz$, $(i = 0,1,2)$ and ρ^k is the material density of the k^{th} layer.

The Eq. (4.39) can be rewritten as:

$$L_e = \frac{1}{2}\left\{\dot{\delta}_e\right\}^T \left(\iint [N]^T [\bar{m}][N] dxdy\right)\left\{\dot{\delta}_e\right\} \tag{4.41}$$

$$L_e = \frac{1}{2}\left\{\dot{\delta}\right\}_e^T [M_e]\left\{\dot{\delta}_e\right\} \tag{4.42}$$

Where, $[M_e]$ is the element mass matrix, given by:

$$[M_e] = \iint [N]^T [\bar{m}][N] dxdy \tag{4.43}$$

The total kinetic energy of the plate is the sum of all the elemental kinetic energies:

$$L = \sum_{e=1}^{NE} L_e \tag{4.44}$$

By substituting Eqs. (4.34) and (4.42) into Eq. (4.22), the Lagrange equation for a single element of the plate becomes:

$$[M_e]\left\{\ddot{\delta}_e\right\} + \left([K_e] + \left[K_{\sigma_e}\right]\right)\{\delta_e\} = 0 \tag{4.45}$$

Here, $\left\{\ddot{\delta}_e\right\}$ is the vector of elemental accelerations.

The global equations of motion are obtained using Eqs. (3.35), (3.44):

$$[M]\left\{\ddot{\delta}\right\} + \left([K] + [K_\sigma]\right)\{\delta\} = 0 \tag{4.46}$$

Where $[M]$, $[K]$, and $[K_\sigma]$ are respectively global mass, global stiffness and global initial stress stiffness matrices.

4.6 Solution process

The initial step of the solution involves determining the stress resultants induced by the hygrothermal loading conditions. Eqs. (4.26), (4.43), (4.31), (4.19) and (4.20) provide respectively the formulations for the element stiffness matrix $[K_e]$, the mass matrix $[M_e]$, the initial stress stiffness matrix due to hygrothermal load $\left[K_{\sigma_e}\right]$, and the element load vectors $\{X_e\}$, and $\left\{X_e^H\right\}$ to evaluate them in the local natural coordinates of the element, followed by numerical integration using Gaussian quadrature. Then the element matrices are assembled to obtain the respective global matrices.

The initial displacements $\left\{\delta^i\right\}$ are found using the equilibrium condition:

$$[K]\left\{\delta^i\right\} = \left\{X\right\} + \left\{X^H\right\} \tag{4.47}$$

Where $\{P\}$ is the global load vector due to external transverse static load, and $\left\{X^H\right\}$ is the global load vector due to hygrothermal forces and moments.

After that, the initial stress resultants (N_x^i, N_y^i, N_{xy}^i M_x^i, M_y^i, M_{xy}^i, Q_x^i and Q_y^i) are obtained from Eqs. (3.55), (4.10).

The next part of the solution involves the determination of natural frequencies from the eigenvalue solution of the Eq. (4.46).

4.6.1 Modal analysis

Modal analysis is used to determine the natural frequencies and mode shapes of a structure. It helps analyze the system's dynamic behavior by solving the eigenvalue problem associated with the equation of motion.

For free vibration, we assume a harmonic solution:

$$\{\delta\}(t) = \{\Phi\} e^{i\omega t} \tag{4.48}$$

Where:

- ω is the natural frequency,
- $\{\Phi\}$ is the mode shape (eigenvector).

By substituting into the equation of motion and simplifying, we obtain the eigenvalue problem:

$$\left(\left([K]+[K_\sigma]\right)-\omega^2[M]\right)\{\Phi\}=\{0\} \tag{4.49}$$

This equation must be solved for the eigenvalues ω^2 (squared natural frequencies) and the corresponding mode shapes $\{\Phi\}$.

Equation (4.49) defines a generalized eigenvalue problem, which can be solved using various numerical techniques such as the Householder method, QR method, and subspace iteration method.

The selection of a solution method depends on factors such as the properties of matrices [*K*] and [*M*], their dimensions, bandwidth, and the number of eigenvalues required.

Among these methods, the subspace iteration technique is widely employed in structural analysis software due to its efficiency in computing the smallest eigenvalues of large systems. This approach relies on inverse iterations performed simultaneously on a set of initial vectors. With successive iterations, the matrices [*K*] and [*M*] progressively transform toward a diagonal form, making the generalized Jacobi method particularly effective for solving the reduced eigenvalue problem.

4.7 Conclusion

This chapter presented the finite element method for structural analysis, detailing the selection of a reference element, discretization, and element property calculations. We established the strain-displacement relationships and derived the equations of motion using Lagrange's principle. The solution process was outlined, including modal analysis, which provides key insights into the structure's dynamic behavior. These foundations will be essential for analyzing the effects of hygrothermal environments on composite structures in the following chapters.

CHAPTER 5: VIBRATIONAL BEHAVIOR OF FG-CNTRC PLATES UNDER THE EFFECT OF VARIOUS THERMAL AND HYGROTHERMAL ENVIRONMENTS.

5.1 Introduction

This study examines the effects of various parameters on the vibrational performance of CNTRC plates to achieve enhanced structural efficiency. A finite element-based computational code was developed to evaluate the vibrational characteristics of nanocomposite plates, including their natural frequencies and mode shapes. The code demonstrates significant versatility, accommodating the analysis of both thin and thick plates composed of isotropic or laminated composite materials reinforced with functionally graded CNT plies.

To validate the accuracy of the developed code, three comparative studies were conducted. The first study compares the dimensionless natural frequencies obtained from the code against reference values reported in the literature at room temperature. The second study investigates the code's ability to predict vibrational responses under varying thermal conditions, while the third study assesses its reliability in moisture-affected environments. The excellent agreement between the results generated by the in-house code and those reported in the literature or obtained using ABAQUS underscores the code's accuracy and robustness in modeling free vibration responses under diverse environmental conditions, including thermal and hygrothermal effects.

Subsequently, a detailed parametric analysis was performed to explore the influence of key factors on the free vibration behavior of polymeric nanocomposite plates reinforced with carbon nanotube fillers. These factors include plate geometry (length-to-width and width-to-thickness ratios), carbon nanotube volume fractions, boundary conditions, linear and nonlinear CNT distribution patterns, and the effects of thermal and hygrothermal environments.

5.2 Mesh convergence study

In order to ensure the accuracy and reliability of the numerical results, a convergence study is conducted to determine the appropriate number of finite elements required to discretize the plate. This process involves systematically refining the mesh and analyzing the corresponding variations in the computed natural frequencies.

The objective is to identify a mesh density beyond which further refinement produces negligible changes in the solution, indicating that the numerical model has reached convergence. The selected mesh configuration will then be used for all subsequent simulations to achieve a balance between computational efficiency and solution accuracy.

Table 5.1 Mesh Convergence of the first five non-dimensional frequencies (SSSS, *a/b* =1, *b/h* =10)

Mesh Configuration (Elements)	**Mode number**				
	1	**2**	**3**	**4**	**5**
4 × 4	17.6626	22.2112	34.4528	52.0162	67.4844
6 × 6	17.6661	22.2721	34.2961	54.3257	67.2205
7 × 7	17.6665	22.2819	34.2739	54.0756	67.1956
10 × 10	17.6668	22.2892	34.2547	53.8176	67.1681
12 × 12	17.6669	22.2904	34.2518	53.7740	67.1636

The results in Table 5.1 indicate that as the mesh is refined from 4 × 4 to 12 × 12, the natural frequencies converge. Although the 6 × 6 mesh provides close values for lower modes, it shows a noticeable deviation (nearly 1%) in higher modes when compared to the 10 × 10 mesh. Since the difference between the 10 × 10 and 12 × 12 meshes is minimal, the 10 × 10 configuration is adopted as sufficiently accurate.

5.3 Comparative studies

The accuracy and reliability of the results obtained using the proposed mathematical formulations were assessed through a series of comparative studies. These studies involved benchmarking the computed results against reference data from the existing literature and included the following cases:

- FG-CNTRC plates at room temperature,
- FG-CNTRC plates under varying thermal conditions,
- CNTRC plates subjected to moisture-laden environments.

5.3.1. FG-CNTRC plates at room temperature

In this study, simply supported square FG-CNTRC plates with dimensions $a = b = 0.02$ m are considered. The analysis is conducted for two width-to-thickness ratios (b/h = 10, 50), various CNT volume fractions (V_{CNT}^{*} = 0.11, 0.14, 0.17), and different CNT distribution patterns (UD, FG-V, FG-O, and FG-X). The mechanical properties of the nanocomposite constituents are assumed as: $E_{11}^{CNT} = 5.6466\ TPa$, $E_{22}^{CNT} = 7.0800\ TPa$, $G_{12}^{CNT} = 1.9445\ TPa$, $\alpha_{11}^{CNT} = 3.4584\ (10^{-6}/\mathrm{K})$, $\alpha_{22}^{CNT} = 5.1682\ (10^{-6}/\mathrm{K})$. The properties of the PmPV (poly(m-phenylenevinylene)-co-(2.5-dioctoxy-p-phenylene)) matrix material are: $\rho^{m} = 1150 Kg/m^{3}$, $v^{m} = 0.34$ and $E^{m} = 2.1 GPa$. The corresponding efficiency parameters of $V_{CNT}^{*} = 0.11$ are: $\eta_1 = 0.149$, $\eta_2 = \eta_3 = 0.934$, for $V_{CNT}^{*} = 0.14$, $\eta_1 = 0.150$, $\eta_2 = \eta_3 = 0.941$ and for $V_{CNT}^{*} = 0.17$, $\eta_1 = 0.149$ and $\eta_2 = \eta_3 = 1.381$. [21], [88]

The fundamental non-dimensional natural frequency ($\bar{\omega} = \omega\ (b^2/h)\sqrt{\rho^m/E^m}$) of the FG-CNTRC plates are compared with those reported by Zhu et al. [21] and Singh et al. [106] in Table 5.2. It can be observed that the obtained results and those reported in Refs. [21] and [106] are in very good agreement, validating the accuracy and reliability of the findings presented in this study for FG-CNTRC plates.

Table 5.2 Comparison of the dimensionless fundamental natural frequency for SSSS square CNTRC plate in room temperature

		b/h=10					b/h=50				
		Present	Zhu et al. [21]		Singh and Bhar [106]		Present	Zhu et al. [21]		Singh and Bhar [106]	
Distribution patterns	V_{CNT}^{*}		result	error (%)	result	error (%)		result	error (%)	result	error (%)
UD	0.11	13,5048	13,532	0,20	13,735	1,70	19,1502	19,184	0,18	19,238	0,46
	0.14	14,292	14,306	0,10	14,553	1,83	21,3116	21,287	0,12	21,417	0,49
	0.17	16,7776	16,815	0,22	16,832	0,32	23,6016	23,697	0,40	23,077	2,22
FG-X	0.11	14,5783	14,616	0,26	14,873	2,02	22,8542	22,984	0,57	23	0,64
	0.14	15,3428	15,368	0,16	15,669	2,13	25,4578	25,555	0,38	25,631	0,68
	0.17	18,2216	18,278	0,31	18,377	0,85	28,2385	28,413	0,62	27,653	2,07
FG-O	0.11	11,5577	11,55	0,07	11,675	1,01	14,3191	14,302	0,12	14,326	0,05
	0.14	12,3612	12,338	0,19	12,501	1,13	15,8493	15,801	0,30	15,859	0,06
	0.17	14,2962	14,282	0,10	14,198	0,69	17,5704	17,544	0,15	17,136	2,47
FG-V	0.11	12,4341	12,452	0,14	12,606	1,38	16,2133	16,252	0,24	16,267	0,33
	0.14	13,252	13,256	0,03	13,451	1,50	17,9844	17,995	0,06	18,048	0,35
	0.17	15,4385	15,461	0,15	15,409	0,19	19,9349	19,982	0,24	19,488	2,24

5.3.2. FG-CNTRC under different temperature environments

The second validation study examines the effect of elevated temperatures on the free vibration response of simply-supported FG-CNTRC plates. This study aims to validate the accuracy of the present model by comparing its results with those reported by Kumar et al. [107] under similar thermal conditions (500K and 700K). The analysis is performed for two width-to-thickness ratios (*a/h* = 50, 100) , different CNT volume fractions (V^* = 0.11, 0.14, 0.17), and three distribution patterns of CNTs (UD, FG-O, and FG-X).

The matrix material properties are considered as temperature-dependence to accurately represent the thermal behavior. Where, the material properties of the matrix are : $\rho^m = 1150 Kg/m^3$, $v^m = 0.34$, $E^m = (3.51 - 0.0047T) GPa$, and $\alpha^m = 45(1 + 0.0005\Delta T) \times 10^{-6}/K$. Whereas, CNTs properties are specified for T=500K as: $E_{11}^{CNT} = 5.5308\ TPa$, $E_{22}^{CNT} = 6.9348\ TPa$, $G_{12}^{CNT} = 1.9643\ TPa$, and for T=700K, the CNT properties are: $E_{11}^{CNT} = 5.4744\ TPa$, $E_{22}^{CNT} = 6.8641\ TPa$, $G_{12}^{CNT} = 1.9644\ TPa$.

Table 5.3 Comparison of fundamental frequencies of CNTRC plates under different temperature environments

V*CNT		*a/h=50*						*a/h=100*					
		500k			700k			500k			700k		
		Present	L. Kumar et al. [107]		Present	L. Kumar et al. [107]		Present	L. Kumar et al. [107]		Present	L. Kumar et al. [107]	
			Result	Error (%)		Result	error (%)		Result	Error (%)		Result	Error (%)
0.11	UD	24,6052	24,6299	0,10	48,1124	48,3545	0,50	25.3133	25.3206	0,03	54.4251	54.4956	0,13
	FG-O	18,2363	18,1161	0,66	37,1502	36,542	1,64	18.5080	18.4203	0,47	39.7982	39.4688	0,83
	FG-X	29,3246	29,4382	0,39	54,9653	55,6105	1,17	30.5548	30.6233	0,22	64.9790	65.2798	0,46
0.14	UD	27,3908	27,4242	0,12	52,5112	52,8352	0,62	28.3497	28.3595	0,03	60.7024	60.7984	0,16
	FG-O	20,2844	20,1466	0,68	41,0524	40,3832	1,63	20.6508	20.5503	0,49	44.5687	44.1939	0,84
	FG-X	32,5943	32,6959	0,31	59,5017	60,0574	0,93	34.2477	34.3176	0,20	72.2036	72.4682	0,37
0.17	UD	30,3744	30,404	0,10	59,6405	59,9328	0,49	31.2234	31.2322	0,03	67.2905	67.3755	0,13
	FG-O	22,4473	22,3178	0,58	45,9909	45,4116	1,26	22.7679	22.6646	0,45	49.1622	48.8103	0,72
	FG-X	36,2752	36,3362	0,17	68,3433	68,5931	0,37	37.7427	37.8052	0,17	80.4456	80.5921	0,18

The fundamental non-dimensional frequencies of the FG-CNTRC plates are compared with the results reported by Kumar et al. [107] in Table 5.2. An excellent agreement is

observed between the present findings and those reported by Kumar et al. [107], confirming the accuracy and reliability of the developed model under elevated temperature conditions.

5.3.3. CNTRC exposed to a moisture-laden environment

The final comparison study focuses on the free vibration analysis of simply-supported UD-CNTRC plates within moisture environments. Since no published research could be found on the influence of moisture on the free vibration characteristics of such plates, the present study utilizes the commercial finite element analysis (FEA) software ABAQUS for comparison.

Table 5.4 compares the first five non-dimensional natural frequencies ($\bar{\omega} = \omega(b^2 / h)\sqrt{\rho^m / E^m}$) obtained via the in-house code with those calculated using ABAQUS for two different moisture concentrations (0% and 4%). The analysis is conducted with fixed geometric and material parameters: a width-to-thickness ratio of 10, a length-to-width ratio of 1, and a CNT volume fraction of 0.17.

The excellent agreement observed between the results obtained from both methods, as presented in Table 5.4, confirms the accuracy and capability of the in-house code for predicting the free vibration behavior of UD-CNTRC plates under hygrothermal conditions.

Table 5.4 Comparative examination of the first five dimensionless frequencies with those obtained by ABAQUS. (a/b = 1, b/h = 50, $V_{CNT}^{*} = 0.17$)

Mode number	Moisture concentration (0%)			Moisture concentration (4%)		
	ABAQUS	present	error (%)	ABAQUS	present	error (%)
1	21.142	21.060	0.39	18.066	17.975	0.51
2	27.512	27.321	0.70	24.899	24.692	0.84
3	44.326	43.164	2.69	42.417	41.216	2.91
4	72.669	68.886	5.49	71.215	67.392	5.67
5	77.924	76.680	1.62	74.857	73.575	1.74

The comparative studies presented in Tables 5.2-5.4 demonstrate an excellent correlation between the results obtained from the in-house developed code and those reported in the literature (for thermal effects) or from the commercial FEA software ABAQUS (for moisture effects). These observations strongly accuracy, robustness, and reliability of the proposed computational model in predicting the free vibration behavior of FG-CNTRC plates under diverse environmental conditions, including elevated temperatures and moisture exposure.

5.4 Free vibrations analysis of FG-CNTRC plates under thermal environments

This section presents a comprehensive parametric investigation to elucidate the effect of temperature on a broad range of parameters, which include *(i)* width-to-thickness ratio, *(ii)* length-to-width ratio, *(iii)* CNTs volume fraction, *(iv)* boundary conditions, and *(vi)* thermal environments, on the free vibration characteristics of FG-CNTRC plates.

The FG nanocomposite plates are composed of polymethyl methacrylate (PMMA) polymer matrix reinforced with armchair (10, 10) single-walled carbon nanotubes. The material properties of the PMMA matrix are considered temperature-dependent and are defined as follows:

$$\nu^m = 0.34, \quad \rho^m = 1150\,\text{kg/m}^3 \tag{5.1}$$

$$E^m = (3.52 - 0.0034T)\,\text{GPa} \tag{5.2}$$

$$\alpha^m = 45(1 + 0.0005\Delta T)\times 10^{-6}/K \tag{5.3}$$

The temperature-dependent material properties of CNTs are expressed as follows [52, 57]:

$$E_{11}^{CNT}(TPa) = 6.3998 - 4.33817\times 10^{-3}T + 7.43\times 10^{-6}T^2 - 4.45833\times 10^{-9}T^3 \tag{5.4}$$

$$E_{22}^{CNT}(TPa) = 8.02155 - 5.420375\times 10^{-3}T + 9.725\times 10^{-6}T^2 - 5.5625\times 10^{-9}T^3 \tag{5.5}$$

$$G_{22}^{CNT}(TPa) = 1.40755 - 3.476208\times 10^{-3}T + 6.965\times 10^{-6}T^2 - 4.479167\times 10^{-9}T^3 \tag{5.6}$$

$$\alpha_{11}^{CNT}(10^{-6}/K) = -1.12515 + 0.02291688T - 2.887\times 10^{-5}T^2 + 1.13625\times 10^{-8}T^3 \tag{5.7}$$

$$\alpha_{22}^{CNT}(10^{-6}/K) = 5.43715 - 0.984625\times 10^{-4}T - 2.9\times 10^{-7}T^2 - 1.25\times 10^{-11}T^3 \tag{5.8}$$

Where, T refers to temperature.

To investigate the impact of temperature variations on CNT-reinforced composite structures, this study explores the response of plates subjected to different thermal conditions. The analysis is conducted for four CNT dispersion patterns (UD, FG-V, FG-O, and FG-X), considering volume fractions of 0.12, 0.17, and 0.28. These volume fractions are associated with their respective efficiency parameters (η_1, η_2 and η_3), as detailed in Table 5.5. The thermal environment is characterized by temperature levels ranging from 300K to 500K. For accurate representation of the graded CNT distribution, the plates are discretized into 20 layers (i.e., N_L = 20).

The non-dimensional mathematical expression of the natural frequencies is given as: $\bar{\omega} = \omega(b^2 / h)\sqrt{\rho_0^m / E_0^m}$.

The boundary conditions are assumed to be as follows:

i. All edges are simply-supported (SSSS)

$$\begin{cases} v_0 = w_0 = \theta_y = 0 \\ u_0 = w_0 = \theta_x = 0 \end{cases} \text{ at } \begin{matrix} x = 0 \\ y = 0 \end{matrix}$$

ii. All edges are clamped (CCCC)

$u_0 = v_0 = w_0 = \theta_x = \theta_y = 0$ for all edges.

Table 5.5 Values of the CNT efficiency parameters

V_{CNT}^*	η_1	η_2	η_3
0.12	0.137	1.022	0.715
0.17	0.142	1.626	0.715
0.28	0.141	1.585	1.109

5.4.1. Effect of temperature and aspect ratio on the natural frequencies

Table 5.6 presents a comprehensive analysis of the effects of *a/b* ratios and temperature on the first five dimensionless frequencies of CCCC FG-CNTRC plates. Four CNT nanofiller distribution patterns, three distinct aspect ratios (*a/b* = 1, 1.5, and 2), and three temperature environments are considered. The power-law index and volume fraction are set to 1 and 0.12, respectively.

The results demonstrate a clear correlation between these parameters and the vibrational behavior of the plates. Increasing temperature leads to a decrease in plate frequencies due to the degradation of material properties under elevated temperatures. The FG-X distribution consistently offers the highest frequency values, indicating its superior stiffness properties compared to the other configurations. The aspect ratio (*a/b*) directly affects the plate's flexibility, with higher aspect ratios leading to increased flexibility and, consequently, lower natural frequencies.

Table 5.6 Effect of aspect ratio, distribution patterns and temperature environments on the non-dimensional frequency parameter of a fully clamped CNTRC plate

Distribution patterns	Mode number	a/b=1			a/b=1.5			a/b=2		
		300K	400K	500K	300K	400K	500K	300K	400K	500K
UD	1	25.5465	24.2646	22.8221	15.1756	14.5136	13.7761	10.8764	10.3826	9.8469
	2	30.7619	28.9997	27.0534	22.8381	21.4822	20.0074	20.1647	18.8799	17.4928
	3	42.6169	39.8784	36.8919	31.3039	29.7747	28.0558	21.2547	20.3393	19.3106
	4	52.3569	49.3851	46.0886	35.9134	33.9402	31.7567	27.4760	25.9647	24.3082
	5	55.2902	52.0383	48.4486	37.2944	34.8036	32.1059	34.9791	33.2137	30.5805
FG-V	1	23.8247	22.1173	20.1268	13.9422	12.8705	11.6251	10.1227	9.2550	8.2484
	2	29.5087	27.3799	24.9660	22.1860	20.5502	18.7285	19.4340	17.9073	16.1120
	3	41.9491	38.9283	35.5853	29.0786	26.9060	24.3574	19.8974	18.4080	16.7647
	4	49.9402	46.1457	41.7464	34.1787	31.6321	28.7149	26.2697	24.2773	22.0197
	5	53.1846	49.1434	44.5056	37.0965	34.4209	31.4961	32.3927	30.0070	27.2094
FG-O	1	22.2923	21.3418	20.2756	12.8908	12.3667	11.7990	9.4291	8.9794	8.5022
	2	28.0378	26.5227	24.8626	21.1659	19.8883	18.5124	17.9276	17.2524	16.5098
	3	40.3992	37.8329	35.0484	27.1557	26.0304	24.7676	19.1230	17.8673	16.5166
	4	47.7059	45.2946	42.5952	32.3541	30.6959	28.8744	24.8682	23.5114	22.0450
	5	51.0006	48.2468	45.1913	35.8612	33.4363	30.8187	30.2003	28.9763	27.6031
FG-X	1	27.2555	25.7656	24.0979	16.6062	15.8206	14.9398	11.9351	11.3799	10.7692
	2	32.4244	30.4811	28.3366	24.1604	22.7060	21.1166	21.1785	19.8361	18.3820
	3	44.3645	41.4648	38.3009	33.5241	31.7453	29.7575	23.2153	22.1147	20.8770
	4	54.7229	51.4649	47.8699	38.0337	35.8401	33.3585	29.2769	27.6145	25.7856
	5	57.6177	54.0961	50.2238	38.7665	36.1727	33.4169	36.9598	34.4315	31.6945

5.4.2. Effect of temperature and width-to-thickness ratio on the natural frequencies

Table 5.7 presents the results showing the influence of the width-to-thickness ratio (aspect ratio) on the non-dimensional frequency of a fully clamped square CNTRC plate. The analysis considers three width-to-thickness ratios (b/h = 10, 20, and 50), while keeping the CNT volume fraction (V_{CNT}^{*}) at 0.12 and setting the power law index (P_{in}) to 1. The findings reveal that increasing temperature leads to a decrease in the non-dimensional frequency ($\bar{\omega}$) across all distribution patterns and width-to-thickness ratios, highlighting the impact of thermal effects on the plate's vibrational behavior. Among the distribution patterns, the FG-X distribution exhibits the highest frequencies due to the concentration of CNTs in both the top and bottom layers, enhancing the plate's stiffness. In contrast, the FG-O distribution results in the lowest frequencies, as the CNTs are distributed more evenly throughout the thickness, offering less reinforcement compared to the FG-X configuration. This demonstrates how both the width-to-thickness ratio and CNT distribution patterns

significantly influence the vibrational properties of CNTRC plates under varying temperature conditions.

Table 5.7 Effect of width-to-thickness ratio, distribution patterns and temperature environments on the non-dimensional frequency parameter of a fully clamped CNTRC plate

Distribution patterns	Mode number	b/h=10			b/h=20			b/h=50		
		300K	400K	500K	300K	400K	500K	300K	400K	500K
UD	1	15.8763	14.8527	13.7297	25.5465	24.2646	22.8221	36.1066	35.2298	34.2757
	2	21.5581	20.0989	18.5103	30.7619	28.9997	27.0534	40.6385	39.2352	37.7313
	3	29.8060	27.8730	25.7602	42.6169	39.8784	36.8919	52.1812	49.6057	46.8522
	4	31.7449	29.5401	27.1490	52.3569	49.3851	46.0886	72.6577	68.2785	63.5745
	5	33.3058	31.0891	28.6742	55.2902	52.0383	48.4486	87.8186	84.9630	81.7194
FG-V	1	15.5641	14.3663	13.0086	23.8247	22.1173	20.1268	31.2603	27.2250	22.0165
	2	21.4218	19.8246	18.0545	29.5087	27.3799	24.9660	36.5677	32.4507	27.3711
	3	29.2870	26.9499	24.3017	41.9491	38.9283	35.5853	49.3717	44.7767	39.4102
	4	31.7665	29.4568	26.9310	49.9402	46.1457	41.7464	71.0668	65.3002	58.8178
	5	32.9532	30.3659	27.4650	53.1846	49.1434	44.5056	77.5239	70.4999	61.9865
FG-O	1	15.1409	14.2250	13.2138	22.2923	21.3418	20.2756	27.8736	27.2617	26.6360
	2	20.9130	19.5299	18.0221	28.0378	26.5227	24.8626	33.4199	32.1753	30.8821
	3	28.7096	26.9181	24.9542	40.3992	37.8329	35.0484	46.3935	43.8901	41.2391
	4	31.1293	28.9800	26.6488	47.7059	45.2946	42.5952	67.9083	63.5963	58.9776
	5	32.3309	30.2300	27.9378	51.0006	48.2468	45.1913	69.9234	68.1330	66.1737
FG-X	1	16.2766	15.1990	14.0210	27.2555	25.7656	24.0979	41.7429	40.5849	39.2883
	2	22.0822	20.5700	18.9260	32.4244	30.4811	28.3366	45.9022	44.2648	42.4699
	3	30.4452	28.4344	26.2398	44.3645	41.4648	38.3009	56.9217	54.1579	51.1704
	4	32.4397	30.1775	27.7252	54.7229	51.4649	47.8699	77.1505	72.5776	67.6445
	5	33.9978	31.7070	29.2137	57.6177	54.0961	50.2238	98.7043	94.9690	90.7040

5.4.3. Effect of temperature and volume fraction on the natural frequencies

The study investigates the effect of CNT volume fraction and temperature on the vibrational behavior of square composite plates with different CNT distribution patterns, subject to CCCC boundary conditions. The analysis considers three values of CNT volume fraction, with the width-to-thickness ratio fixed at 20. The results in Table 5.8 show that increasing the CNT volume fraction leads to higher stiffness, reflected by an increase in the non-dimensional frequency parameter ($\bar{\omega}$). Conversely, rising temperatures cause a reduction in the non-dimensional frequency, indicating a decrease in stiffness due to thermal softening. Four CNT distribution patterns (UD, FG-V, FG-O, and FG-X) are considered, with plates featuring the FG-X distribution exhibiting the highest stiffness, followed by those with uniform distribution (UD). Plates with the FG-O distribution show the lowest stiffness.

Table 5.8 Effect of volume fraction, distribution patterns and moisture concentration on the non-dimensional frequency parameter of a fully clamped CNTRC plate

Distribution patterns	Mode number	$V_{CNT}^{*} = 0.12$			$V_{CNT}^{*} = 0.17$			$V_{CNT}^{*} = 0.28$		
		300K	400K	500K	300K	400K	500K	300K	400K	500K
UD	1	25.5465	24.2646	22.8221	32.1433	30.5947	28.8475	35.8416	33.9583	31.8420
	2	30.7619	28.9997	27.0534	39.0704	36.8725	34.4446	42.6209	40.1285	37.3731
	3	42.6169	39.8784	36.8919	54.6194	51.1291	47.3244	58.3223	54.5528	50.4375
	4	52.3569	49.3851	46.0886	66.4402	62.7624	58.6694	72.6216	68.3890	63.7055
	5	55.2902	52.0383	48.4486	70.3492	66.2909	61.8009	76.3978	71.8137	66.7614
FG-V	1	23.8247	22.1173	20.1268	29.8259	27.8938	25.6565	34.0877	31.8649	29.2912
	2	29.5087	27.3799	24.9660	37.4675	34.9227	32.0576	41.6258	38.7989	35.6081
	3	41.9491	38.9283	35.5853	53.9069	50.1284	45.9664	58.4426	54.3538	49.8413
	4	49.9402	46.1457	41.7464	63.1753	58.7841	53.7173	70.7849	65.7787	60.0298
	5	53.1846	49.1434	44.5056	67.5627	62.8040	57.3715	75.0423	69.6864	63.5882
FG-O	1	22.2923	21.3418	20.2756	27.7271	26.6100	25.3569	31.8523	30.4737	28.9151
	2	28.0378	26.5227	24.8626	35.2725	33.4004	31.3538	38.6866	36.6328	34.3677
	3	40.3992	37.8329	35.0484	51.3093	48.0614	44.5420	54.1101	50.7279	47.0475
	4	47.7059	45.2946	42.5952	60.0468	57.1486	53.8892	67.7617	64.2615	60.3391
	5	51.0006	48.2468	45.1913	64.3921	61.0295	57.2890	71.5689	67.6733	63.3412
FG-X	1	27.2555	25.7656	24.0979	34.6415	32.8098	30.7532	38.8083	36.6139	34.1642
	2	32.4244	30.4811	28.3366	41.6839	39.2240	36.5075	46.5108	43.6594	40.5171
	3	44.3645	41.4648	38.3009	57.6793	53.9275	49.8344	64.0666	59.8343	55.2184
	4	54.7229	51.4649	47.8699	69.9700	65.8812	61.3585	77.1593	72.4873	67.3405
	5	57.6177	54.0961	50.2238	73.9398	69.4845	64.5770	81.4981	76.4423	70.8907

5.4.4. Effect of temperature and boundary conditions on the natural frequencies

The Figure 5.2 presents a graphical representation of the influence of boundary conditions on the dimensionless fundamental frequency of CNTRC plates subjected to varying temperature conditions. The study considers plates with geometric parameters *b/h* = 10 and *a/b* = 1, and the boundary conditions are denoted using 'C' for clamped and 'S' for simply supported edges, as illustrated in Figure 5.1. The results indicate that for all boundary condition configurations, the dimensionless frequency decreases progressively as the temperature increases from 300K to 500K, highlighting the thermal softening effect on the composite structure. The highest frequencies correspond to plates with CSCS boundary conditions, while simply supported plates (SSSS) exhibit the lowest frequencies, with intermediate configurations lying in between. Notably, regardless of the boundary condition, plates with FG-X CNT distribution consistently demonstrate the highest frequency values, suggesting enhanced stiffness compared to other CNT distributions. This graphical representation (Figure 5.2) further reinforces the significant impact of boundary conditions,

temperature variation, and CNT distribution on the vibrational characteristics of CNTRC plates, providing valuable insights for the optimization of thermomechanical structural performance.

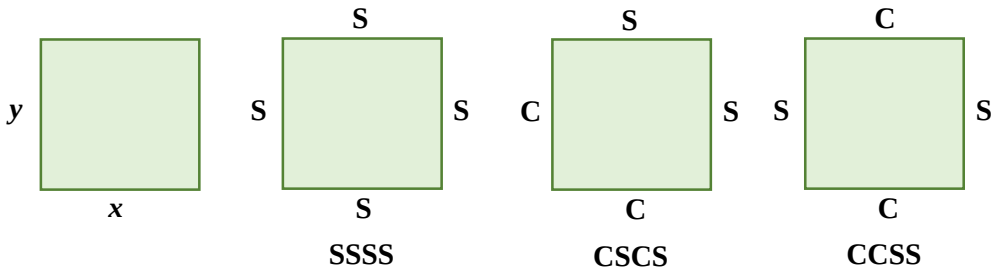

Figure 5.1 : Combinations of boundary conditions

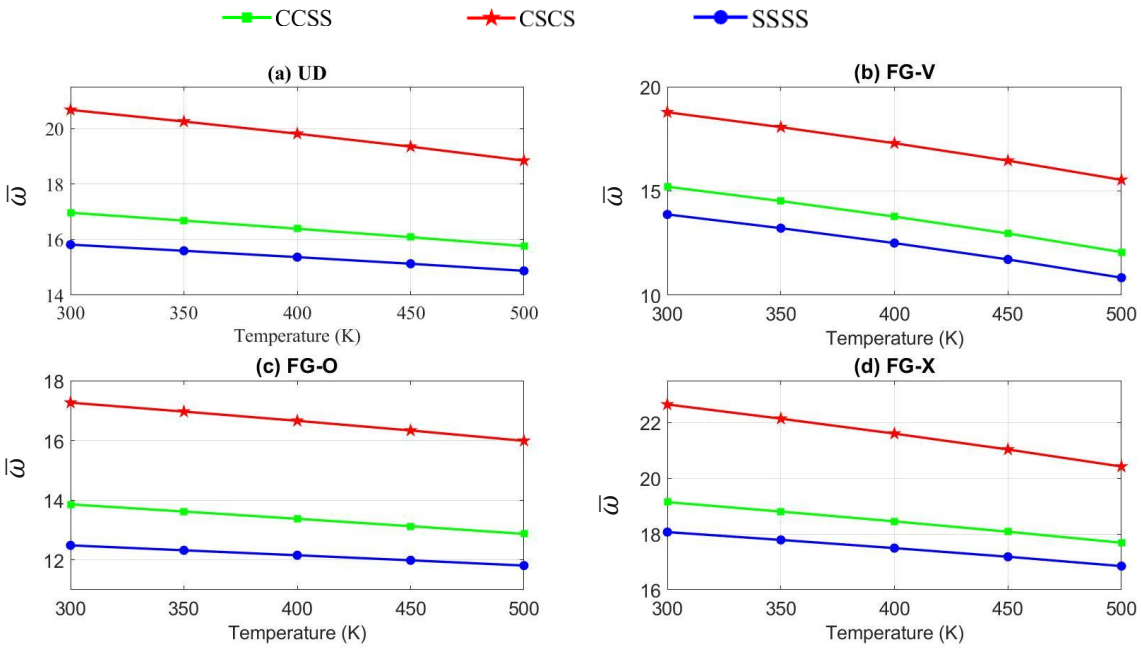

Figure 5.2 : Variation of dimensionless frequency with temperature for CNTRC plates under different boundary conditions and CNT distributions.

5.5 Free vibrations analysis of FG-CNTRC plates under hygrothermal environments

This section presents a comprehensive parametric investigation to elucidate the effect of moisture content and hygrothermal conditions on a range of parameters, which include *(i)* width-to-thickness ratio, *(ii)* length-to-width ratio, *(iii)* CNTs volume fraction, *(iv)* boundary conditions, *(v)* linear and non-linear distributions of CNTs, and *(vi)* hygrothermal environments, on the free vibration characteristics of FG-CNTRC plates.

The FG nanocomposite plates consist of PMMA polymer matrix reinforced with armchair (10, 10) single-walled carbon nanotubes. The PMMA matrix material properties are assumed

to be temperature and moisture-dependent, a consideration that is crucial for accurately predicting and understanding material behavior under varying hygrothermal conditions. They are presented as follows [61], [66], [67], [108], [109]:

$$\nu^m = 0.34\,, \quad \rho^m = 1200\,\text{kg/m}^3 \tag{5. 9}$$

$$E^m = (3.51 - 0.003T - 0.142C)\ \text{GPa} \tag{5. 10}$$

$$\alpha^m = 45(1 + 0.0001\Delta T) \times 10^{-6} / K \tag{5. 11}$$

$$\beta^m = 2.68 \times 10^{-3} / wt.\%\ \text{of}\ H_2O \tag{5. 12}$$

This part examines the influence of moisture on the mechanical behavior of CNT-reinforced composite plates under hygrothermal conditions. Four different CNT distribution patterns (UD, FG-V, FG-O, and FG-X) are considered, evaluated at three volume fractions: 0.12, 0.17, and 0.28. To systematically assess the effect of moisture absorption, the analysis includes seven moisture concentration levels of 0%, 0.5%, 1%, 1.5%, 2%, 3%, and 4%. The composite plates are discretized into 20 layers to ensure a smooth gradient in CNT distribution across the thickness.

The non-dimensional expression for the natural frequencies is given as: $\bar{\omega} = \omega(b^2 / h)\sqrt{\rho_0^m / E_0^m}$

5.5.1. Effect of width-to-thickness ratio and CNTs distribution patterns in different moisture environments

The impact of moisture content, width-to-thickness ratios, and CNT distribution patterns on the vibrational behavior of fully clamped (CCCC) FG-CNTRC plates is analyzed in Table 5.9. The investigation considers a fixed CNT volume fraction ($V_{CNT}^* = 0.12$) and an aspect ratio ($a / b = 1$). The analysis focuses on the first three non-dimensional frequencies ($\bar{\omega}$) of the plates.

The findings indicate that an increase in moisture content results in a reduction in non-dimensional natural frequencies, regardless of the CNT distribution pattern. In contrast, higher width-to-thickness ratios (*b/h*) are associated with increased non-dimensional frequencies. This behavior is attributed to the enhanced effective stiffness of plates with larger *b/h* ratios, leading to higher natural frequencies.

Table 5.9 Effect of width-to-thickness ratio, distribution patterns and moisture concentration on the non-dimensional frequency parameter of a fully clamped CNTRC plate (a/b = 1, $V_{CNT}^{*} = 0.12$)

b/h	Distribution patterns	mode number	Moisture concentration (%)						
			0	0.5	1	1.5	2	3	4
10	UD	1	15.8880	15.8721	15.8562	15.8402	15.8243	15.7923	15.7603
		2	21.5999	21.5856	21.5713	21.5570	21.5427	21.5140	21.4853
		3	29.8335	29.8014	29.7692	29.7370	29.7047	29.6401	29.5753
	FG-V	1	15.5647	15.5491	15.5336	15.5180	15.5024	15.4711	15.4398
		2	21.4582	21.4443	21.4303	21.4164	21.4025	21.3746	21.3467
		3	29.3010	29.2698	29.2385	29.2072	29.1758	29.1131	29.0501
	FG-O	1	15.1304	15.1145	15.0986	15.0827	15.0668	15.0348	15.0028
		2	20.9414	20.9274	20.9133	20.8992	20.8851	20.8568	20.8285
		3	28.7106	28.6790	28.6473	28.6155	28.5838	28.5201	28.4563
	FG-X	1	16.2990	16.2840	16.2688	16.2537	16.2386	16.2083	16.1779
		2	22.1321	22.1183	22.1046	22.0909	22.0771	22.0496	22.0221
		3	30.4865	30.4560	30.4254	30.3948	30.3642	30.3028	30.2413
20	UD	1	25.4352	25.3968	25.3583	25.3198	25.2812	25.2038	25.1261
		2	30.7077	30.6711	30.6345	30.5978	30.5611	30.4876	30.4139
		3	42.6492	42.6163	42.5834	42.5505	42.5175	42.4515	42.3855
	FG-V	1	23.6892	23.6494	23.6095	23.5696	23.5295	23.4493	23.3687
		2	29.4423	29.4054	29.3685	29.3315	29.2945	29.2202	29.1458
		3	41.9795	41.9470	41.9145	41.8819	41.8494	41.7842	41.7189
	FG-O	1	22.1399	22.0971	22.0543	22.0113	21.9682	21.8818	21.7950
		2	27.9602	27.9214	27.8826	27.8437	27.8047	27.7266	27.6483
		3	40.4215	40.3881	40.3546	40.3212	40.2877	40.2206	40.1534
	FG-X	1	27.1789	27.1442	27.1095	27.0748	27.0399	26.9702	26.9002
		2	32.3967	32.3629	32.3291	32.2952	32.2614	32.1935	32.1255
		3	44.4153	44.3841	44.3529	44.3217	44.2904	44.2278	44.1652
50	UD	1	35.6430	35.4622	35.2802	35.0972	34.9130	34.5414	34.1651
		2	40.2631	40.0854	39.9067	39.7272	39.5467	39.1829	38.8152
		3	51.9661	51.8063	51.6459	51.4850	51.3235	50.9988	50.6718
	FG-V	1	30.8519	30.6485	30.4435	30.2370	30.0288	29.6074	29.1791
		2	36.2588	36.0664	35.8727	35.6779	35.4819	35.0860	34.6850
		3	49.2255	49.0606	48.8950	48.7288	48.5619	48.2262	47.8877
	FG-O	1	27.5002	27.2698	27.0373	26.8024	26.5652	26.0834	25.5913
		2	33.1487	32.9369	32.7234	32.5083	32.2917	31.8532	31.4078
		3	46.2793	46.1034	45.9266	45.7491	45.5707	45.2116	44.8491
	FG-X	1	41.2500	41.1025	40.9545	40.8058	40.6565	40.3560	40.0529
		2	45.4894	45.3397	45.1894	45.0385	44.8871	44.5825	44.2756
		3	56.6662	56.5251	56.3836	56.2417	56.0994	55.8137	55.5264
100	UD	1	38.4698	37.7671	37.0496	36.3162	35.5659	34.0099	32.3708
		2	42.9633	42.2694	41.5626	40.8421	40.1073	38.5908	37.0053
		3	54.5058	53.8809	53.2479	52.6063	51.9557	50.6265	49.2570
	FG-V	1	32.5608	31.7581	30.9320	30.0808	29.2020	27.3508	25.3508
		2	37.9076	37.1455	36.3656	35.5665	34.7469	33.0397	31.2287
		3	50.9005	50.2501	49.5900	48.9197	48.2388	46.8432	45.3985
	FG-O	1	28.6628	27.7444	26.7910	25.7986	24.7622	22.5323	20.0321
		2	34.2844	33.4381	32.5670	31.6691	30.7419	28.7874	26.6735
		3	47.5071	46.8091	46.0989	45.3759	44.6393	43.1224	41.5411
	FG-X	1	45.8933	45.3347	44.7683	44.1936	43.6104	42.4170	41.1847
		2	49.9213	49.3508	48.7730	48.1874	47.5938	46.3811	45.1323
		3	60.7096	60.1688	59.6227	59.0709	58.5133	57.3803	56.2220

Table 5.9 reveals a trend where increasing moisture content leads to decreasing non-dimensional frequencies across all distribution patterns. Conversely, an increase in the

width-to-thickness ratio (*b/h*) demonstrates a positive influence on the non-dimensional frequencies ($\bar{\omega}$) as shown in Table 5.9. Plates with larger width-to-thickness ratios exhibit higher natural frequencies compared to those with smaller ratios, leading to increased effective stiffness. Furthermore, Table 5.9 highlights a significant influence of CNT distribution patterns on $\bar{\omega}$. Plates with the FG-X distribution pattern consistently exhibit the highest frequencies, while those with the FG-O pattern exhibit the lowest. This disparity can be attributed to the strategic placement of CNTs in FG-X plates. The higher concentration of CNTs in the upper and lower layers enhances the overall stiffness of the FG-X plate, resulting in its higher vibration frequencies. In contrast, FG-O plates concentrate CNTs in the mid-plane. This distribution pattern offers less overall stiffness compared to FG-X, leading to the observed lower natural frequencies.

5.5.2. Effect of aspect ratio and CNTs distribution patterns in different moisture environments

The numerical study summarized in Table 5.10 investigates the combined effects of length-to-width ratios (*a/b*), CNT distribution patterns, and moisture concentrations on the first three non-dimensional natural frequencies ($\bar{\omega}$) of fully clamped FG-CNTRC plates. The analysis is performed with a fixed width-to-thickness ratio (*b/h = 50*) and a constant CNT volume fraction ($V_{CNT}^{*} = 0.12$).

The results in Table 5.10 demonstrate a consistent reduction in the non-dimensional natural frequencies as the aspect ratio (*a/b*) and moisture content increase, irrespective of the CNT distribution pattern. This behavior highlights the detrimental effect of moisture on the stiffness of the composite plates, as elevated moisture levels are correlated with lower $\bar{\omega}$ values. The findings underline the significant influence of environmental factors on the dynamic response of FG-CNTRC plates. Moreover, the CNT distribution pattern is shown to play a critical role in determining vibrational performance. Plates with an FG-X distribution exhibit the highest non-dimensional natural frequencies due to the higher reinforcement of their outer layers, which enhances stiffness. In contrast, FG-O plates, where CNTs are concentrated near the mid-plane, display lower frequencies due to reduced overall stiffness.

Table 5.10 Effect of aspect ratio, distribution patterns and moisture concentration on the non-dimensional frequency parameter of a fully clamped CNTRC plate.

a/b	Distribution patterns	Mode number	Moisture concentration (%)						
			0	0.5	1	1.5	2	3	4
1	UD	1	35.6430	35.4622	35.2802	35.0972	34.9130	34.5414	34.1651
		2	40.2631	40.0854	39.9067	39.7272	39.5467	39.1829	38.8152
		3	51.9661	51.8063	51.6459	51.4850	51.3235	50.9988	50.6718
	FG-V	1	30.8519	30.6485	30.4435	30.2370	30.0288	29.6074	29.1791
		2	36.2588	36.0664	35.8727	35.6779	35.4819	35.0860	34.6850
		3	49.2255	49.0606	48.8950	48.7288	48.5619	48.2262	47.8877
	FG-O	1	27.5002	27.2698	27.0373	26.8024	26.5652	26.0834	25.5913
		2	33.1487	32.9369	32.7234	32.5083	32.2917	31.8532	31.4078
		3	46.2793	46.1034	45.9266	45.7491	45.5707	45.2116	44.8491
	FG-X	1	41.2500	41.1025	40.9545	40.8058	40.6565	40.3560	40.0529
		2	45.4894	45.3397	45.1894	45.0385	44.8871	44.5825	44.2756
		3	56.6662	56.5251	56.3836	56.2417	56.0994	55.8137	55.5264
1.5	UD	1	17.9805	17.8099	17.6375	17.4631	17.2867	16.9278	16.5600
		2	25.6265	25.4818	25.3361	25.1894	25.0417	24.7434	24.4409
		3	41.4189	41.3034	41.1876	41.0714	40.9548	40.7205	40.4847
	FG-V	1	15.7280	15.5392	15.3477	15.1535	14.9564	14.5533	14.1371
		2	24.2407	24.0921	23.9424	23.7917	23.6398	23.3326	23.0206
		3	37.6698	37.3983	37.1246	36.8487	36.5706	36.0073	35.4342
	FG-O	1	14.1375	13.9262	13.7113	13.4926	13.2697	12.8109	12.3328
		2	22.7758	22.6176	22.4581	22.2972	22.1349	21.8061	21.4713
		3	33.5256	33.2186	32.9084	32.5951	32.2785	31.6348	30.9767
	FG-X	1	20.9181	20.7788	20.6384	20.4969	20.3543	20.0656	19.7722
		2	28.1568	28.0296	27.9018	27.7734	27.6442	27.3839	27.1208
		3	43.8573	43.7504	43.6431	43.5356	43.4278	43.2113	42.9937
2	UD	1	11.8696	11.7100	11.5479	11.3832	11.2157	10.8719	10.5154
		2	21.5725	21.4494	21.3255	21.2007	21.0750	20.8210	20.5632
		3	26.3927	26.1563	25.9176	25.6765	25.4329	24.9380	24.4321
	FG-V	1	10.7507	10.5800	10.4061	10.2288	10.0479	9.6744	9.2837
		2	21.1066	20.9837	20.8600	20.7353	20.6097	20.3556	20.0976
		3	22.7824	22.5177	22.2495	21.9778	21.7024	21.1399	20.5608
	FG-O	1	9.8713	9.6847	9.4939	9.2986	9.0984	8.6819	8.2411
		2	20.1552	19.9969	19.6931	19.3842	19.0699	18.4238	17.7523
		3	20.2957	20.0266	19.8970	19.7663	19.6345	19.3675	19.0957
	FG-X	1	13.5411	13.4074	13.2720	13.1352	12.9966	12.7145	12.4251
		2	23.0338	22.9216	22.8087	22.6952	22.5810	22.3506	22.1175
		3	30.8786	30.6868	30.4937	30.2993	30.1035	29.7077	29.3062

5.5.3. Effect of volume fraction and CNTs distribution patterns in different moisture environments

Figure 5.3 illustrates the influence of CNT volume fractions and distribution patterns on the fundamental non-dimensional frequencies of SSSS square FG-CNTRC plates. The analysis explores various moisture environments while maintaining a fixed aspect ratio (b/h) of 50.

The results clearly demonstrate a significant increase in $\bar{\omega}$ with increasing CNT volume fraction from 0.12 to 0.28. This suggests a direct correlation between higher CNT content

and enhanced effective stiffness of the plates. The figure consistently reveals a decrease in $\bar{\omega}$ parameter across all CNT volume fractions and distribution patterns as the moisture concentration increases from 0% (i.e., reference moisture) to 4%. This trend reinforces the potential weakening effect of moisture exposure on the overall stiffness of the FG-CNTRC plates. Consistent with prior findings (Tables 5.9 and 5.10), Figure 5.3 reaffirms that FG-X plates exhibit higher natural frequencies compared to UD, FG-V, and FG-O plates.

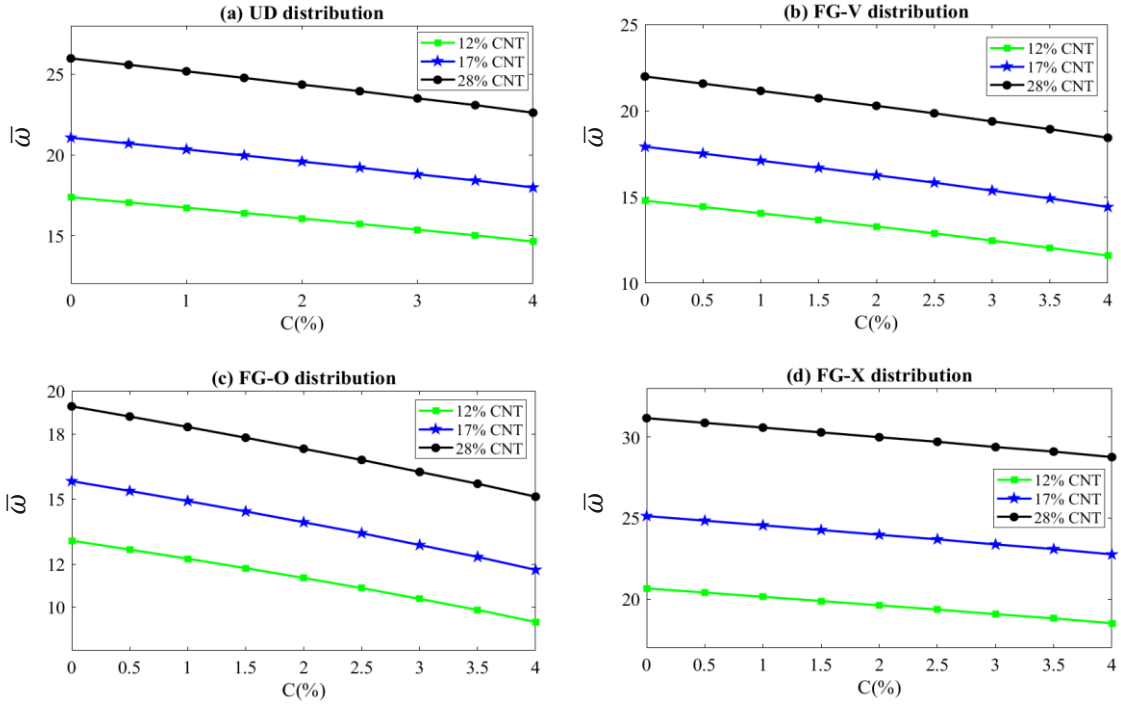

Figure 5.3 : Effect of volume fraction, distribution patterns, and moisture concentration on the non-dimensional frequency parameter of a simply supported CNTRC plate

5.5.4. Effect of boundary conditions and CNTs distribution patterns in different moisture environment

Table 5.11 digs deeper into exploring the influence of boundary conditions, CNT distribution patterns, and moisture concentrations on the fundamental natural frequencies of square FG-CNTRC. In the modeling, the b/h and V_{CNT}^{*} are set to 50 and 0.12, respectively. Notably, boundary conditions are represented by notations: "F" for free, "S" for simply-supported, and "C" for clamped edges. Figure 5.4 presents the boundary condition combinations considered in the present analysis. Table 5.11 confirms a consistent decrease in $\bar{\omega}$ with increasing moisture concentration for all combinations of boundary conditions investigated. This observation aligns with previous findings (Tables 5.9, 5.10, and Fig. 5.3), suggesting a potential weakening effect of moisture on the stiffness of FG-CNTRC plates. Furthermore, Table 5.11 reaffirms the superiority of FG-X distribution pattern in term of

frequency across all the boundary conditions considered in this investigation, followed by UD distribution while FG-O exhibit the lowest frequencies. In consequence, the mechanical integrity of plates possessing fully clamped edges in the FG-X configuration is established as superlative, rendering them as the stiffer structures among the array of plates considered in this analysis.

Table 5.11 Influence of boundary conditions, distribution patterns and moisture concentration on the fundamental non-dimensional frequency

Boundary conditions	Distribution patterns	Moisture concentration (%)						
		0	0.5	1	1.5	2	3	4
CCCC	UD	35.6430	35.4622	35.2802	35.0972	34.9130	34.5414	34.1651
	FG-V	30.8519	30.6485	30.4435	30.2370	30.0288	29.6074	29.1791
	FG-O	27.5002	27.2698	27.0373	26.8024	26.5652	26.0834	25.5913
	FG-X	41.2500	41.1025	40.9545	40.8058	40.6565	40.3560	40.0529
CSSS	UD	35.6411	35.4603	35.2783	35.0953	34.9112	34.5395	34.1633
	FG-V	30.8461	30.6426	30.4377	30.2311	30.0229	29.6015	29.1732
	FG-O	27.4987	27.2683	27.0358	26.8009	26.5637	26.0820	25.5899
	FG-X	41.2478	41.1004	40.9524	40.8037	40.6544	40.3539	40.0508
CSCS	UD	25.8385	25.5972	25.3533	25.1069	24.8578	24.3513	23.8331
	FG-V	22.1403	21.8679	21.5918	21.3118	21.0277	20.4467	19.8473
	FG-O	19.6380	19.3291	19.0148	18.6947	18.3686	17.6968	16.9963
	FG-X	30.3577	30.1628	29.9666	29.7689	29.5698	29.1672	28.7584
CCSS	UD	18.5105	18.2091	17.9026	17.5908	17.2734	16.6204	15.9407
	FG-V	16.1486	15.8167	15.4776	15.1310	14.7762	14.0398	13.2627
	FG-O	14.4986	14.1279	13.7473	13.3558	12.9525	12.1057	11.1951
	FG-X	21.7026	21.4566	21.2076	20.9557	20.7008	20.1812	19.6480
SSSS	UD	17.3663	17.0475	16.7227	16.3914	16.0533	15.3548	14.6230
	FG-V	14.7819	14.4219	14.0526	13.6735	13.2835	12.4671	11.5933
	FG-O	13.0783	12.6700	12.2480	11.8110	11.3572	10.3904	9.3239
	FG-X	20.6684	20.4123	20.1529	19.8901	19.6238	19.0801	18.5206
CCCF	UD	9.3802	9.0872	8.7784	8.4517	8.1043	7.3325	6.4207
	FG-V	8.8220	8.5205	8.1998	7.8564	7.4860	6.6404	5.5862
	FG-O	8.2554	7.9306	7.5800	7.1979	6.7769	5.7697	4.3754
	FG-X	10.4194	10.1690	9.9089	9.6381	9.3555	8.7496	8.0770

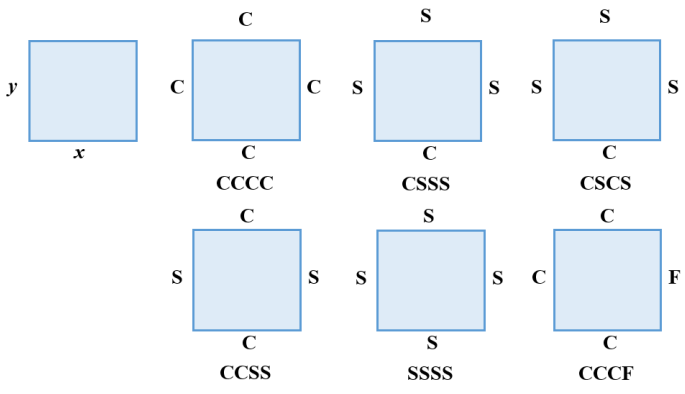

Figure 5.4 : Boundary conditions combinations

5.5.5. Effect of power-law index and CNTs distribution patterns in different moisture environments

The study investigates the influence of the power-law exponent (P_{in}) on the non-dimensional natural frequencies ($\bar{\omega}$) of simply-supported FG-CNTRC square plates, the finding are presented in Table 5.12. P_{in} governs the distribution of CNTs across the plate thickness in a uniform, linear, or non-linear way. The analysis takes into consideration different moisture concentrations and distribution types of CNTs. Notably, parameters b/h and V_{CNT}^{*} are set at 50 and 0.12, respectively.

Table 5.12 First five non-dimensional frequencies on the non-dimensional frequency parameter of FG-CNTRC plate

		Moisture concentration (1%)			**Moisture concentration (2%)**			**Moisture concentration (3%)**		
P_{in}	Mode number	FG-V	FG-O	FG-X	FG-V	FG-O	FG-X	FG-V	FG-O	FG-X
0	1	16.7227	16.7227	16.7227	16.0533	16.0533	16.0533	15.3548	15.3548	15.3548
	2	21.4019	21.4019	21.4019	20.8214	20.8214	20.8214	20.2243	20.2243	20.2243
	3	33.4756	33.4756	33.4756	33.0423	33.0423	33.0423	32.6034	32.6034	32.6034
	4	53.2499	53.2499	53.2499	52.9214	52.9214	52.9214	52.5910	52.5910	52.5910
	5	62.3479	62.3479	62.3479	61.6594	61.6594	61.6594	60.9631	60.9631	60.9631
0.4	1	15.6631	14.6208	18.4296	14.9537	13.8567	17.8292	14.2090	13.0481	17.2081
	2	20.5878	19.6947	22.8627	19.9891	19.0671	22.3240	19.3721	18.4183	21.7720
	3	32.9422	32.1376	34.7032	32.5051	31.6891	34.2876	32.0622	31.2343	33.8670
	4	52.8701	51.9713	54.4942	52.5412	51.6367	54.1743	52.2104	51.3001	53.8526
	5	58.7690	55.2404	67.8707	58.0462	54.4698	67.2430	57.3142	53.6882	66.6094
0.8	1	14.5580	12.9379	19.6583	13.8081	12.0874	19.1089	13.0153	11.1725	18.5433
	2	19.8353	18.4172	23.9514	19.2248	17.7578	23.4475	18.5943	17.0731	22.9327
	3	32.6101	31.2171	35.6678	32.1751	30.7627	35.2697	31.7344	30.3016	34.8672
	4	52.8510	49.2833	55.5172	52.5257	48.4384	55.2066	52.1985	47.5786	54.8944
	5	54.8892	51.1570	71.7038	54.1317	50.8216	71.1224	53.3635	50.3720	70.5363
1	1	14.0526	12.2480	20.1529	13.2835	11.3572	19.6238	12.4671	10.3904	19.0801
	2	19.5227	17.9237	24.3990	18.9084	17.2527	23.9097	18.2735	16.5548	23.4102
	3	32.5264	30.8899	36.0791	32.0937	30.4346	35.6888	31.6553	29.9726	35.2944
	4	52.9541	46.7709	55.9680	52.2922	45.8912	55.6618	51.5063	44.9944	55.3539
	5	53.0665	49.6694	73.2165	52.6313	48.8204	72.6539	52.3067	47.9564	72.0870
1.4	1	13.1547	11.1079	20.9727	12.3500	10.1426	20.4774	11.4891	9.0754	19.9698
	2	19.0223	17.1623	25.1543	18.4045	16.4756	24.6900	17.7653	15.7592	24.2169
	3	32.4922	30.4448	36.7976	32.0661	29.9908	36.4214	31.6345	29.5299	36.0413
	4	49.7446	42.5174	56.7812	48.9387	41.5731	56.4828	48.1193	40.6068	56.1830
	5	52.7140	45.7277	75.6881	51.9334	44.8275	75.1572	51.1411	43.9089	74.6226
1.8	1	12.3951	10.2116	21.6256	11.5598	9.1806	21.1578	10.6594	8.0183	20.6794
	2	18.6529	16.6213	25.7703	18.0361	15.9271	25.3271	17.3977	15.2014	24.8761
	3	32.5647	30.1954	37.4122	32.1467	29.7454	37.0483	31.7234	29.2887	36.6809
	4	46.8441	39.0700	57.5077	46.0101	38.0680	57.2164	45.1608	37.0389	56.9237
	5	50.1034	42.5883	77.6265	49.3026	41.6455	77.1221	48.4887	40.6808	76.6143

Interestingly, the effect of P_{in} on $\bar{\omega}$ differs based on the CNT distribution. For FG-O and FG-V plates, higher values of P_{in} with increased reinforcement concentration in the center (FG-O) or upper layers (FG-V) leads to a decrease in $\bar{\omega}$, suggesting reduced stiffness. In contrast, FG-X plates exhibit the opposite trend, with $\bar{\omega}$ increasing as P_{in} rises. This is attributed to the strategic placement of CNTs in the FG-X pattern, where a higher P_{in}

concentrates reinforcements in the top and bottom layers, enhancing overall stiffness. Importantly, the study confirms a consistent decrease in $\bar{\omega}$ with increasing moisture content for all P_{in} values and CNT distribution patterns, reinforcing the potential weakening effect of moisture on the stiffness of FG-CNTRC plates.

5.5.6. Effect of hygrothermal environments and CNTs distribution patterns

Table 5.13 and Figure 5.5 examine the interplay between moisture concentrations and temperature environments on the non-dimensional frequencies of different patterns of FG-CNTRC plates. The examination is made for $b/h = 10$ and $V_{CNT}^{*} = 0.12$.

Both Table 5.13 and Figure 5.5 consistently reveal a decrease in the vibrational behavior of nanocomposite plates with increasing moisture concentration and temperature. These findings align with the understanding that higher temperatures and moisture concentrations reduce the effective stiffness of the constituent materials. Figure 5.5 further highlights the influence of boundary conditions. Plates with fully clamped edges (CCCC) exhibit demonstrably higher $\bar{\omega}$ values compared to simply supported configuration across all temperatures and moisture levels. It is important to note that in both Table 5.13 and Figure 5.5, FG-X plates are the least impacted by rising temperature and moisture concentration, followed by UD plates, FG-V plates, and FG-O plates.

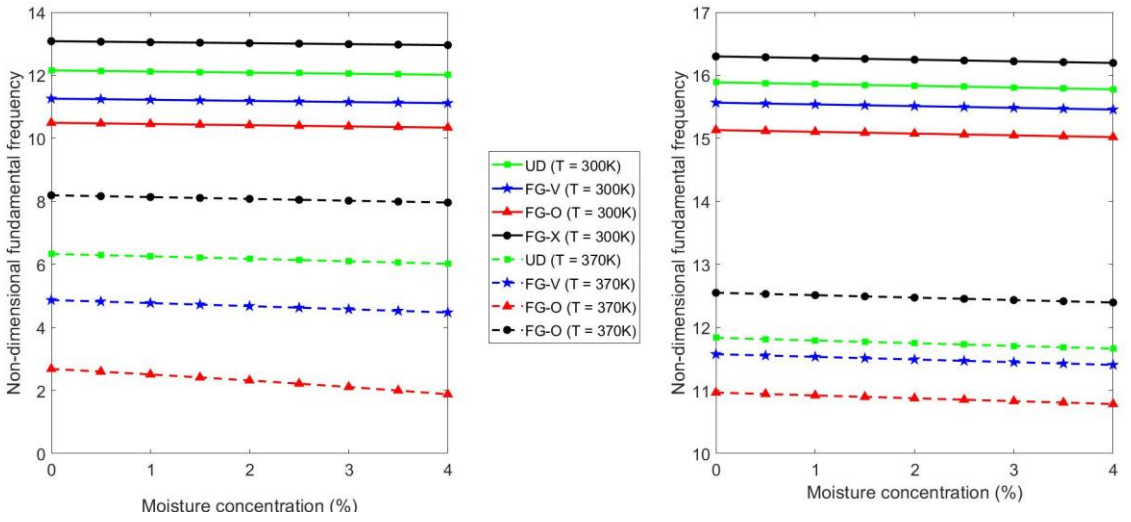

(a) simply supported CNTRC (b) fully claimed CNTRC plate

Figure 5.5 : Effect of hygrothermal environments and distribution patterns on the non-dimensional fundamental frequency of (a) SSSS CNTRC plate and (b) CCCC CNTRC plate

Table 5.13 Influence of hygrothermal environment on the non-dimensional frequencies of CNTRC square plate

Temperature (K)	Distribution patterns	Moisture concentration (%)						
		0	**0.5**	**1**	**1.5**	**2**	**3**	**4**
330	UD	10.0050	9.9821	9.9592	9.9362	9.9132	9.8670	9.8205
		14.9220	14.9041	14.8861	14.8682	14.8502	14.8141	14.7780
		15.5044	15.4883	15.4722	15.4561	15.4400	15.4077	15.3753
		16.7762	16.7733	16.7705	16.7676	16.7647	16.7589	16.7532
		25.0635	25.0260	24.9885	24.9509	24.9132	24.8377	24.7620
	FG-X	11.1410	11.1209	11.1007	11.0805	11.0603	11.0198	10.9791
		15.6147	15.5993	15.5839	15.5685	15.5530	15.5221	15.4911
		15.8474	15.8306	15.8139	15.7971	15.7803	15.7467	15.7131
		16.8282	16.8253	16.8225	16.8196	16.8167	16.8109	16.8051
		26.0289	26.0150	26.0010	25.9871	25.9731	25.9438	25.8733
350	UD	8.2736	8.2461	8.2184	8.1907	8.1628	8.1069	8.0506
		13.6074	13.5879	13.5683	13.5487	13.5290	13.4897	13.4502
		14.3241	14.3068	14.2894	14.2720	14.2546	14.2197	14.1848
		16.5405	16.5376	16.5347	16.5318	16.5289	16.5232	16.5174
		22.2931	22.2511	22.2090	22.1668	22.1246	22.0398	21.9548
	FG-X	9.6380	9.6148	9.5916	9.5684	9.5451	9.4983	9.4512
		14.4803	14.4637	14.4471	14.4306	14.4140	14.3807	14.3473
		14.6197	14.6017	14.5837	14.5656	14.5476	14.5113	14.4750
		16.5919	16.5890	16.5861	16.5832	16.5803	16.5745	16.5687
		23.5682	23.5295	23.4908	23.4520	23.4131	23.3352	23.2570
390	UD	2.3068	2.2067	2.1018	1.9914	1.8745	1.6156	1.3063
		10.5162	10.4912	10.4661	10.4409	10.4157	10.3652	10.3143
		11.6140	11.5927	11.5714	11.5500	11.5287	11.4858	11.4428
		15.3291	15.2683	15.2073	15.1460	15.0845	14.9607	14.8359
		16.0637	16.0607	16.0578	16.0549	16.0519	16.0460	16.0402
	FG-X	5.5306	5.4904	5.4500	5.4093	5.3683	5.2852	5.2009
		11.8084	11.7864	11.7644	11.7423	11.7201	11.6757	11.6312
		11.8951	11.8751	11.8550	11.8349	11.8148	11.7745	11.7340
		16.1137	16.1108	16.1078	16.1049	16.1020	16.0961	16.0902
		17.2815	17.2291	17.1765	17.1237	17.0708	16.9644	16.8574

5.6 Nano-composite *vs.* carbon/PMMA plate

The final study aims to determine the carbon fibers volume fraction required to achieve a comparable stiffness to that of polymeric nanocomposite plates reinforced with CNTs. Both the CNT-reinforced nanocomposite and carbon fiber-reinforced composite plates use PMMA as a matrix. The CNTs maintain the same material properties used throughout this study, with specific properties of the chosen carbon fiber provided as follows: $E_{11}^{F} = 233.05GPa$, $G_{12}^{F} = 8.96GPa$, $\upsilon^{F} = 0.6$, $\rho^{F} = 2267\,Kg/m^{3}$, $\alpha_{11} = -0.54\times10^{-6}/K$, and $\alpha_{22} = 10.8\times10^{-6}/K$.

Table 5.14 listed the fundamental frequencies of fully clamped FG-X nanocomposite and carbon reinforced composite plates exposed to different thermal environments (300K, 400K, and 500K). The analysis is conducted for a fixed b/h and V_{CNT}^{*} of 50 and 0.12, respectively. As evident from Table 5.14, at a reference temperature of 300K and with a 12% CNT volume fraction, FG-X nanocomposite plates exhibit significantly higher fundamental frequencies compared to carbon-reinforced composites, even at a much higher

volume fraction (64%) of reinforcing fibers. This highlights the superior stiffness offered by CNT reinforcement in the FG-X configuration at the reference temperature.

However, the data also suggests a vulnerability of CNT performance to elevated temperatures. Table 5.14 reveals that the required volume fraction of carbon fibers to achieve comparable stiffness to the FG-X plate (12% CNT volume fraction) progressively decreases from 64% at 300K to 61% at 400K and further down to 57% at 500K. This trend indicates a decline in the relative effectiveness of CNT reinforcement with increasing thermal exposure.

Table 5.14 First natural frequencies for different volume fraction of carbon/PMMA plate

	Temperature (300K)		**Temperature (400K)**		**Temperature (500K)**	
Fiber volume fraction (%)	Carbon/ PMMA	CNTs/PMMA FG-X	Carbon/ PMMA	CNTs/PMMA FG-X	Carbon/ PMMA	CNTs/PMMA FG-X
12	598.440	968.308	592.287	949.795	586.033	927.761
17	658.072		652.648		647.144	
28	760.842		756.315		751.732	
35	812.628		808.399		804.121	
40	845.074		840.972		836.824	
50	901.544		897.511		893.437	
57	936.170		932.035		927.860	
61	954.699		950.440			
63.2	964.612					
64	968.179					

5.7 Mode shapes

Furthermore, Figure 5.6 is plotted to investigate the effect of hygrothermal environments on the first six mode shapes of square fully clamped FG-X nanocomposite plates. In the modelling, the b/h, P_{in} and V_{CNT}^{*} are set to 10, 1, and 0.12, respectively.

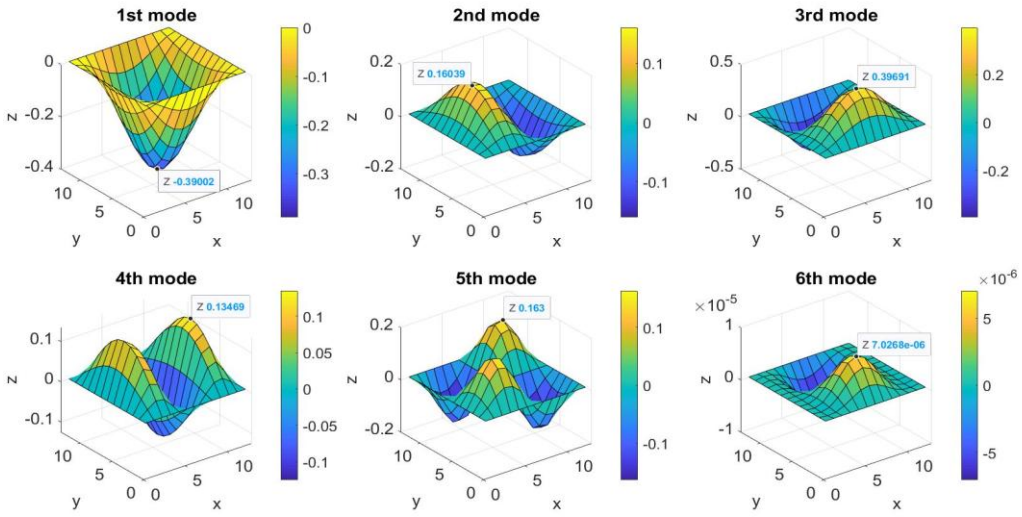

(i) $T = 300K$ and $C = 1\%$

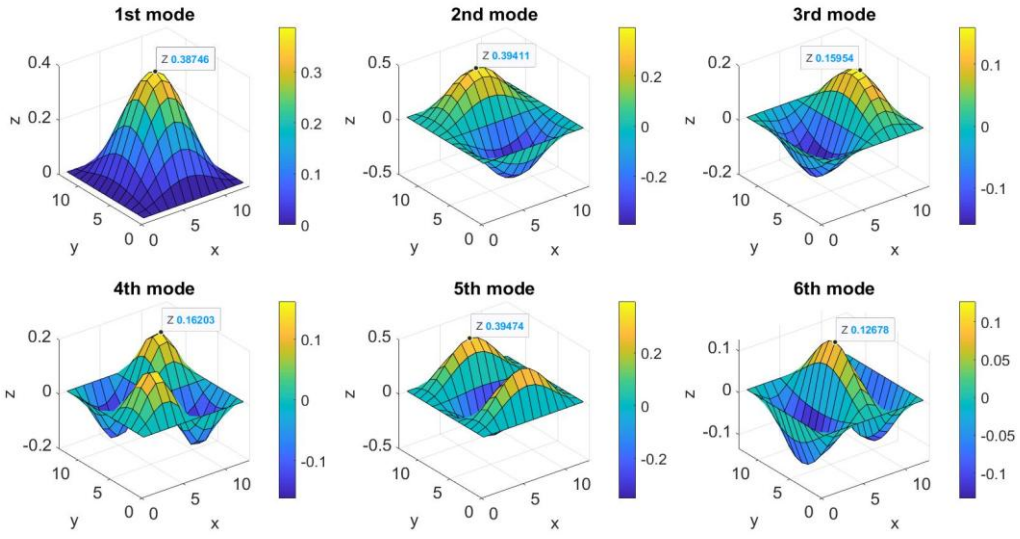

(ii) $T = 400K$ and $C = 1\%$

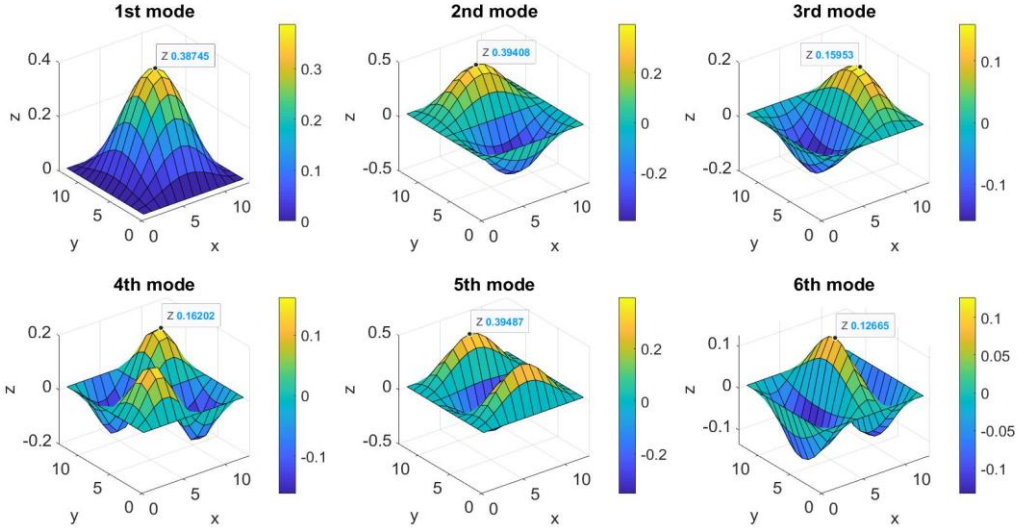

(iii) $T = 400K$ and $C = 3\%$

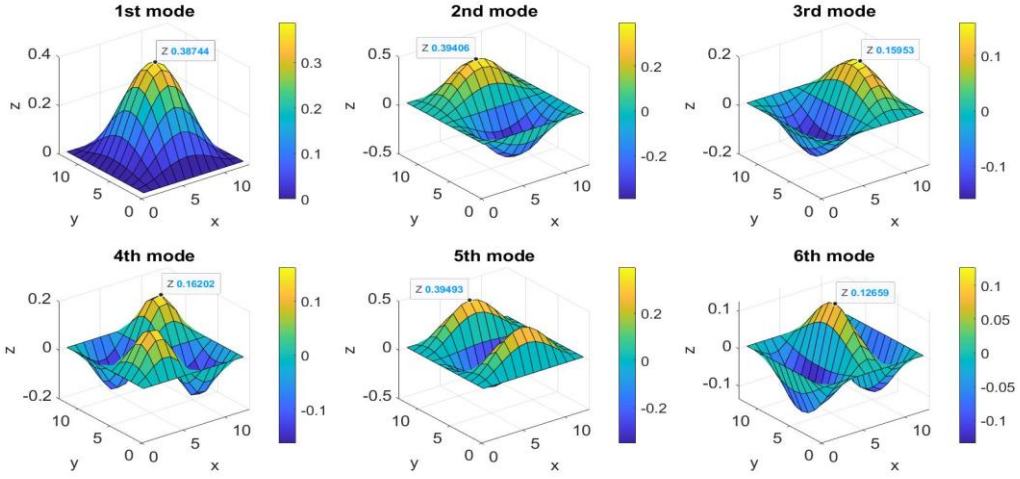

(iv) $T = 400K$ and $C = 4\%$

Figure 5. 6 : First six mode shapes for CCCC square FG-X CNTRC plates under the effects of different hygrothermal environments (a/b = 1, b/h = 10, P_{in} = 1)

5.8 Conclusion

This chapter investigated the free vibration analysis of FG-CNTRC plates in hygrothermal environments using FSDT. The governing equations of the nanocomposite plates in hygrothermal environments have been obtained using Lagrange's equation and solved based on a FEM implemented through a self-developed code. The material properties of the nanocomposite plates (i.e., carbon CNTs and PMMA matrix) were considered to be temperature and moisture-dependent. The current paper studies the influence of varied distribution patterns of CNT reinforcements throughout the plate thickness on the non-dimensional natural frequencies of FG-CNTRC plates. The accuracy of the developed code is verified by comparing the results with ABAQUS and those in the published references. Parametric studies are performed to study the influence of CNT distribution pattern, plate geometry, CNTs volume fraction, boundary conditions, linear and non-linear CNTs distributions, and hygrothermal environments on the free vibrational behavior of FG-CNTRC plates. A review of the most essential highlights is outlined below:

- A consistent decrease in the non-dimensional natural frequencies ($\bar{\omega}$) of the FG-CNTRC plates was observed with increasing temperature and moisture content. This trend suggests a degradation of the overall stiffness within the composite material due to hygrothermal exposure.
- The study revealed a positive correlation between the non-dimensional frequencies and the width-to-thickness ratio (b/h). Conversely, increasing the aspect ratio (a/b) resulted in a gradual decrease in $\bar{\omega}$. This indicates a dependence of the vibrational response on the plate's geometry.
- An increase in the volume fraction of CNTs corresponds to higher natural frequencies. Notably, dispersing more CNTs near the top and bottom surfaces of the plates proved to be the most efficient way to improve stiffness.
- Compared to other boundary configurations, clamped boundary conditions demonstrably yielded the most significant improvements in the mechanical behaviour, as evidenced by the increase in $\bar{\omega}$.
- A unique characteristic was observed for the FG-X distribution pattern. Its natural frequencies exhibited a positive correlation with the P_{in} parameter. Conversely, a decrease in the natural frequencies is noted for FG-O and FG-V plates under similar conditions.

CHAPTER 6: FREE VIBRATION ANALYSIS OF MULTI-LAYERED FG-CNTRC PLATES IN HYGROTHERMAL ENVIRONMENTS

6.1 Introduction

Recent research has demonstrated that laminated structures, such as beams, plates, and shells, offer superior mechanical performance compared to single-layer structures. This has prompted significant interest in the study of laminated composites reinforced with carbon nanotubes (CNTs). The enhanced mechanical properties of CNTs have driven further exploration into the behavior of laminated structures under various conditions.

This chapter investigates the impact of stacking sequences on the vibrational characteristics of laminated composite plates incorporating functionally graded CNT-reinforced composite (FG-CNTRC) layers. The analysis is conducted using the FSDT to model the behavior of these structures. A detailed parametric study is performed to evaluate the impacts of hygrothermal environments, plate geometry, CNTs volume fraction, boundary conditions, CNTs orientation angle, uncertainty in the CNTs distributions, and number of plies constituting the plate thickness on the vibrational behavior of FG-CNTRC laminated plates.

6.2 Comparative studies

This section presents numerical applications performed using the developed finite element code. To assess the accuracy and reliability of the implemented model for laminated plates with various reinforcement orientations, a convergence study is initially carried out. For this purpose, two validation cases are considered, each involving laminated plates composed of a poly(m-phenylenevinylene)-co-[(2,5-dioctoxy-p-phenylene)vinylene] (PmPV) polymer matrix reinforced with (10,10) single-walled carbon nanotubes (SWCNTs). The computational analysis is conducted using the following material and geometric parameters:

$E_m = 2.1GPa$, $v_{12}^m = 0.34$, $\rho^m = 1150kg/m^3$ $E_{11}^{CNT} = 5646.6GPa$, $E_{22}^{CNT} = 7080.0GPa$, $v_{12}^{CNT} = 0.175$, $\rho^{CNT} = 1400kg/m^3$ and $G_{12} = 1944.5GPa$.

In the first study, a simply supported cross-ply square CNTRC laminated plate with a lay-up of $(0°/90°)_2$ is considered. The effects of width-to-thickness ratio (b/h = 10, 20, 50), power-law index (P_{in} = 0, 0.4, 1, 1.4, 1.8), and CNT distribution patterns ([X-X-X-X] and [Λ-Λ-V-V]) on the non-dimensional fundamental frequency are investigated for a constant CNT volume fraction of 0.17. The obtained results are compared with those reported by Chiker et al. [19] in Table 6.1, demonstrating excellent agreement.

The second study focuses on a simply supported CNTRC square laminated plate with two stacking sequences: $(0°/90°)_n$ and $(45°/-45°)_n$, where n = 1, 2, or 4. The width to thickness ratio (b/h) and CNT volume fraction are set to 50 and 0.14, respectively. Table 6.2 presents the calculated results, which exhibit good agreement with those published in Ref. [110].

Table 6.1 Fundamental frequency of cross-ply $(0°/90°)_2$ CNTRC laminated plates with different power-law indexes (V^*_{CNT} = 0.17, and a/b = 1).

b/h	Configurations	P_{in} = 0		P_{in} = 1		P_{in} = 1.4		P_{in} = 1.8	
		Chiker et al. [19]	Present	Chiker et al. [19]	Present	Chiker et al. [19]	Present	Chiker et al. [19]	Present
10	[X-X-X-X]	17.776	17.9560	18.032	18.2105	18.112	18.2914	18.190	18.3705
	[Λ-Λ-V-V]	17.776	17.9560	19.339	19.4908	19.707	19.8533	20.009	20.1517
20	[X-X-X-X]	20.659	20.7535	21.000	21.0955	21.094	21.1897	21.180	21.2757
	[Λ-Λ-V-V]	20.659	20.7535	23.040	23.1338	23.602	23.6960	24.054	24.1484
50	[X-X-X-X]	21.799	21.8159	22.180	22.1964	22.279	22.2957	22.367	22.3838
	[Λ-Λ-V-V]	21.799	21.8159	24.581	24.5984	25.242	25.2598	25.771	25.7891

Table 6.2 Comparisons of the fundamental non-dimensional frequencies of cross-ply $(0°/90°)_n$ and angle- ply $(45°/-45°)_n$ laminated CNTRC plates

Staking sequences	**n**	**FG-O**		**FG-V**		**UD**		**FG-X**	
		Ref. [110]	Present	Ref. [110]	Present	Ref. [110]	Present	Ref. [110]	Present
$(0^\circ/90^\circ)_n$	1	9.874	9.9775	10.876	10.9575	12.395	12.3910	14.396	14.4229
	2	19.354	19.3829	19.484	19.5106	19.726	19.7114	20.032	20.0510
	4	21.036	21.0549	21.065	21.0843	21.142	21.1246	21.193	21.2096
$(45^\circ/-45^\circ)_n$	1	12.996	13.0337	15.388	15.2961	16.631	16.6220	19.600	19.5584
	2	26.536	26.5093	26.694	26.8023	27.005	26.9695	27.481	27.4408
	4	28.859	28.8202	28.908	28.8871	28.961	28.9176	29.077	29.0343

6.3 Free vibrations analysis of FG-CNTRC laminated plates

Consider a CNTRC laminated plate in a Cartesian coordinate system (*x*, *y*, *z*) of homogeneous thickness *h*, length *a* and width *b* (Fig. 6.1). The plate is composed of *n* CNTRC plies, each with uniform thickness *t* and consisting of an even number of layers N_L . The thickness of each individual layer is the same, and equals $\Delta h = t / N_L$. The CNTRC plies consist of PMMA polymer matrix reinforced with armchair (10, 10) single-walled carbon nanotubes.

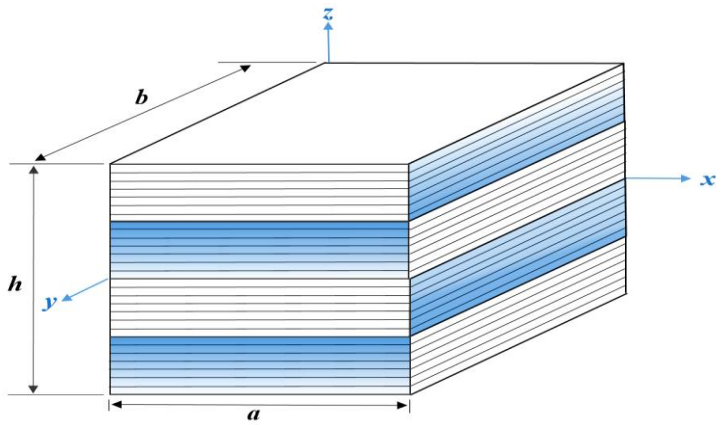

Figure 6.1 : Schematic of CNTRC laminated plate.

Three ply stratification configurations with respect to CNT distribution patterns are proposed: [Λ-Λ-V-V], [V-V-Λ-Λ], and [X-X-X-X], as illustrated in Figure 6.2. Unless otherwise specified, parametric studies are conducted at room temperature (T = 300 K) and P_{in} is equal to 1.

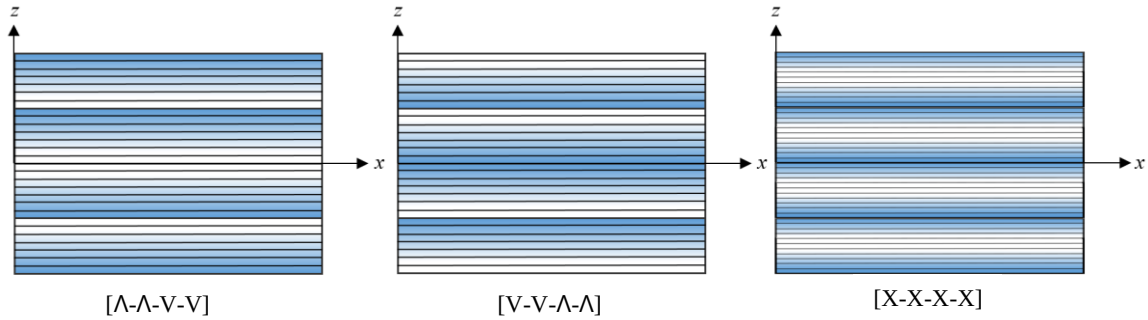

Figure 6.2 : Configuration types of the CNTRC laminated plates

The boundary conditions for a SSSS angle-play laminate are:

$$\begin{cases} u_0 = w_0 = \theta_y = 0 & at \quad x = 0, a \\ v_0 = w_0 = \theta_x = 0 & at \quad y = 0, b \end{cases}$$

The boundary conditions for a SSSS cross-play laminate are:

$$\begin{cases} v_0 = w_0 = \theta_y = 0 & at \quad x = 0, a \\ u_0 = w_0 = \theta_x = 0 & at \quad y = 0, b \end{cases}$$

6.3.1. Effect of width-to-thickness, different moisture environments, plate configurations, and stacking sequences on the natural frequencies

Table 6.3 demonstrates the effects of the side-to-thickness ratio (*b/h* = 10, 20, 50), plate configurations, and moisture concentration (C(%) = 0, 0.5, 1, 1.5, 2, 3, 4) on free vibration of simply supported CNTRC square laminated plates. The results demonstrate a clear correlation between these parameters and the vibrational behavior of the plates. Increasing the side-to-thickness ratio leads to a corresponding increase in the fundamental frequency regardless of the CNTs orientation angle. Conversely, elevated moisture concentrations result in a decrease in frequency due to the degradation of material properties.

Table 6.3 Effect of width-to-thickness ratio, plate configurations, stacking sequences, and moisture rise on the non-dimensional frequency parameter of SSSS laminated plates

			Moisture concentration (%)						
b/h	**Plate configurations**	**Stacking sequences**	**0**	**0.5**	**1**	**1.5**	**2**	**3**	**4**
10	[X-X-X-X]	$(45°/-45°)_2$	15.8546	15.8442	15.8337	15.8233	15.8128	15.7918	15.7707
		$(0°/90°)_2$	13.2158	13.2048	13.1937	13.1827	13.1716	13.1494	13.1271
	[Λ-Λ-V-V]	$(45°/-45°)_2$	16.6612	16.6509	16.6406	16.6303	16.6200	16.5993	16.5785
		$(0°/90°)_2$	14.0848	14.0740	14.0632	14.0524	14.0416	14.0198	13.9980
	[V-V-Λ-Λ]	$(45°/-45°)_2$	14.3756	16.6509	14.3541	14.3433	14.3325	14.3109	14.2892
		$(0°/90°)_2$	11.7486	11.7371	11.7256	11.7140	11.7024	11.6792	11.6558
20	[X-X-X-X]	$(45°/-45°)_2$	20.2347	20.1990	20.1631	20.1272	20.0912	20.0189	19.9462
		$(0°/90°)_2$	15.4850	15.4383	15.3915	15.3446	15.2974	15.2027	15.1072
	[Λ-Λ-V-V]	$(45°/-45°)_2$	21.9799	21.9469	21.9139	21.8808	21.8476	21.7810	21.7141
		$(0°/90°)_2$	16.9184	16.8758	16.8330	16.7900	16.7470	16.6604	16.5733
	[V-V-Λ-Λ]	$(45°/-45°)_2$	17.4227	17.3812	17.3396	17.2979	17.2560	17.1720	17.0874
		$(0°/90°)_2$	13.2790	13.2246	13.1700	13.1151	13.0600	12.9489	12.8367
50	[X-X-X-X]	$(45°/-45°)_2$	22.3083	22.0791	22.2627	22.2398	22.2169	22.1711	22.1251
		$(0°/90°)_2$	16.3721	16.0568	15.7350	15.4063	15.0702	14.3740	13.6416
	[Λ-Λ-V-V]	$(45°/-45°)_2$	24.7056	24.4992	24.6644	24.6439	24.6233	24.5820	24.5407
		$(0°/90°)_2$	18.0877	17.8032	17.5139	17.2197	16.9202	16.3042	15.6633
	[V-V-Λ-Λ]	$(45°/-45°)_2$	18.7048	18.4300	18.6502	18.6228	18.5954	18.5404	18.4853
		$(0°/90°)_2$	13.8336	13.4584	13.0722	12.6741	12.2628	11.3952	10.4548

The specific arrangement of CNTs within the layers, as represented by different plate configurations, also impacts the frequency response. The [Λ-Λ-V-V] configuration consistently exhibits higher frequencies compared to [X-X-X-X] and [V-V-Λ-Λ]. Table 6.3 also reveals that angle-ply $(45°/-45°)_2$ CNTRC laminated plates exhibit higher frequencies

compared to cross-ply $(0°/90°)_2$ laminates, indicating that the specific orientation of CNTs can significantly influence the vibrational behavior of the plates.

6.3.2. Effect of aspect ratio, different moisture environments, plate configurations, and stacking sequences on the natural frequencies

Table 6.4 presents a comprehensive analysis of the dimensionless frequency of simply supported cross-ply and angle-ply CNTRC laminated plates under varying moisture concentrations, aspect ratios, and plate configurations. The results demonstrate a consistent decrease in frequency with increasing moisture concentration, regardless of plate geometry or configuration leading to reduced stiffness. Furthermore, the study highlights the influence of the plate aspect ratio on the frequency response. As the aspect ratio (*a/b*) increases, the dimensionless frequency decreases. This is likely due to the increased flexibility of longer plates, which can vibrate more readily at lower frequencies. However, for cross-ply CNTRC laminated plates with an aspect ratio of 2, the frequency differences between configurations become negligible.

Table 6.4 Effect of aspect ratio, distribution patterns and moisture concentration on the non-dimensional frequency parameter of SSSS CNTRC laminated plates (V^*_{CNT} = 0.12, and *b/h* = 10)

			Moisture concentration (%)						
a/b	**Plate configurations**	**Stacking sequences**	**0**	**0.5**	**1**	**1.5**	**2**	**3**	**4**
1	[X-X-X-X]	$(45°/-45°)_2$	15.8546	15.8442	15.8337	15.8233	15.8128	15.7918	15.7707
		$(0°/90°)_2$	13.2158	13.2048	13.1937	13.1827	13.1716	13.1494	13.1271
	[Λ-Λ-V-V]	$(45°/-45°)_2$	16.6612	16.6509	16.6406	16.6303	16.6200	16.5993	16.5785
		$(0°/90°)_2$	14.0848	14.0740	14.0632	14.0524	14.0416	14.0198	13.9980
	[V-V-Λ-Λ]	$(45°/-45°)_2$	14.3756	16.6509	14.3541	14.3433	14.3325	14.3109	14.2892
		$(0°/90°)_2$	11.7486	11.7371	11.7256	11.7140	11.7024	11.6792	11.6558
1.5	[X-X-X-X]	$(45°/-45°)_2$	14.4393	14.4294	14.4195	14.4095	14.3996	14.3795	14.3594
		$(0°/90°)_2$	15.5313	15.5276	15.5236	15.5194	15.5150	15.5057	15.4956
	[Λ-Λ-V-V]	$(45°/-45°)_2$	14.9737	14.9641	14.9544	14.9447	14.9350	14.9155	14.8959
		$(0°/90°)_2$	16.0189	16.0141	16.0091	16.0040	15.9987	15.9877	15.9763
	[V-V-Λ-Λ]	$(45°/-45°)_2$	13.4554	13.4453	13.4352	13.4250	13.4148	13.3942	13.3734
		$(0°/90°)_2$	14.5789	14.5775	14.5757	14.5735	14.5710	14.5651	14.5582
2	[X-X-X-X]	$(45°/-45°)_2$	10.5376	10.5262	10.5148	10.5034	10.4920	10.4691	10.4461
		$(0°/90°)_2$	8.5897	8.5867	8.5836	8.5805	8.5774	8.5713	8.5651
	[Λ-Λ-V-V]	$(45°/-45°)_2$	11.1732	11.1624	11.1516	11.1408	11.1300	11.1084	11.0866
		$(0°/90°)_2$	8.5899	8.5869	8.5838	8.5807	8.5777	8.5715	8.5653
	[V-V-Λ-Λ]	$(45°/-45°)_2$	9.4584	9.4458	9.4332	9.4206	9.4079	9.3825	9.3570
		$(0°/90°)_2$	8.5424	8.5292	8.5160	8.5027	8.4895	8.4628	8.4360

The impact of plate configuration on frequency is also investigated. The [V-V-Λ-Λ] configuration generally exhibits lower frequencies compared to [Λ-Λ-V-V] and [X-X-X-X]. This can be attributed to the specific arrangement of CNTs within the layers, which affects the overall stiffness and vibration characteristics of the laminate.

6.3.3. Effect of volume fraction, different moisture environments, plate configurations, and stacking sequences on the natural frequencies

Table 6.5 presents a comprehensive analysis of the effects of CNT volume fraction, moisture concentration, and plate configuration on the dimensionless frequency of square SSSS cross-ply and angle-ply CNTRC laminated plates with a *b/h* ratio of 10.

Table 6.5 Effect of CNT volume fraction, plate configurations, stacking sequences, and moisture concentration on the non-dimensional frequency parameter of SSSS CNTRC laminated plates

V^*_{CNT}	Plate configurations	Stacking sequences	Moisture concentration (%)						
			0	0.5	1	1.5	2	3	4
0.12	[X-X-X-X]	$(45°/-45°)_2$	15.8546	15.8442	15.8337	15.8233	15.8128	15.7918	15.7707
		$(0°/90°)_2$	13.2158	13.2048	13.1937	13.1827	13.1716	13.1494	13.1271
	[Λ-Λ-V-V]	$(45°/-45°)_2$	16.6612	16.6509	16.6406	16.6303	16.6200	16.5993	16.5785
		$(0°/90°)_2$	14.0848	14.0740	14.0632	14.0524	14.0416	14.0198	13.9980
	[V-V-Λ-Λ]	$(45°/-45°)_2$	14.3756	16.6509	14.3541	14.3433	14.3325	14.3109	14.2892
		$(0°/90°)_2$	11.7486	11.7371	11.7256	11.7140	11.7024	11.6792	11.6558
0.17	[X-X-X-X]	$(45°/-45°)_2$	19.8423	19.8317	19.8210	19.8104	19.7997	19.7784	19.7569
		$(0°/90°)_2$	16.3984	16.3871	16.3758	16.3644	16.3531	16.3303	16.3075
	[Λ-Λ-V-V]	$(45°/-45°)_2$	20.9359	20.9254	20.9150	20.9045	20.8940	20.8729	20.8518
		$(0°/90°)_2$	17.5319	17.5209	17.5098	17.4988	17.4877	17.4655	17.4433
	[V-V-Λ-Λ]	$(45°/-45°)_2$	17.8688	17.8578	17.8469	17.8359	17.8249	17.8028	17.7806
		$(0°/90°)_2$	14.5112	14.4993	14.4874	14.4755	14.4635	14.4395	14.4154
0.28	[X-X-X-X]	$(45°/-45°)_2$	22.9317	22.9192	22.9067	22.8942	22.8817	22.8565	22.8313
		$(0°/90°)_2$	19.3073	19.2942	19.2811	19.2679	19.2548	19.2284	19.2019
	[Λ-Λ-V-V]	$(45°/-45°)_2$	24.0261	22.9192	24.0014	23.9891	23.9767	23.9519	23.9270
		$(0°/90°)_2$	20.5544	20.5415	20.5287	20.5158	20.5029	20.4771	20.4512
	[V-V-Λ-Λ]	$(45°/-45°)_2$	20.8715	20.8587	20.8459	20.8331	20.8202	20.7945	20.7687
		$(0°/90°)_2$	17.1445	17.1308	17.1172	17.1035	17.0898	17.0623	17.0346

The results reveal that increasing the CNT volume fraction leads to a significant increase in the fundamental non-dimensional frequency, primarily due to the enhanced stiffness provided by the additional CNTs. This effect is observed across all plate configurations and stacking sequences. Conversely, the frequencies decrease with increasing moisture concentration. It is observed that the [Λ-Λ-V-V] configuration exhibits a more pronounced increase in frequency with increasing CNT volume fraction compared to the other

configurations. Moreover, angle-ply $(45°/-45°)_2$ CNTRC laminated plates consistently exhibit higher frequencies compared to cross-ply $(0°/90°)_2$ laminates, further emphasizing the importance of CNT orientation in determining the vibrational behavior of CNTRC plates.

6.3.4. Effect of boundary conditions, different moisture environments, and plate configurations on the natural frequencies

Table 6.6 presents a comprehensive analysis of the combined effects of moisture concentration, plate configuration, and boundary conditions on the fundamental non-dimensional frequencies of $(45°/-45°)_2$ CNTRC laminated plates. The considered boundary condition combinations are illustrated in Figure 6.3, where S denotes simply supported, C clamped, and F free. A square laminated plate with a *b/h* ratio of 10 and a CNT volume fraction of 0.12 is considered.

Table 6.6 Influence of boundary conditions, plate configurations, and moisture concentration on the non-dimensional frequency parameter of laminated CNTRC plate

BCs	Plate configurations	Moisture concentration (%)						
		0	0.5	1	1.5	2	3	4
CCCC	[X-X-X-X]	18.3968	18.3867	18.3766	18.3665	18.3563	18.3360	18.3156
	[Λ-Λ-V-V]	18.9523	18.9423	18.9323	18.9222	18.9122	18.8921	18.8720
	[V-V-Λ-Λ]	17.3168	17.3065	17.2961	17.2857	17.2753	17.2544	17.2335
CSSS	[X-X-X-X]	17.9797	17.9690	17.9582	17.9474	17.9366	17.9150	17.8934
	[Λ-Λ-V-V]	18.5436	18.5331	18.5225	18.5120	18.5014	18.4803	18.4591
	[V-V-Λ-Λ]	16.9128	16.9015	16.8903	16.8790	16.8677	16.8451	16.8225
CSCS	[X-X-X-X]	17.1002	17.0900	17.0797	17.0695	17.0592	17.0386	17.0179
	[Λ-Λ-V-V]	17.7519	17.7417	17.7316	17.7215	17.7113	17.6910	17.6705
	[V-V-Λ-Λ]	15.8853	15.8748	15.8643	15.8537	15.8432	15.8220	15.8008
CCSS	[X-X-X-X]	17.0509	17.0416	17.0323	17.0230	17.0136	16.9949	16.9761
	[Λ-Λ-V-V]	17.6793	17.6700	17.6607	17.6514	17.6421	17.6233	17.6045
	[V-V-Λ-Λ]	15.8784	15.8690	15.8596	15.8502	15.8407	15.8218	15.8028
SSSS	[X-X-X-X]	16.1354	16.1251	16.1147	16.1042	16.0938	16.0729	16.0519
	[Λ-Λ-V-V]	16.8776	16.8673	16.8571	16.8468	16.8365	16.8158	16.7951
	[V-V - Λ-Λ]	14.7941	14.7835	14.7728	14.7621	14.7514	14.7300	14.7085
CCCF	[X-X-X-X]	12.7244	12.7169	12.7093	12.7016	12.6940	12.6786	12.6630
	[Λ-Λ-V-V]	13.2822	13.2748	13.2674	13.2599	13.2524	13.2373	13.2221
	[V-V-Λ-Λ]	11.7250	11.7170	11.7090	11.7009	11.6928	11.6764	11.6599
CFCF	[X-X-X-X]	5.4415	5.4313	5.4210	5.4107	5.4004	5.3797	5.3588
	[Λ-Λ-V-V]	5.8337	5.8243	5.8149	5.8054	5.7959	5.7768	5.7576
	[V-V-Λ-Λ]	4.7999	4.7881	4.7762	4.7643	4.7523	4.7282	4.7038

The outcomes demonstrate that increasing moisture concentration leads to a decrease in frequency. The [Λ-Λ-V-V] configuration consistently exhibits the highest frequencies,

indicating the superior stiffness provided by this arrangement of CNTs. The ranking of frequencies in Table 6.6 from highest to lowest for the different boundary condition combinations further emphasizes the importance of boundary conditions in determining the vibrational behavior of CNTRC plates. As the degree of restraint at the plate edges increases, the fundamental frequency also increases, suggesting that more constrained plates exhibit higher natural frequencies.

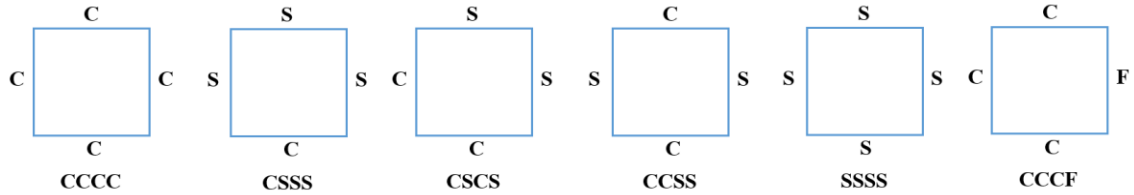

Figure 6.3 : Boundary conditions combinations

6.3.5. Effect of hygrothermal environments, plate configurations, and stacking sequences on the natural frequencies

Table 6.7 investigates the effects of plate configuration, angle-ply stacking sequence, and hygrothermal environments on the fundamental non-dimensional frequencies of simply supported CNTRC square laminated plates.

Table 6.7 Effect of hygrothermal environments, plate configurations, and stacking sequences on the non-dimensional frequency parameter of SSSS CNTRC laminated plates

T	Plate configurations	Stacking sequences	Moisture concentration (%)						
			0	0.5	1	1.5	2	3	4
300K	[X-X-X-X]	$(45°/-45°)_2$	15.8546	15.8442	15.8337	15.8233	15.8128	15.7918	15.7707
		$(0°/90°)_2$	13.2158	13.2048	13.1937	13.1827	13.1716	13.1494	13.1271
	[Λ-Λ-V-V]	$(45°/-45°)_2$	16.6612	16.6509	16.6406	16.6303	16.6200	16.5993	16.5785
		$(0°/90°)_2$	14.0848	14.0740	14.0632	14.0524	14.0416	14.0198	13.9980
	[V-V-Λ-Λ]	$(45°/-45°)_2$	14.3756	16.6509	14.3541	14.3433	14.3325	14.3109	14.2892
		$(0°/90°)_2$	11.7486	11.7371	11.7256	11.7140	11.7024	11.6792	11.6558
350K	[X-X-X-X]	$(45°/-45°)_2$	13.8045	13.7906	13.7767	13.7627	13.7488	13.7208	13.6927
		$(0°/90°)_2$	10.9653	10.9494	10.9335	10.9176	10.9016	10.8695	10.8373
	[Λ-Λ-V-V]	$(45°/-45°)_2$	14.6604	14.6470	14.6336	14.6202	14.6067	14.5797	14.5526
		$(0°/90°)_2$	11.9206	11.9056	11.8906	11.8756	11.8605	11.8302	11.7998
	[V-V-Λ-Λ]	$(45°/-45°)_2$	12.2152	12.2002	12.1852	12.1702	12.1551	12.1248	12.0945
		$(0°/90°)_2$	9.3051	9.2872	9.2693	9.2513	9.2333	9.1970	9.1605
400K	[X-X-X-X]	$(45°/-45°)_2$	10.9155	10.8953	10.8750	10.8546	10.8342	10.7933	10.7521
		$(0°/90°)_2$	7.3905	7.3627	7.3348	7.3068	7.2786	7.2219	7.1646
	[Λ-Λ-V-V]	$(45°/-45°)_2$	11.9162	11.8974	11.8785	11.8595	11.8405	11.8024	11.7641
		$(0°/90°)_2$	8.6634	8.6393	8.6151	8.5908	8.5665	8.5175	8.4681
	[V-V-Λ-Λ]	$(45°/-45°)_2$	8.9709	8.9471	8.9231	8.8991	8.8749	8.8264	8.7776
		$(0°/90°)_2$	4.8133	4.7717	4.7297	4.6873	4.6445	4.5575	4.4687

The results demonstrate that increasing temperature and moisture levels consistently load to a decrease in the fundamental natural frequencies for all plate configurations and stacking sequences, indicating a reduction in stiffness due to the degradation of material properties under hygrothermal conditions. However, angle-ply $(45°/-45°)_2$ CNTRC laminated plates exhibit the highest frequencies. This suggests that the specific arrangement of CNTs across the plies provides superior stiffness. Furthermore, the analysis reveals that plates with the [V-V-Λ-Λ] configuration are more sensitive to changes in temperature and moisture. This is evident from the larger reduction in their fundamental natural frequencies compared to plates with [Λ-Λ-V-V] and [X-X-X-X] configurations. This suggests that the [V-V-Λ-Λ] configuration is more susceptible to environmental changes.

6.3.6. Effect of CNTs orientation angle, different moisture environments, plate configurations, and stacking sequences on the natural frequencies

Figure 6.4 illustrates the effects of CNTs orientation angle (θ = 15°, 30°, 45°, 60°, 75°), two plate configurations ([Λ-Λ-V-V] and [X-X-X-X]), and hygrothermal environments on the non-dimensional frequencies of SSSS $(\theta°/-\theta°)_2$ angle-ply CNTRC laminated plates.

At the reference temperature of 300K, the fundamental frequency curves exhibit a symmetric relationship with respect to the line of θ = 45°. This indicates that the frequency reaches a maximum at a CNT orientation angle of 45° and decreases as the angle deviates from this value. As the temperature increases from 300K to higher values, the symmetry observed at 300K is gradually lost. The frequency continues to increase from θ = 15° to 45°, but the subsequent decrease becomes less pronounced at higher temperatures. At 400K and 440K, the frequency remains relatively steady after reaching its maximum at θ = 45°.

Furthermore, the study reveals the significant impact of hygrothermal environments on the vibrational behavior of the plates. The dimensionless frequencies decrease with increasing moisture concentration and temperature, indicating a reduction in stiffness due to the degradation of material properties. The [Λ-Λ-V-V] configuration consistently offers the

highest frequencies across all scenarios, proving the importance of the specific arrangement of CNTs within the layers and plies.

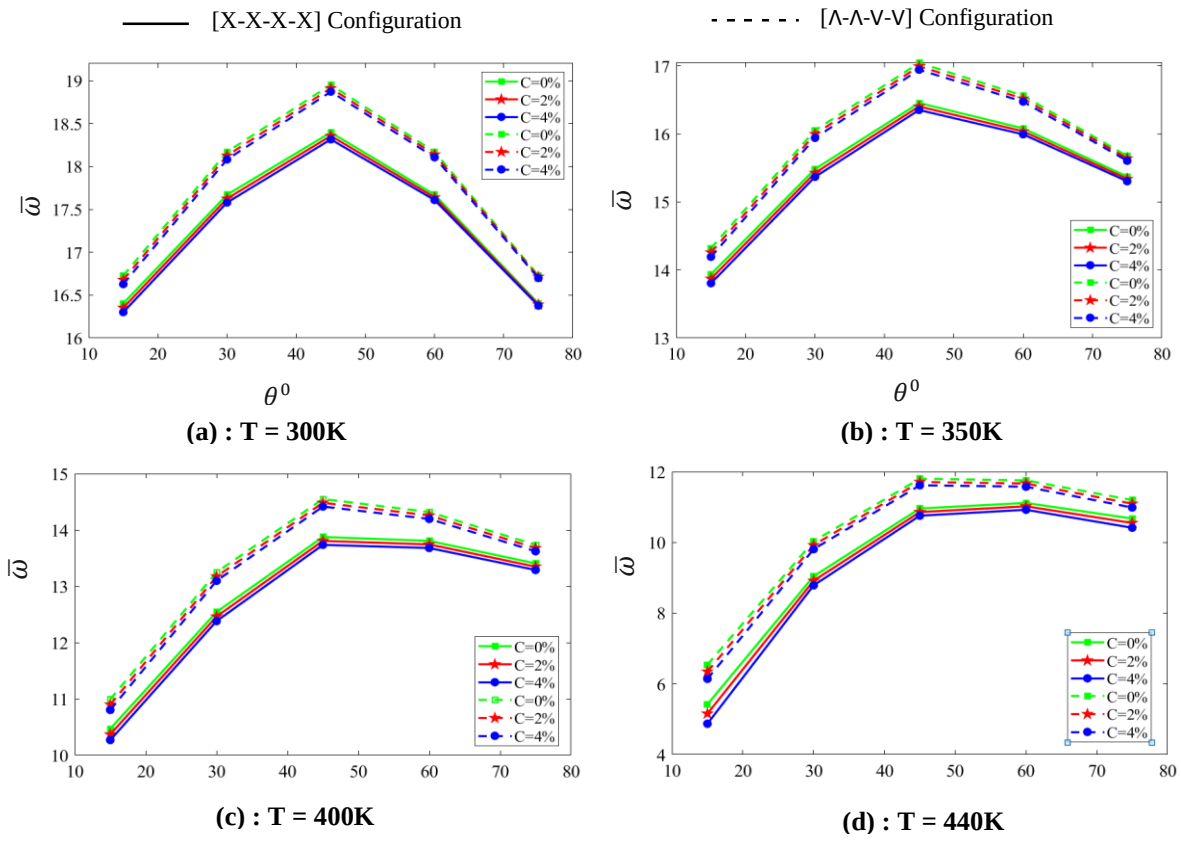

Figure 6.4 : Effects of CNTs orientation angle θ, hygrothermal environments, and plate configurations on the $\bar{\omega}$ parameter of CCCC angle-ply $(\theta°/\text{-}\theta°)_2$ CNTRC laminated plates (a/b = 1, b/h = 10, V^*_{CNT} = 0.12)

6.3.7. Effect of P_{in} parameter, different moisture environments, plate configurations, and stacking sequences on the natural frequencies

Figure 6.5 plots the first non-dimensional frequency versus moisture concentration for various power-law index values of SSSS cross-ply $(0°/90°)_2$ and angle-ply $(45°/\text{-}45°)_2$ CNTRC laminated plates. The outcomes establish a strong relationship between these variables and the vibrational behavior. Increasing the power-law index significantly enhances the fundamental frequency, while increasing moisture concentration leads to a decrease. This effect is observed across both plate configurations and stacking sequences. The influence of plate configuration on the parameter is more pronounced for the [Λ-Λ-V-V] configuration. As the power-law index increases, Fig. 6.5 reveals that the gap between

the first non-dimensional frequencies of plates with [X-X-X-X] configuration is smaller than the gap between the frequencies of plates with [Λ-Λ-V-V] configuration. Furthermore, angle-ply CNTRC laminated plates consistently exhibit higher fundamental dimensionless frequencies compared to cross-ply laminates.

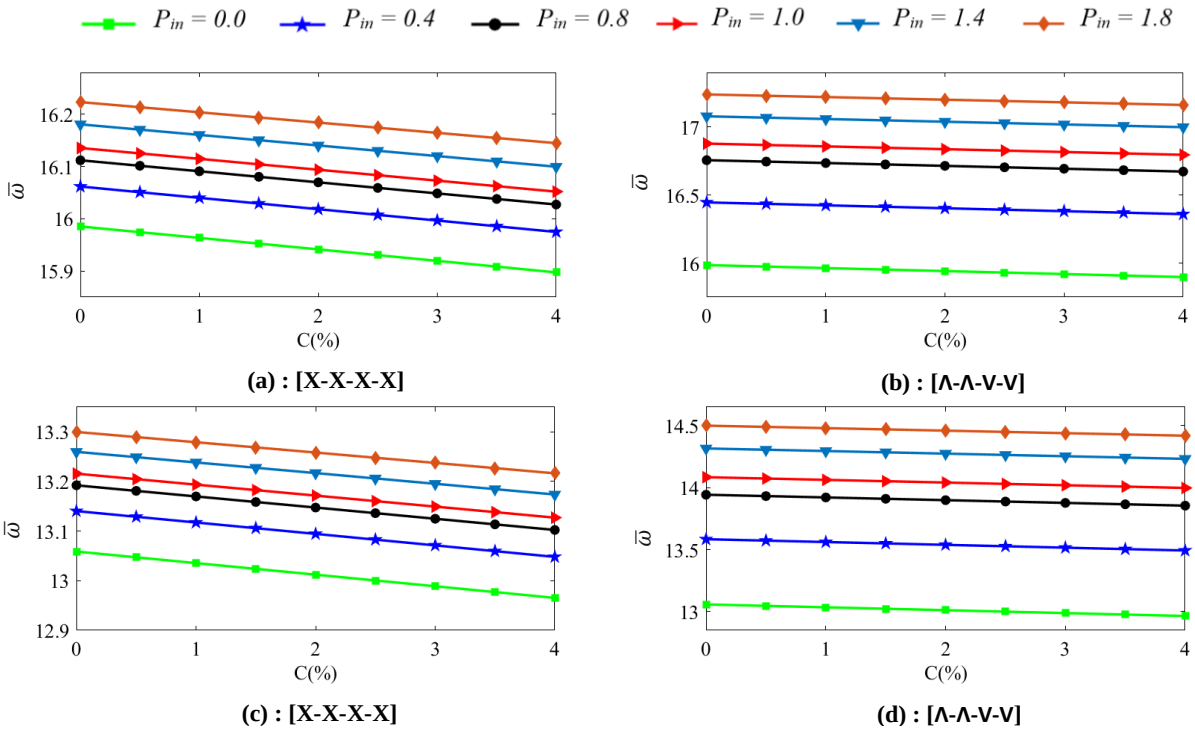

Figure 6.5 : Effects of power-law index (P_{in}), hygrothermal environments, and plate configuration on the $\bar{\omega}$ parameter of SSSS angle-ply ((a) and (b)) and cross-ply ((c) and (d)) CNTRC laminated plates (a/b = 1, b/h = 10, V^*_{CNT} = 0.12)

6.3.8. Effect of number of plies constituting the plate thickness, different moisture environments, plate configurations, and stacking sequences on the natural frequencies

Table 6.8 examines the impact of the number of plies, plate configurations, and moisture rise on the $\bar{\omega}$ parameter of simply supported CNTRC square laminated plates for cross-ply $(0°/90°)_2$ and angle-ply $(45°/-45°)_2$ stacking sequences. The results indicate that increasing the number of plies (n) significantly enhances the parameter $\bar{\omega}$ across all plate configurations. For angle-ply stacking sequence, plates with $[X\text{-}X]_n$ arrangement exhibit the highest $\bar{\omega}$ values when n = 1, while $[V_n\text{-}\Lambda_n]$ plates yield the lowest. However, for n = 2, 4, and 6 in angle-ply stacking sequence, and for all studied n in cross-ply stacking sequence, plates with $[\Lambda_n\text{-}V_n]$ arrangement achieve the highest frequencies under all moisture

conditions. Additionally, the frequencies consistently decrease as moisture concentration increases, reflecting the weakening effect of hygrothermal exposure.

Table 6.8 Influence of number of plies constituting the plate thickness, stacking sequences, distribution patterns and moisture concentration on the non-dimensional frequency parameter of CNTRC plate (b/h = 10, V_{CNT}^{*} = 0.12)

			Moisture concentration (%)						
Stacking sequences	***n***	**Distribution patterns**	**0**	**0.5**	**1**	**1.5**	**2**	**3**	**4**
$(45°/-45°)_n$	**1**	$[X\text{-}X]_n$	13.9352	13.9207	13.9062	13.8917	13.8771	13.8479	13.8186
		$[\Lambda_n\text{-}V_n]$	13.8612	13.8415	13.8216	13.8016	13.7815	13.7408	13.6995
		$[V_n\text{-}\Lambda_n]$	11.5342	11.5084	11.4825	11.4563	11.4299	11.3765	11.3222
	2	$[X\text{-}X]_n$	16.6179	16.6041	16.5904	16.5766	16.5628	16.5352	16.5075
		$[\Lambda_n\text{-}V_n]$	17.3804	17.3669	17.3533	17.3398	17.3262	17.2991	17.2719
		$[V_n\text{-}\Lambda_n]$	15.1791	15.1650	15.1508	15.1367	15.1225	15.0940	15.0655
	4	$[X\text{-}X]_n$	17.0323	17.0187	17.0050	16.9914	16.9777	16.9504	16.9230
		$[\Lambda_n\text{-}V_n]$	17.4077	17.3942	17.3807	17.3671	17.3536	17.3265	17.2993
		$[V_n\text{-}\Lambda_n]$	16.5280	16.5143	16.5005	16.4867	16.4729	16.4453	16.4176
	6	$[X\text{-}X]_n$	17.1023	17.0887	17.0750	17.0614	17.0478	17.0205	16.9931
		$[\Lambda_n\text{-}V_n]$	17.3573	17.3438	17.3303	17.3167	17.3032	17.2760	17.2488
		$[V_n\text{-}\Lambda_n]$	16.7928	16.7791	16.7654	16.7517	16.7380	16.7105	16.6830
$(0°/90°)_n$	**1**	$[X\text{-}X]_n$	11.2720	11.2565	11.2410	11.2254	11.2098	11.1785	11.1471
		$[\Lambda_n\text{-}V_n]$	13.5061	13.4871	13.4681	13.4490	13.4299	13.3917	13.3533
		$[V_n\text{-}\Lambda_n]$	11.0107	10.9876	10.9644	10.9412	10.9179	10.8713	10.8244
	2	$[X\text{-}X]_n$	12.5231	14.0185	14.0040	13.9895	13.9750	13.9459	13.9167
		$[\Lambda_n\text{-}V_n]$	14.9041	14.8899	14.8757	14.8614	14.8472	14.8186	14.7899
		$[V_n\text{-}\Lambda_n]$	14.0330	14.0185	12.4932	12.4782	12.4632	12.4331	12.4029
	4	$[X\text{-}X]_n$	14.5081	14.4938	14.4794	14.4651	14.4507	14.4219	14.3930
		$[\Lambda_n\text{-}V_n]$	14.9439	14.9297	14.9155	14.9012	14.8870	14.8584	14.8298
		$[V_n\text{-}\Lambda_n]$	13.9433	13.9288	13.9143	13.8998	13.8852	13.8561	13.8269
	6	$[X\text{-}X]_n$	14.5898	14.5755	14.5612	14.5469	14.5325	14.5038	14.4749
		$[\Lambda_n\text{-}V_n]$	14.8860	14.8718	14.8576	14.8433	14.8291	14.8005	14.7718
		$[V_n\text{-}\Lambda_n]$	14.2386	14.2242	14.2098	14.1954	14.1809	14.1520	14.1229

6.4 Mode shapes

Furthermore, a fully clamped square CNTRC laminated plate subjected to a specific hygrothermal environment (C = 4% and T = 400K) with a b/h ratio of 10 is considered. The analysis focuses on the dependency of plate mode shapes on CNT configuration, orientation angle θ, and hygrothermal environments, as depicted in Figure 6.6. An angle-ply $(45°/-45°)_2$ stacking sequence and three configurations are chosen for this study.

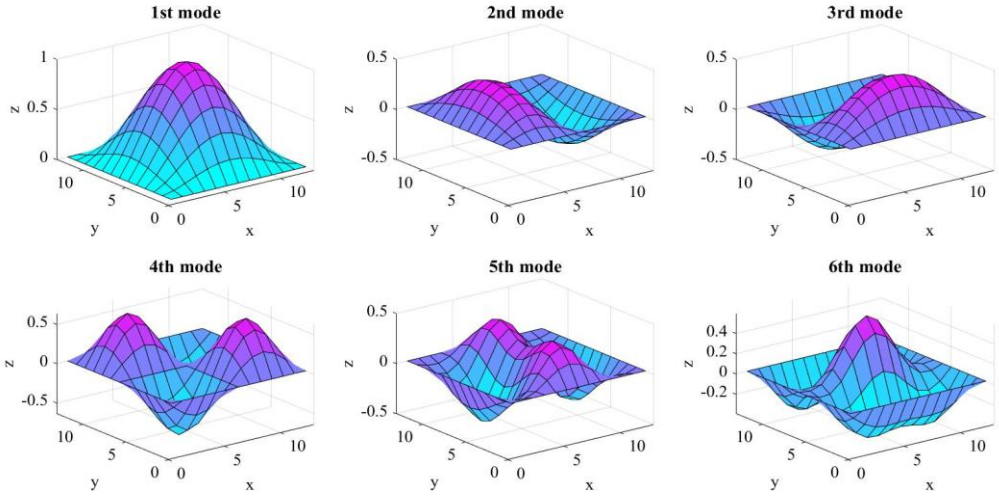

(a) : [X-X-X-X] Configuration

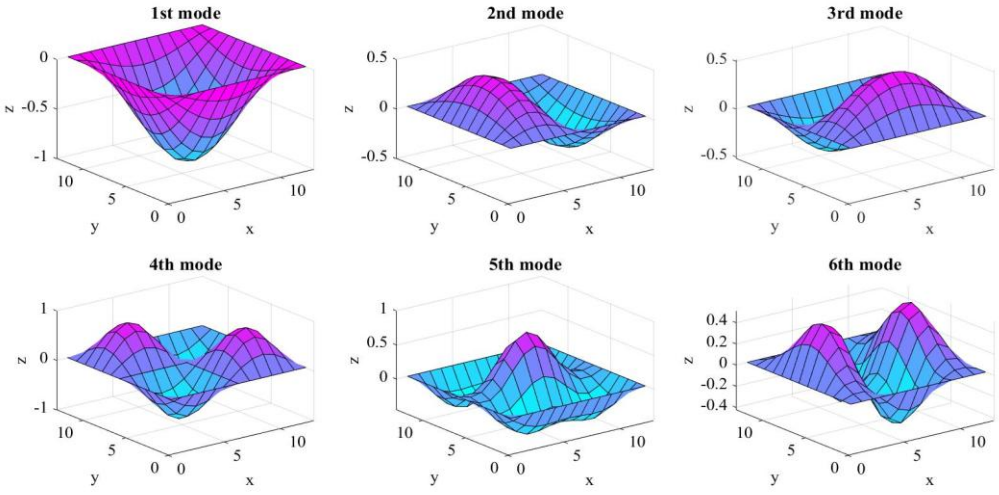

(b) : [Λ-Λ-V-V] Configuration

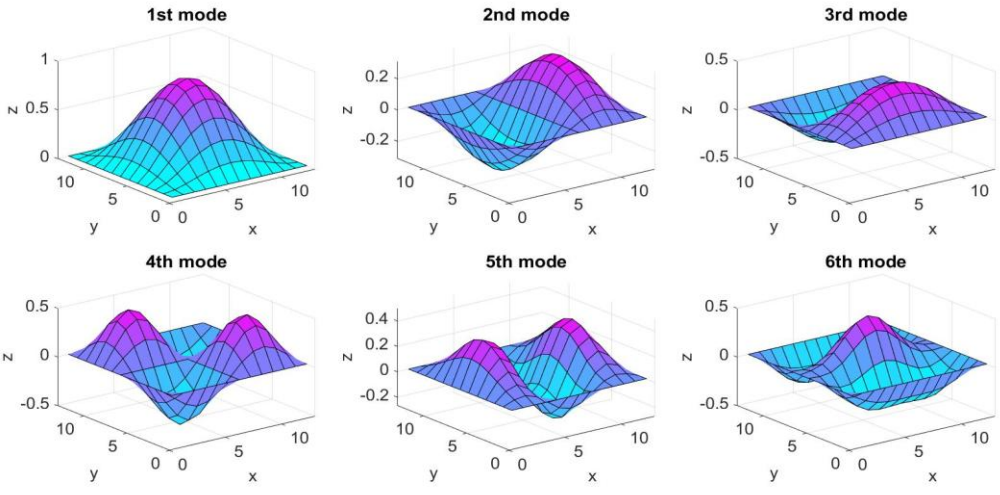

(c) : [V-V-Λ-Λ] Configuration

Figure 6.6 : First six mode shapes for CCCC square CNTRC plates under hygrothermal environment (P_{in} = 1, $(45°/-45°)_2$, C = 4% and T = 400K)

6.5 Conclusion

This chapter focuses on the impact of hygrothermal conditions on the free vibration characteristics of polymeric nanocomposite piecewise laminated plates. The mechanical properties of the plates are considered to be temperature and moisture-dependent. The governing equations are formulated using the FSDT principles and solved through a finite element method implemented via a self-developed computational code, providing the natural frequencies and corresponding mode shapes of the plate. Validation of the numerical results against published literature demonstrates excellent agreement, confirming the accuracy and reliability of the developed code. Comprehensive numerical results are presented in graphical and tabular formats to examine the effect of plate geometry, volume fraction of nanofillers, boundary conditions, CNTs orientation angle, uncertainty in the CNTs distributions and hygrothermal environments on the dimensionless frequencies of the CNTRC laminated plates. The key findings are summarized as follows:

- Elevated temperature and moisture levels reduce the natural frequencies of the laminated plates due to a decrease in their stiffness.
- Angle-ply arrangements exhibit higher natural frequencies compared to cross-ply configurations.
- The natural frequencies increase with higher width-to-thickness ratios and greater volume fractions of nanofillers but decrease with higher length-to-width ratios and elevated temperature or moisture levels.
- This study concludes that the vibrational behavior of ($\theta°/\text{-}\theta°/\theta°/\text{-}\theta°$) angle-ply CNTRC laminated plates is significantly influenced by CNT orientation. At 300K, frequencies are symmetric around θ = 45°, where they reach their maximum, but this symmetry diminishes at elevated temperatures.
- Plates featuring clamped boundaries demonstrate the highest frequencies compared to other configurations.
- Increasing the power-law index enhances the fundamental frequency, while higher moisture concentration reduces it across all plate configurations and stacking sequences. The [Λ-Λ-V-V] configuration demonstrates greater sensitivity to the power-law index, exhibiting a larger frequency gap compared to the [X-X-X-X] configuration.
- Increasing the number of plies enhances the natural frequencies of CNTRC laminated plates, with the [Λ_n-V_n] configuration showing the highest frequencies under various moisture conditions.

GENERAL CONCLUSION

This thesis has focused on the free vibrational behavior of functionally graded carbon nanotube-reinforced composite (FG-CNTRC) plates subjected to hygrothermal environments, with the objective of developing a reliable theoretical and numerical framework capable of capturing the complex interactions between temperature, moisture, and nanoscale reinforcement mechanisms. Using First-Order Shear Deformation Theory (FSDT) and a finite element formulation implemented through a self-developed code, the governing equations of CNTRC plates were derived by incorporating temperature- and moisture-dependent material properties of CNTs and the polymer matrix. The accuracy of the proposed model was confirmed through comparisons with ABAQUS simulations and existing literature.

Across the two main numerical studies (studding the vibrational behavior for FG-CNTRC plates and for laminated FG-CNTRC plates), several important conclusions were reached regarding the influence of environmental conditions, geometrical parameters, reinforcement distribution, and stacking sequences on the dynamic behavior of FG-CNTRC plates:

- **Hygrothermal effects consistently degrade stiffness**, leading to a reduction in the natural frequencies of both single-layer FG-CNTRC plates and multilayer laminated CNTRC configurations. Higher temperatures and moisture concentrations exacerbate this reduction.
- **Plate geometry plays a critical role.** The natural frequencies increase with the width-to-thickness ratio but decrease with the length-to-width ratio, highlighting the sensitivity of vibrational response to plate slenderness and aspect ratio.
- **CNT reinforcement content and distribution strongly enhance performance.** Increasing the CNT volume fraction increases the natural frequencies, with the most efficient improvement obtained when CNTs are concentrated near the plate's outer surfaces. The FG-X pattern, in particular, demonstrated unique behavior, exhibiting a positive correlation between its frequencies and the grading parameter, unlike the FG-O and FG-V patterns.

- **Boundary conditions significantly influence stiffness.** Clamped edges consistently produce the highest natural frequencies, confirming their role in maximizing structural rigidity under dynamic excitation.
- **Lamination sequence and CNT orientation affect dynamic behavior.** Angle-ply CNTRC plates exhibit higher natural frequencies than cross-ply plates. For angle-ply configurations, the natural frequencies display symmetry around $\theta = 45°$ at ambient temperature, a symmetry that gradually diminishes under elevated thermal conditions.
- **Functional grading through power-law distribution introduces an additional degree of control.** Increasing the power-law index enhances the fundamental frequency, although this benefit is reduced as moisture content increases. Layered configurations such as [Λ-Λ-V-V] show greater sensitivity to grading changes compared to uniformly graded [X-X-X-X] configurations.
- **Increasing the number of plies leads to substantial frequency gains**, with the [Λ_n-V_n] configuration achieving the highest natural frequencies across a range of hygrothermal conditions.

Together, these findings confirm that FG-CNTRC plates exhibit complex but highly tunable vibrational characteristics when exposed to combined thermal and moisture loads. The study provides new insights into the interaction between hygrothermal degradation mechanisms and nanoscale reinforcement strategies, demonstrating how CNT volume fraction, distribution pattern, stacking sequence, and lamination architecture can be optimized to compensate for environmental softening effects.

Overall, this work contributes to the ongoing development of high-performance nanocomposite structures for aerospace, marine, and advanced engineering applications, where stability and reliability under harsh environmental conditions are essential. Future research may expand this investigation to nonlinear dynamics, buckling, fatigue assessment, multi-physics coupling, and experimental validation to further enhance the robustness of CNTRC structural models.

REFERENCES

[1] S. Iijima, "Helical microtubules of graphitic carbon," *Nature*, vol. 354, pp. 56–58, 1991.

[2] M. F. Yu, B. S. Files, S. Arepalli, and R. S. Ruoff, "Tensile loading of ropes of single wall carbon nanotubes and their mechanical properties," *Phys. Rev. Lett.*, vol. 84, no. 24, pp. 5552–5555, 2000, doi: 10.1103/PhysRevLett.84.5552.

[3] M. M. J. Treacy, T. W. Ebbesen, and J. M. Gibson, "Exceptionally high Young's modulus observed for individual carbon nanotubes," *Nature*, vol. 381, no. 6584. pp. 678–680, 1996. doi: 10.1038/381678a0.

[4] W. Jiang, G. Ding, and H. Peng, "Measurement and model on thermal conductivities of carbon nanotube nanorefrigerants," *Int. J. Therm. Sci.*, vol. 48, no. 6, pp. 1108–1115, 2009, doi: 10.1016/j.ijthermalsci.2008.11.012.

[5] R. Zhu, E. Pan, and A. K. Roy, "Molecular dynamics study of the stress – strain behavior of carbon-nanotube reinforced Epon 862 composites," *Mater. Sci. Eng. A*, vol. 447, pp. 51–57, 2007, doi: 10.1016/j.msea.2006.10.054.

[6] D. Qian, E. C. Dickey, R. Andrews, and T. Rantell, "Load transfer and deformation mechanisms in carbon nanotube-polystyrene composites," *Appl. Phys. Lett.*, vol. 76, no. 20, pp. 2868–2870, 2000, doi: 10.1063/1.126500.

[7] Erik T Thostenson and Tsu-Wei Chou, "On the elastic properties of carbon nanotube-based composites: modelling and characterization," *J. Phys. D. Appl. Phys.*, vol. 36, no. 11, pp. 573–582, 2003, doi: 10.1016/S0021-9290(03)00188-X.

[8] P. M. Ajayan, L. S. Schadler, and P. V Braun, *Nanocomposite Science and Technology Nanocomposite*. 2003.

[9] F. H. Gojny, M. H. G. Wichmann, U. Köpke, B. Fiedler, and K. Schulte, "Carbon nanotube-reinforced epoxy-composites: Enhanced stiffness and fracture toughness at low nanotube content," *Compos. Sci. Technol.*, vol. 64, no. 15 SPEC. ISS., pp. 2363–2371, 2004, doi: 10.1016/j.compscitech.2004.04.002.

[10] H. S. Shen, "Nonlinear bending of functionally graded carbon nanotube-reinforced composite plates in thermal environments," *Compos. Struct.*, vol. 91, no. 1, pp. 9–19, 2009, doi: 10.1016/j.compstruct.2009.04.026.

[11] M. A. Rafiee, J. Rafiee, Z. Wang, H. Song, Z. Z. Yu, and N. Koratkar, "Enhanced mechanical properties of nanocomposites at low graphene content," *ACS Nano*, vol. 3, no. 12, pp. 3884–3890, 2009, doi: 10.1021/nn9010472.

[12] C. Li and T. W. Chou, "Elastic moduli of multi-walled carbon nanotubes and the effect of van der Waals forces," *Compos. Sci. Technol.*, vol. 63, no. 11, pp. 1517–1524, 2003, doi: 10.1016/S0266-3538(03)00072-1.

[13] S. J. V. Frankland, V. M. Harik, G. M. Odegard, D. W. Brenner, and T. S. Gates, "The stress-strain behavior of polymer-nanotube composites from molecular dynamics simulation," *Compos. Sci. Technol.*, vol. 63, no. 11, pp. 1655–1661, 2003, doi: 10.1016/S0266-3538(03)00059-9.

[14] H. Shen, “Nonlinear bending of functionally graded carbon nanotube-reinforced composite plates in thermal environments,” *Compos. Struct.*, vol. 91, no. 1, pp. 9–19, 2009, doi: 10.1016/j.compstruct.2009.04.026.

[15] G. Tefera, S. Adali, and G. Bright, “file:///C:/Users/dell/Downloads/Predicting-Processing-Induced-Residual-Stresses-in-Carbon-Fiber–Thermoplastic-Micro-Composites.pdf,” *Polym. Polym. Compos.*, vol. 30, p. 09673911221125072, 2022, doi: 10.1177/09673911221125072.

[16] D. D. L. Chung, “Thermal analysis of carbon fiber polymer-matrix composites by electrical resistance measurement,” *Thermochim. Acta*, vol. 364, no. 1–2, pp. 121–132, 2000, doi: 10.1016/S0040-6031(00)00631-6.

[17] O. Matvienko, O. Daneyko, T. Kovalevskaya, A. Khrustalyov, I. Zhukov, and A. Vorozhtsov, “Investigation of stresses induced due to the mismatch of the coefficients of thermal expansion of the matrix and the strengthening particle in aluminum-based composites,” *Metals (Basel).*, vol. 11, no. 2, pp. 1–20, 2021, doi: 10.3390/met11020279.

[18] T. H. Quoc, T. M. Tu, and V. Van Tham, “Free Vibration Analysis of Smart Laminated Functionally Graded CNT Reinforced Composite Plates via New Four - Variable Refined Plate Theory,” *Materials (Basel).*, pp. 1–22, 2019, doi: 10.3390/ma12223675.

[19] Y. Chiker, M. Bachene, B. Attaf, A. Hafaifa, and M. Guemana, “Uncertainty influence of nanofiller dispersibilities on the free vibration behavior of multi-layered functionally graded carbon nanotube-reinforced composite laminated plates,” *Acta Mech.*, vol. 234, no. 4, pp. 1687–1711, 2023, doi: 10.1007/s00707-022-03438-6.

[20] T. Dey and T. Bandyopadhyay, “Free Vibration Response of Porous FGM Plates Using Finite Element Analysis in Thermal Environment,” *J. Vib. Eng. Technol.*, 2023, [Online]. Available: https://doi.org/10.1007/s42417-023-01139-5

[21] P. Zhu, Z. X. Lei, and K. M. Liew, “Static and free vibration analyses of carbon nanotube-reinforced composite plates using finite element method with first order shear deformation plate theory,” *Compos. Struct.*, vol. 94, no. 4, pp. 1450–1460, 2012, doi: 10.1016/j.compstruct.2011.11.010.

[22] N. D. Duc, “New approach to investigate nonlinear dynamic response and vibration of imperfect functionally graded carbon nanotube reinforced composite double curved shallow shells subjected to blast load and temperature,” *Aerosp. Sci. Technol.*, vol. 1, pp. 1–13, 2017, doi: 10.1016/j.ast.2017.09.031.

[23] R. Ansari, R. Hassani, R. Gholami, and H. Rouhi, “Thermal postbuckling analysis of FG-CNTRC plates with various shapes and temperature-dependent properties using the VDQ-FEM technique,” *Aerosp. Sci. Technol.*, vol. 106, p. 106078, 2020, doi: 10.1016/j.ast.2020.106078.

[24] N. J. Kanu and A. Lal, “Post buckling responses of carbon nanotubes’ fiber reinforced and nanoclay modified polymer matrix hybrid composite plate under in-plane buckling load using the higher order shear deformation theory,” *Mech. Based Des. Struct. Mach.*, 2022, doi: https://doi.org/10.1080/15397734.2022.2126985.

[25] A. I. Journal, A. A. Daikh, A. Bachiri, M. Sid, and A. Houari, “Size dependent free vibration and buckling of multilayered carbon nanotubes reinforced composite

nanoplates in thermal environment," *Mech. Based Des. Struct. Mach.*, vol. 0, no. 0, pp. 1–29, 2020, doi: 10.1080/15397734.2020.1752232.

[26] J. Mao and W. Zhang, "Buckling and post-buckling analyses of functionally graded graphene reinforced piezoelectric plate subjected to electric potential and axial forces," *Compos. Struct.*, vol. 216, no. February, pp. 392–405, 2019, doi: 10.1016/j.compstruct.2019.02.095.

[27] M. Di Sciuva and M. Sorrenti, "Bending , free vibration and buckling of functionally graded carbon nanotube-reinforced sandwich plates , using the extended Refined Zigzag Theory," *Compos. Struct.*, vol. 227, no. April, p. 111324, 2019, doi: 10.1016/j.compstruct.2019.111324.

[28] V. N. Van Do and C. Lee, "Nonlinear bending analysis of carbon nanotube-reinforced composite plates in combined thermal and mechanical," *Acta Mech.*, vol. 233, no. 8, pp. 3365–3391, 2022, doi: 10.1007/s00707-022-03268-6.

[29] A. Wang, H. Chen, Y. Hao, and W. Zhang, "Vibration and bending behavior of functionally graded nanocomposite doubly-curved shallow shells reinforced by graphene nanoplatelets," *Results Phys.*, vol. 9, pp. 550–559, 2018, doi: 10.1016/j.rinp.2018.02.062.

[30] K. Mehar, S. K. Panda, A. Dehengia, and V. R. Kar, "Vibration analysis of functionally graded carbon nanotube reinforced composite plate in thermal environment," *J. Sandw. Struct. Mater.*, 2015, doi: 10.1177/1099636215613324.

[31] S. Kamarian and M. Bodaghi, "Thermal buckling analysis of sandwich plates with soft core and CNT composite face sheets," *J. Sandw. Struct. Mater.*, 2020, doi: 10.1177/1099636220935557.

[32] K. Mehar, S. K. Panda, and B. K. Patle, "Stress , Deflection , and Frequency Analysis of CNT Reinforced Graded Sandwich Plate under Uniform and Linear Thermal Environment : A Finite Element Approach," *Polym. Compos.*, pp. 1–18, 2018, doi: 10.1002/pc.24409.

[33] Y. Z. Yüksel and Ş. D. Akbaş, "Hygrothermal stress analysis of laminated composite porous plates Hygrothermal stress analysis of laminated composite porous plates," *Struct. Eng. Mech.*, no. October, 2021, doi: 10.12989/sem.2021.80.1.001.

[34] A. Dogan, "Dynamic response of laminated functionally graded carbon nanotube-reinforced composite viscoelastic plates," *Mech. Based Des. Struct. Mach.*, 2023, doi: https://doi.org/10.1080/15397734.2023.2258183.

[35] Y. Kiani, "Free Vibration of FG-CNT Reinforced Composite Spherical Shell Panels using Gram-Schmidt Shape Functions A novel class of composites known as functionally graded carbon nanotube composites," *Compos. Struct.*, 2016, doi: 10.1016/j.compstruct.2016.09.079.

[36] H. Li *et al.*, "Nonlinear vibration characteristics of elastically supported FRP cylindrical shells under temperature gradient conditions: Theoretical and experimental studies," *Mech. Based Des. Struct. Mach.*, 2023, doi: https://doi.org/10.1080/15397734.2023.2255264.

[37] N. D. Dat, N. D. Khoa, P. D. Nguyen, and N. D. Duc, "An analytical solution for

nonlinear dynamic response and vibration of FG-CNT reinforced nanocomposite elliptical cylindrical shells resting on elastic foundations," *Math. Methods Appl. Sci.*, no. August, pp. 1–20, 2019, doi: 10.1002/zamm.201800238.

[38] M. Rout and S. S. Hota, "Geometrically nonlinear free vibration of CNTs reinforced sandwich conoidal shell in thermal environment," *Acta Mech.*, vol. 234, no. 6, pp. 2677–2694, 2023, doi: 10.1007/s00707-023-03508-3.

[39] Y. Kiani, "Thermal buckling of temperature-dependent FG- CNT-reinforced composite skew plates," *J. Therm. Stress.*, vol. 0, no. 0, pp. 1–19, 2017, doi: 10.1080/01495739.2017.1336742.

[40] F. H. H. A. M. Mohammed Sobhy, "Magnetic Control of Vibrational Behavior of Smart FG Sandwich Plates with Honeycomb Core via a Quasi-3D Plate Theory," *Adv. Eng. Mater.*, vol. 25, no. 13, 2023.

[41] J. F. Wang, S. H. Cao, and W. Zhang, "Thermal vibration and buckling analysis of functionally graded carbon nanotube reinforced composite quadrilateral plate," *Eur. J. Mech. / A Solids*, vol. 85, no. July 2020, 2021, doi: https://doi.org/10.1016/j.euromechsol.2020.104105.

[42] S. Dutton, D. Kelly, and A. Baker, *Composite Materials for Aircraft Structures, Second Edition*. 2004.

[43] D. Hull and T. W. Clyne, *An Introduction to Composite Materials*, 2nd ed. in Cambridge Solid State Science Series. Cambridge University Press, 1996.

[44] Erik T. Thostensona, Z. Renb, and T.-W. Chou, "Advances in the science and technology of carbon nanotubes and their composites: a review," *Mater. Today Proc.*, vol. 61, pp. 1899–1912, 2001, doi: 10.1016/j.matpr.2018.03.038.

[45] M. H. Al-Saleh and U. Sundararaj, "A review of vapor grown carbon nanofiber/polymer conductive composites," *Carbon N. Y.*, vol. 47, no. 1, pp. 2–22, 2009, doi: https://doi.org/10.1016/j.carbon.2008.09.039.

[46] B. Uymaz and G. Uymaz, "Three-Dimensional Thermal Vibration of CFFF Functionally Graded Carbon Nanotube-Reinforced Composite Plates," *J. Vib. Eng. Technol.*, 2023, [Online]. Available: https://doi.org/10.1007/s42417-023-00957-x

[47] D. Qian, Wagner, , Gregory J, L. W. Kam, Y. Min-Feng, and R. R. S, "Mechanics of carbon nanotubes," *Appl. Mech. Rev.*, vol. 55, no. 6, pp. 495–533, 2002, doi: 10.1115/1.1490129.

[48] H. Khov, W. L. Li, and R. F. Gibson, "An accurate solution method for the static and dynamic deflections of orthotropic plates with general boundary conditions," *Compos. Struct.*, vol. 90, no. 4, pp. 474–481, 2009, doi: https://doi.org/10.1016/j.compstruct.2009.04.020.

[49] F. Korkees, "Moisture absorption behavior and diffusion characteristics of continuous carbon fiber reinforced epoxy composites: a review," *Polym. Technol. Mater.*, vol. 62, no. 14, pp. 1789–1822, 2023, doi: 10.1080/25740881.2023.2234461.

[50] G. S. Springer, A. Arbor, B. A. Sanders, and R. W. Tung, "Environmental Effects on Glass Fiber Reinforced Polyester and Vinylester Composites Manufacturing Development General Motors Technical Center," *J. Reinf. Plast. Compos.*, vol. 5,

no. 3, pp. 216–235, 1986.

[51] C.-H. Shen and G. S. Springer, “Moisture Absorption and Desorption of Composite Materials,” *J. Compos. Mater.*, vol. 10, no. 1, pp. 2–20, 1976, doi: 10.1177/002199837601000101.

[52] G. Viana, M. Costa, M. D. Banea, and L. F. M. da Silva, “A review on the temperature and moisture degradation of adhesive joints,” *Proc. Inst. Mech. Eng. Part L J. Mater. Des. Appl.*, vol. 231, no. 5, pp. 488–501, 2017, doi: 10.1177/1464420716671503.

[53] W. Xu, M. M. Thwe, C. Shearwood, and K. Liao, “Effects of carbon nanotube reinforcement on moisture diffusion and mechanical degradation in polymer composites,” *Compos. Sci. Technol.*, vol. 68, no. 6, pp. 1489–1494, 2008.

[54] D. F. Adams and A. K. Miller, “Hygrothermal Microstresses in a Unidirectional Composite Exhibiting Inelastic Material Behavior,” *J. Compos. Mater.*, 1977, doi: 10.1177/002199837701100304.

[55] D. E. Bowles and S. S. Tompkins, “Prediction of Coefficients of Thermal Expansion for Unidirectional Composites,” *J. Compos. Mater.*, 1989, doi: 10.1177/002199838902300405.

[56] B. F. Boukhoulda and K. Madani, “The effect of fiber orientation angle in composite materials on moisture absorption and material degradation after hygrothermal ageing,” *Compos. Struct.*, vol. 74, pp. 406–418, 2006, doi: 10.1016/j.compstruct.2005.04.032.

[57] R. Inala, “Influence of Hygrothermal Environment and FG Material on Natural Frequency and Parametric Instability of Plates,” *Mech. Adv. Compos. Struct.*, no. December, 2020, doi: 10.22075/MACS.2019.17822.1207.

[58] M. W. Zaitoun, A. Chikh, and A. Tounsi, “Influence of the visco-Pasternak foundation parameters on the buckling behavior of a sandwich functional graded ceramic – metal plate in a hygrothermal environment,” *Thin-Walled Struct.*, vol. 170, no. September 2021, p. 108549, 2022, doi: 10.1016/j.tws.2021.108549.

[59] M. W. Zaitoun *et al.*, “An efficient computational model for vibration behavior of a functionally graded sandwich plate in a hygrothermal environment with viscoelastic foundation effects,” *Eng. Comput.*, vol. 39, no. 2, pp. 1127–1141, 2023, doi: 10.1007/s00366-021-01498-1.

[60] E. Arshid, M. Khorasani, Z. Soleimani, J. Saeed, and A. Abdelouahed, “Porosity - dependent vibration analysis of FG microplates embedded by polymeric nanocomposite patches considering hygrothermal effect via an innovative plate theory,” *Eng. Comput.*, no. 0123456789, 2021, doi: 10.1007/s00366-021-01382-y.

[61] V. Kallannavar, S. Kattimani, and H. Ramesh, “Influence of Temperature and Moisture on Free Vibration Behavior of Skew Laminated Composite Sandwich Panels with CNTRC Core,” *Int. J. Struct. Stab. Dyn.*, vol. 22, no. 8, pp. 1–33, 2022, doi: 10.1142/S0219455422500833.

[62] C. Zhang *et al.*, “Vibration analysis of a sandwich cylindrical shell in hygrothermal environment,” *De Gruyter*, pp. 414–430, 2021.

[63] H. Bisheh, N. Wu, and T. Rabczuk, “Thin-Walled Structures Free vibration analysis

of smart laminated carbon nanotube-reinforced composite cylindrical shells with various boundary conditions in hygrothermal environments," *Thin-Walled Struct.*, no. June, p. 106500, 2019, doi: 10.1016/j.tws.2019.106500.

[64] M. S. H. Al-Furjan, B. Alzahrani, L. Shan, M. Habibi, and D. W. Jung, "Nonlinear forced vibrations of nanocomposite-reinforced viscoelastic thick annular system under hygrothermal environment," *Mech. Based Des. Struct. Mach.*, vol. 50, no. 11, pp. 4021–4047, 2020, doi: 10.1080/15397734.2020.1824795.

[65] K. Foroutan, E. Carrera, and H. Ahmadi, "Nonlinear hygrothermal vibration and buckling analysis of imperfect FG-CNTRC cylindrical panels embedded in viscoelastic foundations," *Eur. J. Mech. / A Solids*, vol. 85, no. April 2020, p. 104107, 2021, doi: 10.1016/j.euromechsol.2020.104107.

[66] R. Penna, G. Lovisi, and L. Feo, "Dynamic Response of Multilayered Polymer Functionally Graded Carbon Nanotube Reinforced Composite (FG-CNTRC) Nano-Beams in Hygro-Thermal Environment," *Polymers (Basel).*, 2021.

[67] H. D. Chalak, A. M. Zenkour, and A. Garg, "Free vibration and modal stress analysis of FG- CNTRC beams under hygrothermal conditions using zigzag theory," *Mech. Based Des. Struct. Mach.*, vol. 0, no. 0, pp. 1–22, 2021, doi: 10.1080/15397734.2021.1977659.

[68] S. S. Patnaik and T. Roy, "Vibration characteristics and damping properties of functionally graded carbon nanotubes reinforced hybrid composite skewed shell structures under hygrothermal conditions," *J. Vib. Control*, vol. 27, no. 21–22, pp. 2494–2512, 2021, doi: 10.1177/1077546320961718.

[69] A. M. Alsubaie *et al.*, "Porosity-dependent vibration investigation of functionally graded carbon nanotube-reinforced composite beam," *Comput. Concr.*, vol. 32, no. 1, pp. 75–85.

[70] Y. Zhai, S. Li, and X. Zhang, "Thermomechanical buckling and vibration of composite sandwich doubly curved shells with carbon nanotube-reinforced face layers," *Polym. Compos.*, vol. 45, no. 18, pp. 16692–16705, 2024, doi: https://doi.org/10.1002/pc.28921.

[71] S. S. Patnaik, "FE Modelling of Vibrational Parameters of Viscoelastic CNT–CFRP Hybrid Spherical Shell Structures," *J. Vib. Eng. Technol.*, vol. 12, pp. 5021–5039, 2024, [Online]. Available: https://doi.org/10.1007/s42417-023-01222-x

[72] B. P. Patel, M. Ganapathi, and D. P. Makhecha, "Hygrothermal effects on the structural behaviour of thick composite laminates using higher-order theory," *Compos. Struct.*, vol. 56, no. 1, pp. 25–34, 2002, doi: 10.1016/S0263-8223(01)00182-9.

[73] M. K. Rath and S. K. Sahu, "Vibration of woven fiber laminated composite plates in hygrothermal environment," *JVC/Journal Vib. Control*, vol. 18, no. 13, pp. 1957–1970, 2012, doi: 10.1177/1077546311428638.

[74] M. Bouazza and A. M. Zenkour, "Free vibration characteristics of multilayered composite plates in a hygrothermal environment via the refined hyperbolic theory," *Eur. Phys. J. Plus*, vol. 133, no. 6, p. 217, 2018, doi: 10.1140/epjp/i2018-12050-x.

[75] A. Abdelmalek, M. Bouazza, M. Zidour, and N. Benseddiq, "Hygrothermal Effects

on the Free Vibration Behavior of Composite Plate Using nth-Order Shear Deformation Theory: a Micromechanical Approach," *Iran. J. Sci. Technol. - Trans. Mech. Eng.*, vol. 43, pp. 61–73, 2019, doi: 10.1007/s40997-017-0140-y.

[76] H. Bisheh and Ö. Civalek, "Vibration of smart laminated carbon nanotube-reinforced composite cylindrical panels on elastic foundations in hygrothermal environments," *Thin-Walled Struct.*, vol. 155, no. May, p. 106945, 2020, doi: 10.1016/j.tws.2020.106945.

[77] L. H. Carvalho, E. L. Canedo, S. R. Farias Neto, A. G. B. de Lima, and C. J. Silva, "Moisture Transport Process in Vegetable Fiber Composites: Theory and Analysis for Technological Applications," in *Industrial and Technological Applications of Transport in Porous Materials*, J. M. P. Q. Delgado, Ed., Berlin, Heidelberg: Springer Berlin Heidelberg, 2013, pp. 37–62. doi: 10.1007/978-3-642-37469-2_2.

[78] M. K. Egbo, "A fundamental review on composite materials and some of their applications in biomedical engineering," *J. King Saud Univ. - Eng. Sci.*, vol. 33, no. 8, pp. 557–568, 2021, doi: 10.1016/j.jksues.2020.07.007.

[79] J. P. Greene, "12 - Polymer Composites," in *Automotive Plastics and Composites*, J. P. Greene, Ed., in Plastics Design Library. , William Andrew Publishing, 2021, pp. 191–222. doi: https://doi.org/10.1016/B978-0-12-818008-2.00007-6.

[80] J. P. Davim, *Metal matrix composites*. 2012. doi: 10.31399/asm.tb.scm.t52870537.

[81] P. Ladevèze, E. Baranger, M. Genet, and C. Cluzel, *Damage and Lifetime Modeling for Structure Computations*, vol. 9781118231, no. October. 2014. doi: 10.1002/9781118832998.ch17.

[82] K. K. Kar, J. K. P. Sravendra, and R. Editors, *Handbook of Polymer Nanocomposites. Processing, Performance and Application*, vol. B. 2015.

[83] A. Aligayev, F. Raziq, U. Jabbarli, N. Rzayev, and L. Qiao, "Chapter 17 - Morphology and topography of nanotubes," in *Graphene, Nanotubes and Quantum Dots-Based Nanotechnology*, Y. Al-Douri, Ed., in Woodhead Publishing Series in Electronic and Optical Materials. , Woodhead Publishing, 2022, pp. 355–420. doi: https://doi.org/10.1016/B978-0-323-85457-3.00019-0.

[84] M. Niino and S. Maeda, "Recent Development Status of Functionally Gradient Materials," *ISIJ Int.*, vol. 30, no. 9, pp. 699–703, 1990, doi: 10.2355/isijinternational.30.699.

[85] Y. Hu, W.-M. Ji, and L.-W. Zhang, "Water-induced damage revolution of the carbon nanotube reinforced poly (methyl methacrylate) composites," *Compos. Part A Appl. Sci. Manuf.*, vol. 136, p. 105954, 2020, doi: https://doi.org/10.1016/j.compositesa.2020.105954.

[86] S. H. Yetgin, "Effect of multi walled carbon nanotube on mechanical, thermal and rheological properties of polypropylene," *J. Mater. Res. Technol.*, vol. 8, no. 5, pp. 4725–4735, 2019, doi: https://doi.org/10.1016/j.jmrt.2019.08.018.

[87] H. Elkady and A. Hassan, "Assessment of High Thermal Effects on Carbon Nanotube (Cnt)- Reinforced Concrete," *Sci. Rep.*, vol. 8, no. 1, pp. 1–11, 2018, doi: 10.1038/s41598-018-29663-5.

[88] Y. Chiker, M. Bachene, M. Guemana, B. Attaf, and S. Rechak, "Free vibration

analysis of multilayer functionally graded polymer nanocomposite plates reinforced with nonlinearly distributed carbon-based nanofillers using a layer-wise formulation model," *Aerosp. Sci. Technol.*, vol. 104, p. 105913, 2020, doi: 10.1016/j.ast.2020.105913.

[89] B. Saiah, Y. Chiker, M. Bachene, B. Attaf, and M. Guemana, "Vibrational Behavior of Temperature-Dependent Piece-Wise Functionally Graded Polymeric Nanocomposite Plates Reinforced with Monolayer Graphene," *J. Vib. Eng. Technol.*, no. 0123456789, 2023, doi: 10.1007/s42417-023-01062-9.

[90] M. E. Golmakani, E. Rahimi, and M. Sadeghian, "Large deflection of functionally graded carbon nanotube reinforced composite cylindrical shell exposed to internal pressure and thermal gradient," *Math. Methods Appl. Sci.*, no. November 2020, pp. 1–19, 2021, doi: 10.1002/mma.7569.

[91] Z. Wang and H. Shen, "Composites : Part B Nonlinear vibration and bending of sandwich plates with nanotube-reinforced composite face sheets," *Compos. Part B*, vol. 43, no. 2, pp. 411–421, 2012, doi: 10.1016/j.compositesb.2011.04.040.

[92] L. W. Zhang, Z. G. Song, and K. M. Liew, "State-space Levy method for vibration analysis of FG-CNT composite plates subjected to in-plane loads based on higher-order shear deformation theory," *Compos. Struct.*, 2015, doi: 10.1016/j.compstruct.2015.08.138.

[93] S. Amir, E. Arshid, S. M. A. Rasti-alhosseini, and A. Loghman, "Quasi-3D tangential shear deformation theory for size-dependent free vibration analysis of three-layered FG porous micro rectangular plate integrated by nano-composite faces in hygrothermal environment," *J. Therm. Stress.*, vol. 0, no. 0, pp. 1–24, 2019, doi: 10.1080/01495739.2019.1660601.

[94] E. Reissner, "On the Theory of Bending of Elastic Plates," *Stud. Appl. Math.*, vol. 23, no. 1–4, pp. 184–191, 1944, doi: 10.1002/sapm1944231184.

[95] E. Reissner, "The effect of transverse shear deformation on the bending of elastic plates," *J. Appl. Mech.*, vol. 12, no. 2, pp. A69–A77, 1945, [Online]. Available: https://doi.org/10.1115/1.4009435

[96] H. Hencky, "Über die Berücksichtigung der Schubverzerrung in ebenen Platten," *Ingenieur-Archiv*, vol. 16, no. 1, pp. 72–76, 1947, doi: 10.1007/BF00534518.

[97] R. D. Mindlin, "Influence of Rotatory Inertia and Shear on Flexural Motions of Isotropic, Elastic Plates," *J. Appl. Mech.*, vol. 18, no. 1, pp. 31–38, Apr. 2021, doi: 10.1115/1.4010217.

[98] A. K. Noor and W. Scott Burton, "Stress and free vibration analyses of multilayered composite plates," *Compos. Struct.*, vol. 11, no. 3, pp. 183–204, 1989, doi: 10.1016/0263-8223(89)90058-5.

[99] P. F. Pai, "A new look at shear correction factors and warping functions of anisotropic laminates," *Int. J. Solids Struct.*, vol. 32, no. 16, pp. 2295–2313, 1995, doi: 10.1016/0020-7683(94)00258-X.

[100] N. J. Reddy, *Laminated Composite Plates and Shells: theory and analysis*. 2003.

[101] K. S. SAI RAM and P. K. SINHA, "Hygrothermal effects on the free vibration of laminated composite plates," *J. Sound Vib. 158(l), 133-148*, vol. 158, pp. 133–148,

1992.

[102] D. R. Vepa, *DYNAMICS OF SMART STRUCTURES*. 2010.

[103] E. Hinton and N. Bićanić, “A comparison of lagrangian and serendipity mindlin plate elements for free vibration analysis,” *Comput. Struct.*, vol. 10, no. 3, pp. 483–493, 1979, doi: 10.1016/0045-7949(79)90023-3.

[104] T. J. R. Hughes, M. Cohen, and M. Haroun, “Reduced and selective integration techniques in the finite element analysis of plates,” *Nucl. Eng. Des.*, vol. 46, no. 1, pp. 203–222, 1978, doi: 10.1016/0029-5493(78)90184-X.

[105] P. K. Parhi, S. K. Bhattacharyya, and P. K. Sinha, “Hygrothermal effects on the dynamic behavior of multiple delaminated composite plates and shells,” *J. Sound Vib.*, vol. 248, no. 2, pp. 195–214, 2001, doi: 10.1006/jsvi.2000.3506.

[106] A. K. Singh and A. Bhar, “Isogeometric FE analysis of CNT-reinforced composite plates: free vibration,” *SN Appl. Sci.*, vol. 1, no. 9, pp. 1–7, 2019, doi: 10.1007/s42452-019-1027-x.

[107] L. Kumar, S. Neeraj, and G. Gagandeep, “Buckling and Free Vibration Analysis of Temperature - Dependent Functionally Graded CNT - Reinforced Plates,” *J. Vib. Eng. Technol.*, vol. 11, no. 1, pp. 175–192, 2022, doi: 10.1007/s42417-022-00571-3.

[108] N. Dinh, T. Quoc, V. Mahesh, and N. Dinh, “Analytical solutions for nonlinear magneto-electro-elastic vibration of smart sandwich plate with carbon nanotube reinforced nanocomposite core in hygrothermal environment,” *Int. J. Mech. Sci.*, vol. 186, no. March, p. 105906, 2020, doi: 10.1016/j.ijmecsci.2020.105906.

[109] H. Hosseini and R. Kolahchi, “Seismic response of functionally graded-carbon nanotubes-reinforced submerged viscoelastic cylindrical shell in hygrothermal environment,” *Phys. E Low-dimensional Syst. Nanostructures*, 2018, doi: 10.1016/j.physe.2018.04.037.

[110] B. Huang *et al.*, “Bending and free vibration analyses of antisymmetrically laminated carbon nanotube-reinforced functionally graded plates,” *J. Compos. Mater.*, 2016, doi: 10.1177/0021998316685165.